Metal Hexacyanoferrate/Prussian Blue Analogue as a New Class of Promoters of Surface Redox Reactions for Efficient Photocatalytic Water Splitting

Hikaru Matsuoka

2022

Table of Contents

General Introduction

1. Background of the work

1.1. Water splitting using semiconductor photocatalyst for hydrogen production

The increase in energy demands and environmental concerns has encouraged the replacement of the fossil fuels with sustainable and clean energy sources within the next few decades. Hydrogen (H_2) has garnered significant attention as not only a clean energy carrier to generate electricity and/or heat via technologies such as fuel cells, but also a raw material to produce ammonia and useful hydrocarbon chemicals. However, the present industrial H_2 production relies heavily on the steam reforming of fossil fuels (e.g., methane (CH_4) gas), which simultaneously generates significant amounts of CO_2, as described by Eqs.1 and 2.

$$CH_4 + H_2O \rightarrow 3H_2 + CO \quad \text{(Eq. 1)}$$

$$CO + H_2O \rightarrow H_2 + CO_2 \quad \text{(Eq. 2)}$$

To develop a truly sustainable society, H_2 must be produced from water using renewable energy sources such as solar power, stored in an appropriate manner, and then converted back to water after obtaining energy through combustion or electric generation (Eq. 3).

$$2H_2O \rightleftarrows 2H_2 + O_2 \quad \text{(Eq. 3)}$$

In addition, the cost of H_2 production must be significantly reduced. The retail price of H_2 is currently approximately 100 yen per normal cubic meter (Nm^3: volume unit at 0 °C, 1.013×10^5 Pa). Japanese government, in the Basic Hydrogen Strategy, set the target price of H_2 to approximately 30 yen per Nm^3. The United States Department of Energy (DOE) has set similar targets. Water splitting using the combination of a photovoltaic (PV) cell and electrolysis is one of the possible methods for clean production of H_2 from water by utilizing solar light energy. Currently, this technology can realize a solar-to-hydrogen (STH) energy conversion efficiency exceeding 10% by employing commercially available PV cells with efficiency exceeding 16%, even after considering the loss during electrolysis of water (70%–80%).[1–3] However, it is currently difficult to achieve the abovementioned target price (30 yen/Nm^3) owing to the high cost of water electrolysis systems even after the price of PV becomes drastically low.[4]

Photocatalytic water splitting using semiconductor particles has garnered considerable attention as a promising technology that can achieve the target H_2 price of around 30 yen/Nm^3.[4–12] For example, the DOE has estimated that the price of H_2 can be

approximately 16 yen/Nm^3 if a single photocatalyst (i.e., one-step photoexcitation system) can split water with a STH conversion efficiency of 10%, and 23 yen/Nm^3 can be obtained with a conversion efficiency of 5%.[4] As for the Z-scheme water splitting system (i.e., two-step photoexcitation system) comprising two different photocatalysts, 32 yen/Nm^3 can be achieved with a conversion efficiency of 5%.[4]

Figure 1a shows a schematic diagram of a one-step photoexcitation system. To split water into H_2 and O_2 using a single semiconductor photocatalyst, it must possess a conduction band minimum (CBM) that is more negative than the water reduction potential (H^+/H_2, 0 V vs. standard hydrogen electrode (SHE)), and the valence band maximum (VBM) must be more positive than the water oxidation potential (O_2/H_2O, 1.23 V vs. SHE). In addition, the photocatalyst material must be stable during the photocatalysis. The following three main processes should proceed efficiently on/in the semiconductors (Figure 1b): (i) The absorption of photons with energy values greater than the semiconductor bandgap to excite electrons from the VB to the CB, creating electron (e^-)/hole (h^+) pairs; (ii) the separation of the photoexcited carriers into free carriers and subsequent migration to accumulate at the active sites on the particle surfaces without recombination; (iii) reduction of protons (or water) to H_2 and oxidation of water to O_2 by the electrons and holes, respectively. Improving the efficiency of processes (i)–(iii) is crucial for realizing practical high STH conversion efficiency. For example, the loading of appropriate cocatalyst such as metal nanoparticles (e.g., Pt and Ru) or metal oxide nanoparticles (e.g., RuO_2, IrO_2 and CoO_x) has been performed to effectively improve surface redox reactions (process (iii)), as well as to obtain carriers from the semiconductor

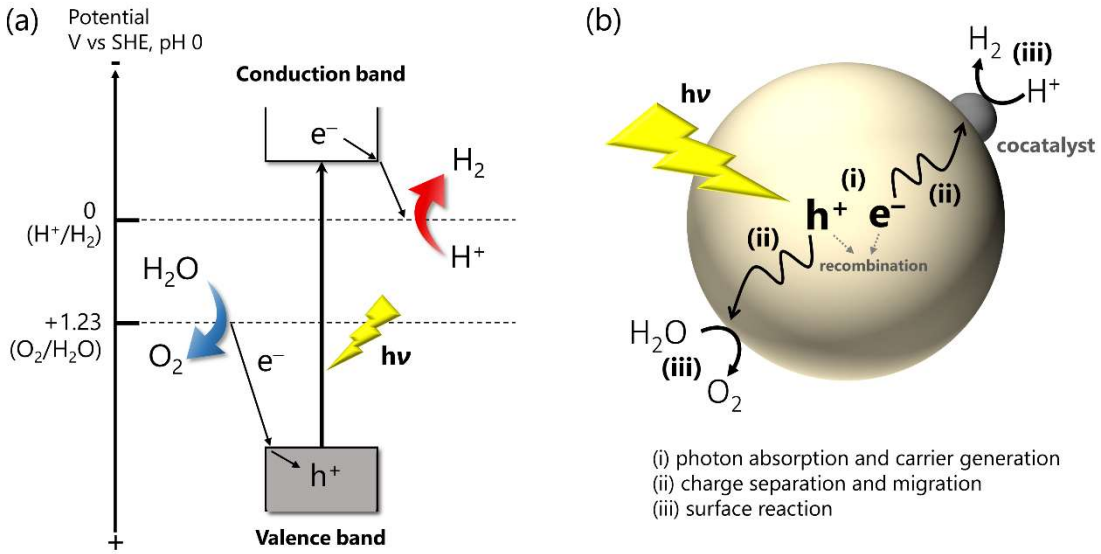

Figure 1. (a) Schematic illustration of water splitting using a single photocatalyst. (b) reaction steps in photocatalytic water splitting on a semiconductor particle.

bulk (process (ii)). It has been recently demonstrated that approximately 100% of quantum efficiencies (at wavelengths between 350 and 360 nm) of water slitting can be achieved by using an Al-doped $SrTiO_3$ with suitable cocatalysts, in which the above processes (ii) and (iii) were ultimately optimized.[13] Unfortunately, however, this Al-doped $SrTiO_3$ can only harvest ultraviolet (UV) lights with wavelength shorter than 390 nm due to its wide bandgap of $SrTiO_3$ (about 3.2 eV).

1.2. Utilization of visible light

Figure 2a shows a typical solar spectrum. Because UV light occupies a small percentage of the solar spectrum, the solar conversion efficiency would only be 2% even if all UV lights up to 400 nm can be utilized. As described in Section 1.1, achieving an STH conversion efficiency of 5% or higher is indispensable for the cost-effective H_2 production via photocatalytic water splitting.[4,10] Figure 2b shows the calculated STH conversion efficiencies as a function of wavelength for an overall water splitting process using photocatalysts with various quantum efficiencies. For example, an STH conversion efficiency of 5% can be obtained by using a photocatalyst absorbing light up to 500 nm and splitting water with quantum yield of 60%. Thus, it is essential to use visible light, which constitutes approximately one-half of sunlight. In other words, it is indispensable to develop the photocatalyst materials with a band gap narrower than 3.1 eV, while keeping the band levels suitable for both water reduction and oxidation.

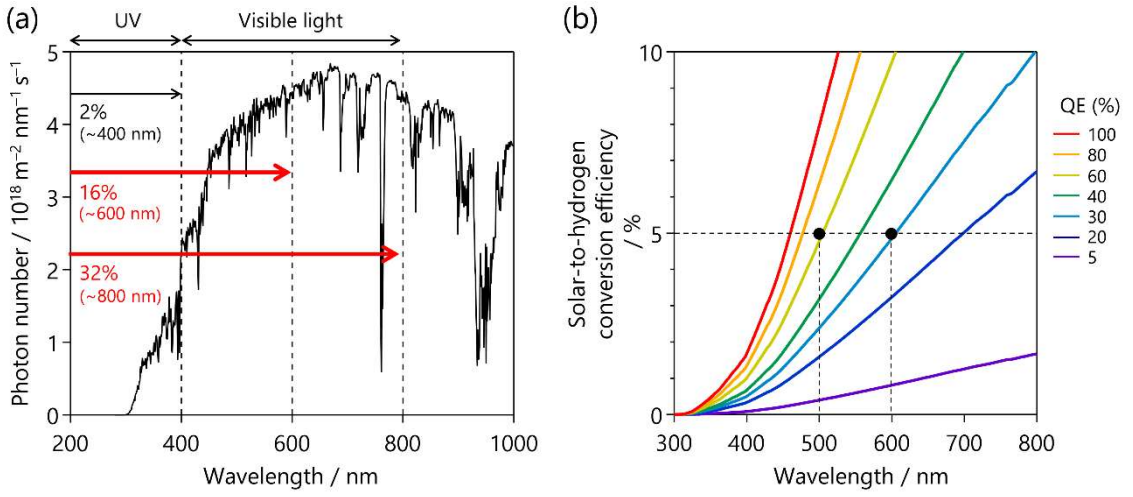

Figure 2. (a) Solar spectrum and solar energy conversion efficiency for overall water splitting using photocatalysts with 100% of quantum efficiency (QE) and (b) relationship between QE and solar-to-hydrogen conversion efficiency.

Figure 3 shows the band diagrams of representative photocatalysts. Since the discovery of the Honda–Fujishima effect in 1972,[14] many metal oxides have been reported as active photocatalysts that can split water into H_2 and O_2.[15–17] However, most of them have wide band gaps (E_g) that can absorb only UV light. The difficulty in utilizing visible light for water splitting using oxide semiconductors is primarily due to the fixed VBM levels around +3.0 V vs. SHE.[16] This fixation is basically originated from the dominant contribution of O-2p orbitals to the density of states (DOS) around the VBM. Eventually, metal oxides with visible light absorption ($E_g < 3.0$ eV) cannot possess a CBM that is more negative than the reduction potential of water (0 V vs. SHE).

This fact promoted the research on non-oxide semiconductors such as metal sulfides (e.g., CdS) in the early 1980s for water splitting under visible light.[18] Because the p-orbitals of non-oxide anions (such as S-3p of S^{2-}) have a higher (i.e., more negative) potential than the O-2p orbitals, the VBM of non-oxides is located at a much more negative potential than that of oxides. Thus, the upward shift of VBM endow them with both visible light absorption ability (i.e., narrow bandgap) and a more negative CBM compared with the water reduction potential in many cases. However, such non-oxides have been reported to undergo self-oxidation, in which the photogenerated holes preferentially oxidize the non-oxide anions (e.g., $CdS + 2h^+ \rightarrow Cd^{2+} + S$)[18] instead of water, eventually resulting in photocorrosion or surface inactivation. Such self-oxidative deactivation has rendered it extremely difficult to achieve simultaneous generation of H_2 and O_2 using such non-oxide semiconductors.

Subsequently, in the early 2000s, mixed-anion semiconductors such as oxysulfides and oxynitrides have garnered the attention of researchers owing to their better durability against self-oxidative deactivation compared with those of the aforementioned non-oxides.[19–21] In such mixed anion semiconductors, the p-orbitals of non-oxide anions (e.g., N-2p of N^{3-}), which have a lower electronegativity than O^{2-}, contribute to the DOS near the VBM together with O-2p, thereby elevating their VBM to a higher potential than those of the corresponding oxides. The mixed VBs formed by the hybridization of non-oxide p-orbitals and O-2p are more durable against self-oxidation compared with simple non-oxides (e.g., sulfides or nitrides). Then some mixed-anion semiconductors such as TaON have been demonstrated to produce oxygen from water under visible-light irradiation.[19–21] Although the intrinsic problem (i.e., the competitive occurrence of self-oxidative deactivation) has not been completely solved, some surface modifications such as cocatalyst (e.g., IrO_x and CoO_x) loading have proven to be highly effective in selective water oxidation, thereby suppressing the self-oxidative deactivation.[22–25]

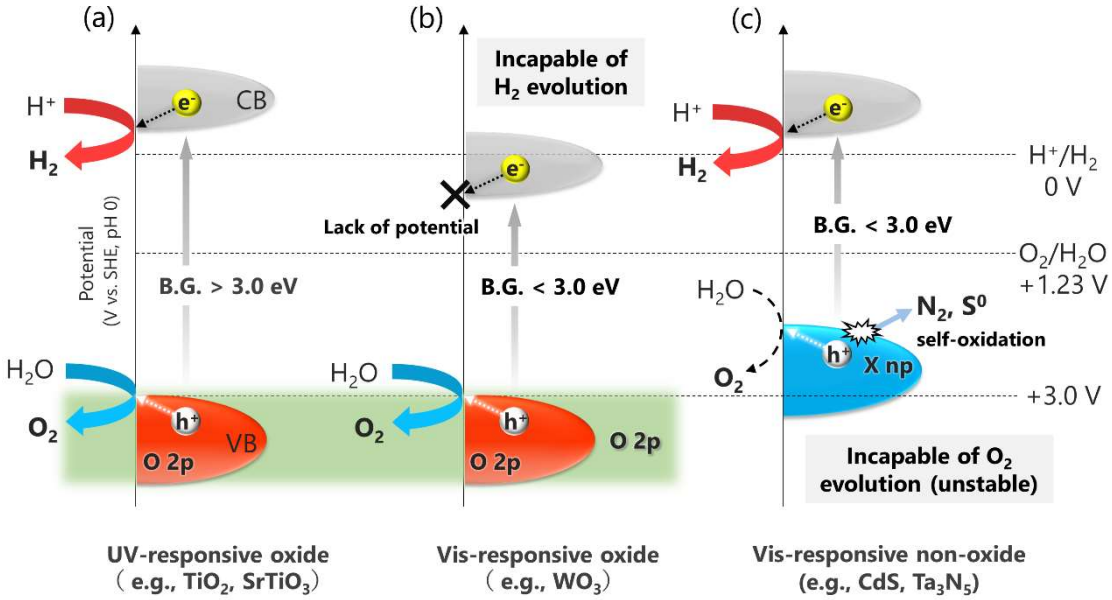

Figure 3. Schematic band energy diagram of various semiconductors.

1.3. Strategies for achieving visible-light-driven water splitting

Visible-light-driven water splitting can be achieved via one of two primary approaches (Figure 4). One is to use a single visible-light-responsive photocatalyst (one-step system, see Figure 4a), as described above. To split water under visible light, a single photocatalyst must (a) possess a band gap narrower than 3.1 eV, (b) be stable under photoirradiation, and (c) possess conduction and valence band levels suitable for both water reduction and oxidation. Although various band engineering methods have been investigated, only a few photocatalysts such as GaN:ZnO,[26] TaON,[27] Ir-doped $SrTiO_3$,[28] and $Y_2Ti_2S_2O_5$[29] can be used to split water into H_2 and O_2 in a stoichiometric ratio under visible light owing to their strict requirements.

The other approach is to introduce a two-step photoexcitation process for water splitting (see Figure 4b),[11,30–33] which is inspired by the natural photosynthesis of green plants and is known as the Z-scheme water splitting system. In this system, the water-splitting reaction is segmented into two stages: H_2 production and O_2 production. The two photocatalysts are electrically combined with electron mediators such as redox couples (e.g., trivalent/divalent iron (Fe^{3+}/Fe^{2+}) and iodate/iodide (IO_3^-/I^-)). On an O_2 evolution photocatalyst, water is oxidized to O_2, accompanied by the reduction of the oxidant (e.g., IO_3^-) to a reductant (e.g., I^-). Meanwhile, the re-oxidation of the reductant to the oxidant occurs on an H_2 evolution photocatalyst, accompanied by the reduction of water to H_2. This system can reduce the energy required for each photocatalysis, thereby enabling it the utilization of visible light more efficiently as compared with conventional water-

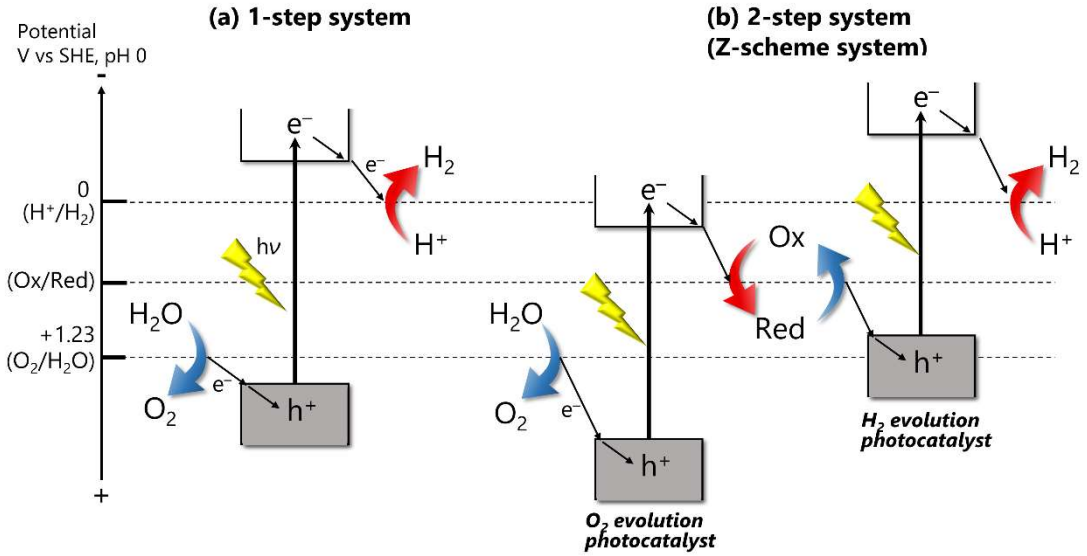

Figure 4. Two types of overall water splitting systems: (a) one step photoexcitation system using a single photocatalyst, (b) two step photoexcitation system using two kinds of photocatalysts.

splitting systems. In other words, photocatalysts that possess the potential for either water oxidation or reduction can be employed on one side of the Z-scheme system, which is typified by tungsten trioxide (WO_3) and bismuth vanadate ($BiVO_4$). Although they cannot reduce water to H_2 because their CBM are more positive than the reduction potential of water, their CBM and VBM levels are sufficient for reducing oxidants such as Fe^{3+} to Fe^{2+} (Fe^{3+}/Fe^{2+}, 0.77 V vs. SHE) and oxidize water to O_2, respectively; therefore, they can serve as O_2 evolution photocatalysts in Z-scheme water splitting systems.[30,31]

Most Z-scheme water splitting systems rely on redox couples such as Fe^{3+}/Fe^{2+} or IO_3^-/I^- to realize an efficient electron transfer between H_2- and O_2-evolution photocatalysts. Some new redox couples (e.g., VO_2^+/VO^{2+},[34] metal complexes,[35,36] and polyoxometalates[37]) and solid electron mediators (e.g., carbon-based materials,[38,39] indium tin oxide particles,[40] and Au[41]) have recently been demonstrated. In general, solid electron mediators are more favorable in terms of practical and industrial use than ionic redox couples (e.g., Fe^{3+}/Fe^{2+}, IO_3^-/I^-) because of the facile recovery of the photocatalyst and reclamation of clean water.[38] However, in both cases, the efficiency remains low; therefore, researchers have investigated significant efforts in improving it using various strategies such as surface modification.

1.4. Keys and strategies for improving (Z-scheme) water splitting

To achieve water splitting with a high STH conversion efficiency, surface modifications (e.g., cocatalyst loading, protective layer covering, and hetero-junction introduction) as

well as the development of novel photocatalysts are indispensable. The cocatalyst generally (1) enhances the charge separation in the photocatalyst, and/or (2) facilitates the surface chemical reactions by the carriers, i.e., water reduction and/or oxidation for one-step water splitting.[9]

1.4.1. Promotion and suppression of surface redox reactions by surface modification

1.4.1.1. Cocatalysts for hydrogen evolution reaction or oxygen evolution reaction

Hydrogen evolution reaction (HER)

Because the majority of semiconductor materials do not inherently possess the active sites for photocatalytic H_2 evolution, cocatalysts for HER must be loaded. Although nanoparticles of noble metals such as Pt, Rh, and Pd have been widely used as an effective cocatalyst for HER,[15,18,42–44] they simultaneously showed catalytic activities for backward reactions, i.e., O_2 reduction and water formation from H_2 and O_2,[15,45,46] lowering the overall efficiency in water splitting. Therefore, various strategies to selectively proceed with HER have been developed, typified by the coating of (hydro)oxide layers (e.g., CrO_x,[45] TiO_x,[47,48] TaO_x,[47] and ZrO_x[49]) on noble metal cocatalysts, and the loading of complex oxides (e.g., $Rh_{2-x}Cr_xO_3$[50] and $RhZrO_x$[51]) instead of noble metals. The (hydro)oxide layers shielding HER cocatalysts or the photocatalyst surfaces are permeable to protons but can effectively suppress the penetration of evolved H_2 and O_2.[52] By contrast, the reactions on such complex oxides have not been fully understood.

Oxygen evolution reaction (OER)

As described above, the oxide semiconductors possess deep VBMs at approximately +3.0 V vs. SHE in most cases. In short, they generally possess sufficient oxidizing power (i.e., sufficient driving force) for O_2 evolution from water. Indeed, many of them have been demonstrated to split water even without loading of OER cocatalyst. By contrast, non-oxide semiconductors such as (oxy)nitrides have shallower VBM than oxides; therefore, the loading of OER cocatalysts on them should significantly affects the O_2 evolution activity. In addition, the loading of appropriate OER cocatalysts also have been proven to prevent non-oxide semiconductors (e.g., TaON) from self-oxidative deactivation through the facile capture of photogenerated holes prior to self-oxidation. The oxide species of novel metals such as RuO_x and IrO_x have often been used as OER cocatalysts.[22,25,53] Recently, some non-noble-metal-based (e.g., Co-, Fe-, and Ni-based ones[23,54–56]) OER cocatalysts have garnered significant attention, although some of them possess their stability issue to be addressed (e.g., dissolution under acidic conditions).

1.4.1.2. Cocatalyst for reactions of redox mediators in Z-scheme water splitting

In Z-scheme water splitting systems (Figure 5), facilitating the oxidation/reduction of redox mediators (e.g., Fe^{3+}/Fe^{2+}, IO_3^-/I^-, and $[Fe(CN)_6]^{3-}/[Fe(CN)_6]^{4-}$) as well as HER/OER is critical for realizing highly efficient water splitting. Furthermore, unfavorable backward reactions, i.e., the re-oxidation and re-reduction of redox mediators, should be suppressed. Hence, the development of cocatalysts for the Z-scheme water splitting system is more elaborate than that for the one-step system. However, few studies have focused on cocatalysts for the oxidation/reduction of redox mediators compared with those for HER/OER. For the reduction of oxidants of redox mediators, Ir-, Pt-, Ru-, and Fe-based compounds have been demonstrated to serve as cocatalysts for IO_3^- reduction,[53,57–62] whereas Au metal as a cocatalyst for $[Fe(CN)_6]^{3-}$ reduction.[63] By contrast, only a few examples of oxidation cocatalysts have so far been reported: IrO_2 on $Sm_2Ti_2S_2O_5$ for I^- oxidation[44] and cadmium hexacyanoferrate on sulfide for $[Fe(CN)_6]^{4-}$ oxidation.[36] As will be described later, cadmium hexacyanoferrate (CdHCF) is one of the coordination polymers with controllability in terms of metal or ligand substitution.

In addition to promoting the forward reactions of redox mediators, suppressing the backward reactions is crucial. However, such suppression typically relies on the specific affinity between the photocatalyst surface and each redox species, such as the selective adsorption of either of the redox couples on the photocatalyst surface. For example, it has been demonstrated that IO_3^- preferentially adsorbs on the surfaces of rutile TiO_2 or WO_3 particles, whereas I^- cannot, thereby allowing these photocatalysts to oxidize water even in the presence of a considerably high concentration of I^-.[7] Although the intentional control of surface redox reactions via surface modifications has been investigated recently,[57,64,65] the rational promotion/suppression of the forward/backward reactions of redox mediators are still challenging topics.

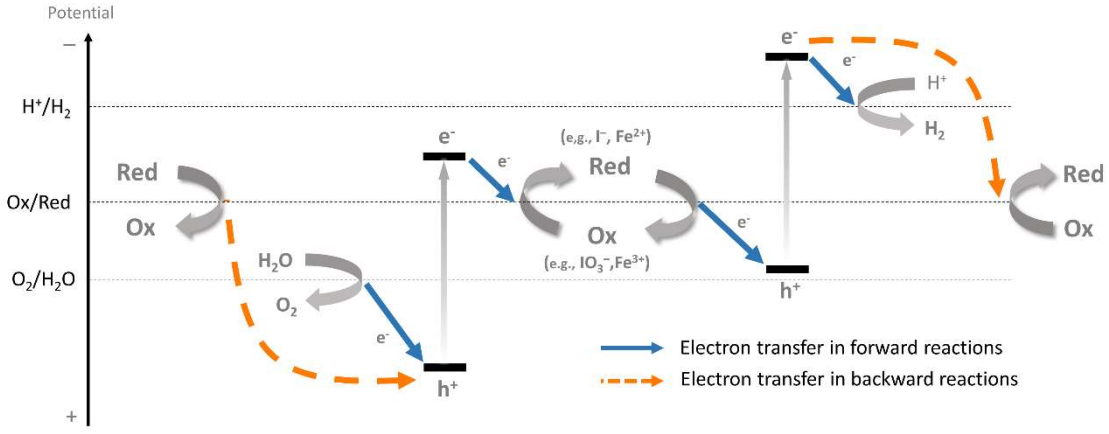

Figure 5. Forward and backward reactions in Z-scheme water splitting system.

1.5. Application of Metal hexacyanoferrate/Prussian blue analogue

1.5.1. Metal hexacyanoferrate/Prussian blue analogue

Prussian blue (PB = iron hexacyanoferrate), with its three-century history, is recognized as the first synthetic coordination compound[66] and is widely known as the blue pigment in paintings (e.g., ukiyoe) or photographs. In the past few decades, PB analogue (PBA), also known as metal hexacyanoferrate (MHCF), where nitrogen (N)-coordinated Fe in PB is substituted by other metal cations, has garnered considerable attention as a functional material, as well as PB. This is basically because of their favorable electrochemical and photomagnetic properties as well as their high designabilities,[67] as will be described later more comprehensively. Cadmium hexacyanoferrate (CdHCF), which was introduced in Section 1.4.1.2, belongs to the MHCF family.

MHCF has a general formula of $A_hM_k[Fe(CN)_6]_l{\cdot}mH_2O$ (*h, k, l, m*: composition ratios, A: alkali metal cation (typically, Na^+ or K^+), M: (transition) metal cation), where M and Fe ions are bridged by linear cyanide (CN) ligands.[67] Representative structures based on composition are shown in Figure 6 for A = K^+, M, and Fe in the II and II oxidation states, respectively. Most of the MHCFs have a face-centered cubic lattice (unit cell length: ~10.2 Å) with octahedral coordination of the M and Fe ions by –N≡C and –C≡N ligands, respectively.[67] The defect-free, i.e., "perfect", structure (Figure 6a) has the composition of $K_2M[Fe(CN)_6]$, where K^+ cations providing charge compensation are located in the tetrahedral sites in these structures. By contrast, the "defect" structure (Figure 6b) has the composition of $M_2[Fe(CN)_6]$. Because the number of M^{II} is greater than that of Fe^{II}, the octahedral cavities (i.e., $[Fe(CN)_6]$ vacancies) are occupied by coordinated water in the defect type to satisfy the charge neutrality requirement. The desired composition and/or structure of MHCFs vary by the intended application. For example, in the field of secondary ion batteries, "perfect" type is desirable in terms of specific capacity for inserting alkali cations. This is because the defect sites (i.e., $[Fe(CN)_6]$ vacancies) will reduce the amount of alkali cations in the lattice owing to charge balance and introduce more water molecules into the framework, thereby decreasing the initial charge capacity and causing more side reactions (i.e., water decomposition).[68] By contrast, in the field of (electro)catalysts, "defect" type is more favorable because many vacancies provide MHCFs with a high concentration of active metal sites (typically N-coordinated metal cation) accessible by target molecules such as water.[69,70]

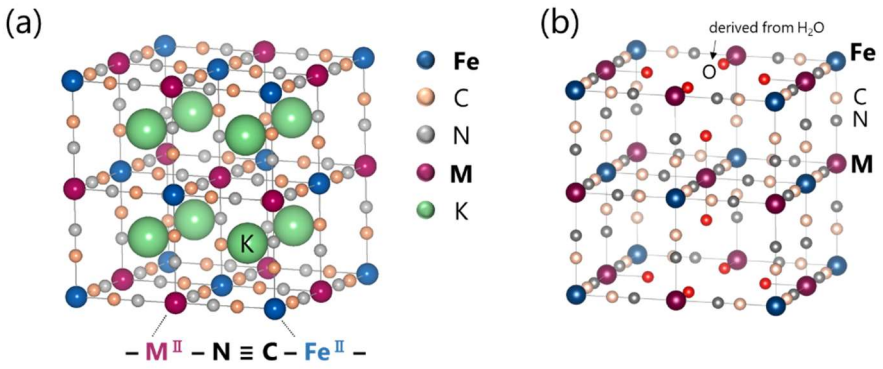

Figure 6. Typical structure of metal hexacyanoferrate (MHCF) containing M^{II} and Fe^{II}: (a) perfect type and (b) defect type.

In general, MHCF powders can be obtained easily as insoluble precipitates via a simple and inexpensive co-precipitation of M^n and $[Fe^{II(III)}(CN)_6]^{4-(3-)}$. Because this conventional co-precipitation reaction proceeds promptly, it is inherently difficult to control the composition, structure, and particle size. Therefore, the appropriate synthetic conditions such as the additives, reaction temperature, and precursor concentration, must be selected. For instance, the "perfect" type MHCFs have been prepared using a chelating reagent (e.g., citrate, EDTA),[71–73] in which the chelate lowers the rate of the reaction between M^{n+} and $[Fe(CN)_6]^{4-}$, and thereby provides sufficient time for nucleation and crystal growth, resulting in defect-free MHCFs.[71] Another approach for synthesizing the perfect type is by adding excess alkali metal salts (e.g., KCl) to the reaction mixture.[74] MHCF nanoparticles have been successfully synthesized by decreasing the reaction temperature (~2 °C)[75] or increasing the concentration of both metal cations and ferrocyanide anions.[76]

One of the most attractive features of MHCFs is their reversible electrochemical properties, which have been extensively investigated.[66,67,77] In general, the redox reaction of metal hexacyanoferrate can be expressed as shown in Eq. 4.

$$A_2M^{II}[Fe^{II}(CN)_6] \rightleftarrows A_{2-x}M^{II}[Fe^{III}_xFe^{II}_{1-x}(CN)_6] + xA^+ + xe^-, \quad \text{(Eq. 4)}$$

where x represents the number of moles of reacted electrons. Accompanied by the oxidation or reduction of Fe cations, the extraction or insertion of counter cations A^+, respectively, should proceed to compensate the charge balance in the structure. Notably, the geometry of MHCFs did not change significantly during ion insertion,[78] which affords long cycle lives in the electrodes or electrocatalysts. The redox potential of Fe is affected

by the N-coordinated metal cation.[79] For example, if N-coordinated metal cations have higher ionic potentials (the quotient of charge and radius), a higher (more negative) redox potential of Fe will be yielded because it reduces the σ-electron donation of the CN ligand, thereby resulting in electron-deficient Fe sites. When MHCFs contain electrochemically active metal cations coordinated to N, two-electron redox reactions (e.g., Fe^{III}/Fe^{II} and M^{III}/M^{II}) can be involved, allowing an increase in the specific capacity of secondary ion battery.[68]

Because the properties of MHCFs can be adjusted based on their components, they are adaptable for various applications. The wide variety of different combinations of types and quantities of substitutional elements in MHCFs allows the effective tuning of their lattice constant as well as electronic and ionic properties for target applications. For example, the control of the lattice constant by metal cation substitution significantly tune channel size in MHCF, thereby affecting the ionic conductivity, specific capacity and adsorption properties for the guest molecules or ions.[68] Hence, the (partial) substitution of components such as N-coordinated metal cations, alkali cations, and ligands in MHCF affords performance improvement. By exploiting these properties, the MHCF family has recently been applied in various research fields, such as electrochromic devices,[80,81] adsorbents for pollutants (e.g., radioactive Cs^+ and NH_3),[82–84] H_2O_2 sensors,[85] hydrogen storage,[86,87] electrodes for secondary batteries,[68,71,88,89] and (electro)catalysts.[69,90–94]

1.5.2. Metal hexacyanoferrate for oxidation (co)catalyst in photocatalytic water splitting

Based on the features of MHCFs described above, the MHCF family is expected to be a promising material as a promoter (cocatalyst) for surface redox reactions in photocatalytic water splitting systems. It has been revealed that CdHCFs modified on metal sulfides (e.g., CdS, $ZnIn_2S_4$) functioned as promoters (cocatalysts) for the oxidation of $[Fe(CN)_6]^{4-}$ via the redox cycles of Fe^{III}/Fe^{II} in CdHCFs, as illustrated in Figure 7.[36] Because the cocatalysts for the oxidation of redox mediators have not been pursued sufficiently, as mentioned above, modifications with CdHCFs will provide new insights into the development of oxidation cocatalysts in Z-scheme water splitting. However, systematic investigations into MHCFs as promoters of the oxidation of redox mediators, such as the performance improvement by varying metal cations and/or ligands, and the applicability to the oxidation of electron donors other than $[Fe(CN)_6]^{4-}$ have not been reported. Hence, the development of MHCFs which can enhance the activities of photocatalysts and the establishment in the design principles of them are highly desirable.

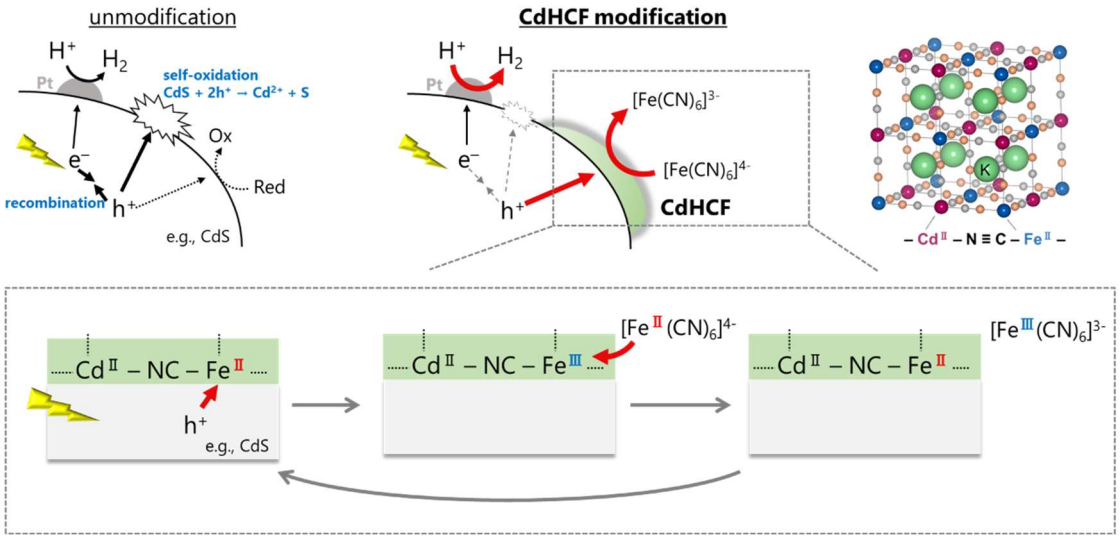

Figure 7. Proposed reaction mechanism of promoted H_2 evolution over some metal sulfide photocatalysts by CdHCF modification.

1.5.3. The possibility of metal hexacyanoferrate for "solid" redox mediator

As described above, MHCFs have been introduced for electrochemical applications owing to their reversible redox properties, and their finely and widely tunable redox potential by appropriately designing the constituent elements in MHCFs.[79] In addition, the redox potentials of Fe^{III}/Fe^{II} in various MHCFs[79] are suitable for Z-scheme water splitting, i.e., located between the water reduction and oxidation potentials. These facts also motivate the author to apply MHCFs into the solid electron mediator in Z-scheme water splitting systems.

2. Outline of the work

Based on the background, this thesis focuses on the application of metal hexacyanoferrates (MHCFs) to promoters of surface redox reactions to improve the efficiency of photocatalytic water splitting under visible light. The present thesis consists of general introduction and following five chapters.

In Chapter 1, the author demonstrated that various MHCFs, as well as previously-reported CdHCF, functioned as promoters of the $[Fe(CN)_6]^{4-}$ oxidation, thereby providing higher H_2 evolution rates on a metal sulfide ($ZnIn_2S_4$) photocatalyst under visible light. Electrochemical measurements revealed that the key to the enhancement in H_2 evolution by promoting $[Fe(CN)_6]^{4-}$ oxidation via MHCFs was their stable redox cycles with the redox potential located between the valence band maxima of photocatalysts and the redox

potential of $[Fe(CN)_6]^{3-}/[Fe(CN)_6]^{4-}$.

In Chapter 2, the author developed a stepwise method for MHCF modification. The stepwise method allowed for the formation of thinner layers of zinc or cadmium hexacyanoferrate (ZnHCF or CdHCF) on $ZnIn_2S_4$, providing higher H_2 evolution rates than those obtained by conventional loading of ZnHCF or CdHCF particles.

In Chapter 3, the author revealed that cobalt hexacyanoferrate (CoHCF) promoted the photocatalytic O_2 evolution on TaON particles in a basic (pH 8) or an acidic (pH 3) aqueous solution containing Ag^+ as an irreversible electron acceptor. It was further demonstrated that CoHCF could promote the O_2 evolution even in the presence of the Fe^{3+} reversible electron acceptor that is stable only under the acidic condition (at pH below 2.5) where conventional cobalt oxyhydroxides lost its activity due to dissolution.

In Chapter 4, the author revealed that photocatalytic H_2 evolution over TaON using Fe^{2+} electron donor was drastically enhanced by co-loading of indium hexacyanoferrate (InHCF) and Rh-Cr mixed oxide (RCO). A series of measurements clarified that InHCF promoted Fe^{2+} oxidation to Fe^{3+} by the photogenerated holes, while RCO did proton reduction to H_2 via the photoexcited electrons without being distracted by unfavorable reduction of Fe^{3+} to Fe^{2+}. The InHCF modification has first enabled Z-scheme water splitting using TaON as an H_2 evolution photocatalyst with Fe^{3+}/Fe^{2+} redox mediator.

In Chapter 5, the author demonstrated for the first time that InHCF functioned as a solid electron mediator in Z-scheme water splitting. Through some experiments, it was revealed that the redox cycles of Fe^{III}/Fe^{II} in InHCF mediates the forward electron transfer between an H_2- and an O_2-evolution photocatalyst, realizing the Z-scheme water splitting.

Finally, the results described in Chapters 1–5 were summarized and outlook was described.

References

1. Khaselev, O.; Turner, J. A. A. **1998**, *280*, 425–427.
2. Reece, S. Y.; Hamel, J. A.; Sung, K.; Jarvi, T. D.; Esswein, A. J.; Pijpers, J. J. H.; Nocera, D. G. *Science* **2011**, *334*, 645–648.
3. Rocheleau, R. E.; Miller, E. L.; Misra, A. *Energy and Fuels* **1998**, *12*, 3–10.
4. Pinaud, B. A.; Benck, J. D.; Seitz, L. C.; Forman, A. J.; Chen, Z.; Deutsch, T. G.; James, B. D.; Baum, K. N.; Baum, G. N.; Ardo, S.; Wang, H.; Millere, E.; Jaramillo, T. F. *Energy Environ. Sci.* **2013**, *6*, 1983–2002.
5. Osterloh, F. E. *Chem. Mater.* **2008**, *20*, 35.
6. Kudo, A.; Miseki, Y. *Chem. Soc. Rev.* **2009**, *38*, 253–278.
7. Abe, R. *Bull. Chem. Soc. Jpn* **2011**, *84*, 1000–1030.
8. Fabian, D. M.; Hu, S.; Singh, N.; Houle, F. A.; Hisatomi, T.; Domen, K.; Osterloh, F. E.; Ardo, S. *Energy Environ. Sci.* **2015**, *8*, 2825–2850.
9. Maeda, K.; Domen, K. *Bull. Chem. Soc. Jpn.* **2016**, *89*, 627–648.
10. Shaner, M. R.; Atwater, H. A.; Lewis, N. S.; McFarland, E. W. *Energy Environ. Sci.* **2016**, *9*, 2354–2371.
11. Wang, Y.; Suzuki, H.; Xie, J.; Tomita, O.; Martin, D. J.; Higashi, M.; Kong, D.; Abe, R.; Tang, J. *Chem. Rev.* **2018**, *118*, 5201–5241.
12. Wang, Q.; Domen, K. *Chem. Rev.* **2020**, *120*, 919–985.
13. Takata, T.; Jiang, J.; Sakata, Y.; Nakabayashi, M.; Shibata, N.; Nandal, V.; Seki, K.; Hisatomi, T.; Domen, K. *Nature* **2020**, *581*, 411–414.
14. Fujishima, A.; Honda, K. *Nature* **1972**, *238*, 37–38.
15. Sato, S.; White, J. M. P *Chem. Phys. Lett.* **1980**, *72*, 83–86.
16. Domen, K.; Naito, S.; Onishi, T.; Tamaru, K.; Soma, M. *J. Phys. Chem.* **1982**, *86*, 3657–3661.
17. Domen, K.; Kudo, A.; Shinozaki, A.; Tanaka, A.; Maruya, K.; Onishi, T. *J. Chem. Soc. Chem. Commun.* **1986**, 356–357.
18. Buehler, N.; Meier, K.; Reber, J. F. *J. Phys. Chem.* **1984**, *88*, 3261–3268.
19. Ishikawa, A.; Takata, T.; Kondo, J. N.; Hara, M.; Kobayashi, H.; Domen, K. *J. Am. Chem. Soc.* **2002**, *124*, 13547–13553.
20. Hitoki, G.; Takata, T.; Kondo, J. N.; Hara, M.; Kobayashi, H.; Domen, K. *Chem. Commun.* **2002**, *2*, 1698–1699.
21. Kasahara, A.; Nukumizu, K.; Hitoki, G.; Takata, T.; Kondo, J. N.; Hara, M.; *J. Phys. Chem. A* **2002**, *106*, 6750–6753.
22. Higashi, M.; Domen, K.; Abe, R. *Energy Environ. Sci.* **2011**, *4*, 4138–4147.
23. Higashi, M.; Domen, K.; Abe, R. *J. Am. Chem. Soc.* **2012**, *134*, 6968–6971.

24. Zhang, F.; Yamakata, A.; Maeda, K.; Moriya, Y.; Takata, T.; Kubota, J.; Teshima, K.; Oishi, S.; Domen, K. *J. Am. Chem. Soc.* **2012**, *134*, 8348–8351.
25. Maeda, K.; Domen, K. *Angew. Chemie - Int. Ed.* **2012**, *51*, 9865–9869.
26. Maeda, K.; Takata, T.; Hara, M.; Saito, N.; Inoue, Y.; Kobayashi, H.; Domen, K. *J. Am. Chem. Soc.* **2005**, *127*, 8286–8287.
27. Maeda, K.; Lu, D.; Domen, K. *Chem. - A Eur. J.* **2013**, *19*, 4986–4991.
28. Asai, R.; Nemoto, H.; Jia, Q.; Saito, K.; Iwase, A.; Kudo, A. *Chem. Commun.* **2014**, *50*, 2543–2546.
29. Wang, Q.; Nakabayashi, M.; Hisatomi, T.; Sun, S.; Akiyama, S.; Wang, Z.; Pan, Z.; Xiao, X.; Watanabe, T.; Yamada, T.;Shibata, N.; Takata, T.;Domen, K. *Nat. Mater.* **2019**, *18*, 827–832.
30. Sayama, K.; Mukasa, K.; Abe, R.; Abe, Y.; Arakawa, H. *Chem. Commun.* **2001**, *23*, 2416–2417.
31. Kato, H.; Hori, M.; Konta, R.; Shimodaira, Y.; Kudo, A. *Chem. Lett.* **2004**, *33*, 1348–1349.
32. Kudo, A. *MRS Bull.* **2011**, *36*, 32–38.
33. Maeda, K. *ACS Catal.* **2013**, *3*, 1486–1503.
34. Miseki, Y.; Fujiyoshi, S.; Gunji, T.; Sayama, K. *J. Phys. Chem. C* **2017**, *121*, 9691–9697.
35. Sasaki, Y.; Kato, H.; Kudo, A. *J. Am. Chem. Soc.* **2013**, *135*, 5441–5449.
36. Shirakawa, T.; Higashi, M.; Tomita, O.; Abe, R. *Sustain. Energy Fuels* **2017**, *1*, 1065–1073.
37. Tsuji, K.; Tomita, O.; Higashi, M.; Abe, R. *ChemSusChem* **2016**, *9*, 2201–2208.
38. Iwase, A.; Ng, Y. H.; Ishiguro, Y.; Kudo, A.; Amal, R. *J. Am. Chem. Soc.* **2011**, *133*, 11054–11057.
39. Wang, Q.; Hisatomi, T.; Suzuki, Y.; Pan, Z.; Seo, J.; Katayama, M.; Minegishi, T.; Nishiyama, H.; Takata, T.; Seki, K.; Kudo, A.; Yamada, T.; Domen, K. *J. Am. Chem. Soc.* **2017**, *139*, 1675–1683.
40. Wang, Q.; Okunaka, S.; Tokudome, H.; Hisatomi, T.; Nakabayashi, M.; Shibata, N.; Yamada, T.; Domen, K. *Joule* **2018**, *2*, 2667–2680.
41. Wang, Q.; Hisatomi, T.; Jia, Q.; Tokudome, H.; Zhong, M.; Wang, C.; Pan, Z.; Takata, T.; Nakabayashi, M.; Shibata, N.; Li, Y.; Sharp, I. D.; Kudo, A.; Yamada, T.; Domen, K. *Nat. Mater.* **2016**, *15*, 611–613.
42. Maeda, K.; Terashima, H.; Kase, K.; Higashi, M.; Tabata, M.; Domen, K. *Bull. Chem. Soc. Jpn.* **2008**, *81*, 927–937.
43. Wang, Z.; Luo, Y.; Hisatomi, T.; Vequizo, J. J. M.; Suzuki, S.; Chen, S.; Nakabayashi, M.; Lin, L.; Pan, Z.; Kariya, N.; Yamakata, A.; Shibata, N.; Takata, T.; Teshima, K.; Domen, K. *Nat. Commun.* **2021**, *12*, 1005.
44. Ma, G.; Chen, S.; Kuang, Y.; Akiyama, S.; Hisatomi, T.; Nakabayashi, M.; Shibata, N.;

Katayama, M.; Minegishi, T.; Domen, K. *J. Phys. Chem. Lett.* **2016**, *7*, 3892–3896.

45. Maeda, K.; Teramura, K.; Lu, D.; Saito, N.; Inoue, Y.; Domen, K. *Angew. Chemie - Int. Ed.* **2006**, *45*, 7806–7809.
46. Kanazawa, T.; Maeda, K. *ACS Appl. Mater. Interfaces* **2016**, *8*, 7165–7172.
47. Takata, T.; Pan, C.; Nakabayashi, M.; Shibata, N.; Domen, K. *J. Am. Chem. Soc.* **2015**, *137*, 9627–9634.
48. Pan, C.; Takata, T.; Nakabayashi, M.; Matsumoto, T.; Shibata, N.; Ikuhara, Y.; Domen, K. *Angew. Chemie - Int. Ed.* **2015**, *54*, 2955–2959.
49. Okunaka, S.; Kameshige, H.; Ikeda, T.; Tokudome, H.; Hisatomi, T.; Yamada, T.; Domen, K. *ChemSusChem* **2020**, *13*, 4906–4910.
50. Maeda, K.; Teramura, K.; Masuda, H.; Takata, T.; Saito, N.; Inoue, Y.; Domen, K. *J. Phys. Chem. B* **2006**, *110*, 13107–13112.
51. Nishino, T.; Saruyama, M.; Li, Z.; Nagatsuma, Y.; Nakabayashi, M.; Shibata, N.; Yamada, T.; Takahata, R.; Yamazoe, S.; Hisatomi, T.;Domen, K.; Teranishi, T. *Chem. Sci.* **2020**, *11*, 6862–6867.
52. Yoshida, M.; Takanabe, K.; Maeda, K.; Ishikawa, A.; Kubota, J.; Sakata, Y.; Ikezawa, Y.; Domen, K. *J. Phys. Chem. C* **2009**, *113*, 10151–10157.
53. Maeda, K.; Abe, R.; Domen, K. *J. Phys. Chem. C* **2011**, *115*, 3057–3064.
54. Zhang, G.; Zang, S.; Wang, X. *ACS Catal.* **2015**, *5*, 941–947.
55. Lyu, H.; Hisatomi, T.; Goto, Y.; Yoshida, M.; Higashi, T.; Katayama, M.; Takata, T.; Minegishi, T.; Nishiyama, H.; Yamada, T.; Sakata, Y.; Asakura K.; Domen, K. *Chem. Sci.* **2019**, *10*, 3196–3201.
56. Kuang, Y.; Jia, Q.; Ma, G.; Hisatomi, T.; Minegishi, T.; Nishiyama, H.; Nakabayashi, M.; Shibata, N.; Yamada, T.; Kudo, A.; Domen, K. *Nat. Energy* **2016**, *2*, 16191.
57. Tabata, M.; Maeda, K.; Higashi, M.; Lu, D.; Takata, T.; Abe, R.; Domen, K. *Langmuir* **2010**, *26*, 9161–9165.
58. Abe, R.; Higashi, M.; Domen, K. *ChemSusChem* **2011**, *4*, 228–237.
59. Ma, S. S. K.; Maeda, K.; Abe, R.; Domen, K. *Energy Environ. Sci.* **2012**, *5*, 8390–8397.
60. Suzuki, H.; Nitta, S.; Tomita, O.; Higashi, M.; Abe, R. *ACS Catal.* **2017**, *7*, 4336–4343.
61. Iwase, Y.; Tomita, O.; Higashi, M.; Abe, R. *Sustain. Energy Fuels* **2017**, *1*, 748–754.
62. Murofushi, K.; Ogawa, K.; Suzuki, H.; Sakamoto, R.; Tomita, O.; Kato, K.; Yamakata, A.; Saeki, A.; Abe, R. *J. Mater. Chem. A* **2021**, *9*, 11718–11725.
63. Qi, Y.; Zhao, Y.; Gao, Y.; Li, D.; Li, Z.; Zhang, F.; Li, C. *Joule* **2018**, *2*, 2393–2402.
64. Miseki, Y.; Kusama, H.; Sugihara, H.; Sayama, K. *J. Phys. Chem. Lett.* **2010**, *1*, 1196–1200.
65. Nakada, A.; Suzuki, H.; Jhon, J.; Vequizo, M.; Ogawa, K.; Higashi, M.; Saeki, A.; Yamakata, A.; Kageyama, H.; Abe, R. *ACS Appl. Mater. Interfaces* **2019**, *11*, 45606–45611.

66. Paolella, A.; Faure, C.; Timochevskii, V.; Marras, S.; Bertoni, G.; Abdelbast, G.; Vijh, A.; Armand, M.; Zaghib, K. *J. Mater. Chem. A* **2017**, 18919–18932.
67. De Tacconi, N. R.; Rajeshwar, K.; Lezna, R. O. *Chem. Mater.* **2003**, *15*, 3046–3062.
68. Hurlbutt, K.; Wheeler, S.; Capone, I.; Pasta, M. *Joule* **2018**, *2*, 1950–1960.
69. Yamada, Y.; Oyama, K.; Gates, R.; Fukuzumi, S. *Angew. Chemie - Int. Ed.* **2015**, *54*, 5613–5617.
70. Aksoy, M.; Nune, S. V. K.; Karadas, F. *Inorg. Chem.* **2016**, *55*, 4301–4307.
71. Wu, X.; Wu, C.; Wei, C.; Hu, L.; Qian, J.; Cao, Y.; Ai, X.; Wang, J.; Yang, H. *ACS Appl. Mater. Interfaces* **2016**, *8*, 5393–5399.
72. Deng, L.; Qu, J.; Niu, X.; Liu, J.; Zhang, J.; Hong, Y.; Feng, M.; Wang, J.; Hu, M.; Zeng, L.; Zhang, Q.; Guo, L.; Zhu, T. *Nat. Commun.* **2021**, *12*, 2167.
73. Wang, W.; Gang, Y.; Hu, Z.; Yan, Z.; Li, W.; Li, Y.; Gu, Q. F.; Wang, Z.; Chou, S. L.; Liu, H. K.; Dou. S. X. *Nat. Commun.* **2020**, *11*, 980.
74. Lee, H. W.; Wang, R. Y.; Pasta, M.; Lee, S. W.; Liu, N.; Cui, Y. *Nat. Commun.* **2014**, *5*, 5280.
75. Fétiveau, L.; Paul, G.; Nicolas-Boluda, A.; Volatron, J.; George, R.; Laurent, S.; Muller, R.; Sancey, L.; Mejanelle, P.; Gloter, A.; Gazeau, F.; Catala, L. *Chem. Commun.* **2019**, *55*, 14844–14847.
76. Gotoh, A.; Uchida, H.; Ishizaki, M.; Satoh, T.; Kaga, S.; Okamoto, S.; Ohta, M.; Sakamoto, M.; Kawamoto, T.; Tanaka, H.; Tokumoto, M.; Hara, S.; Shiozaki, H.; Yamada, M.; Miyake, M.; Kurihara, M. *Nanotechnology* **2007**, *18*, 1–6.
77. Kong, B.; Selomulya, C.; Zheng, G.; Zhao, D. *Chem. Soc. Rev.* **2015**, *44*, 7997–8018.
78. Matsuda, T.; Moritomo, Y. *J. Nanotechnol.* **2012**, *2012*, 1–9.
79. Scholz, F.; Dostal, A. *Angew. Chem., Int. Ed. Engl.* **1995**, *34*, 2685–2687.
80. DeLongchamp., D. M.; Hammond, P. T. *Adv. Funct. Mater.* **2004**, *14*, 224–232.
81. Kholoud, E.; Watanabe, H.; Takahashi, A.; Emara, M. M.; Abd-El-Nabey, B. A.; Kurihara, M.; Tajima, K.; Kawamoto, T. *J. Mater. Chem. C* **2017**, *5*, 8921–8926.
82. Yoshino, K.; Kitajima, A.; Minami, N.; Kawamoto, T.; Tanaka, H. *Chem. Lett.* **2012**, *41*, 1473–1474.
83. Kitajima, A.; Tanaka, H.; Minami, N.; Yoshino, K.; Kawamoto, T.; Kitajima, A.; Minami, N.; Kawamoto, T.; Tanaka, H. *Chem. Lett.* **2012**, *41*, 1473–1474.
84. Takahashi, A.; Tanaka, H.; Parajuli, D.; Nakamura, T.; Minami, K.; Sugiyama, Y.; Hakuta, Y.; Ohkoshi, S. I.; Kawamoto, T. *J. Am. Chem. Soc.* **2016**, *138*, 6376–6379.
85. Varfolomeyev, S. D.; Matveyenko, V. N.; Kurochkin, I. N.; Karyakina, E. E.; Budashov, I. A.; Levchenko, V. A.; Puganova, E. A.; Karyakin, A. A. *Anal. Chem.* **2004**, *76*, 474–478.
86. Kaye, S. S.; Long, J. R. *J. Am. Chem. Soc.* **2005**, *127*, 6506–6507.

87. Reguera, L.; Krap, C. P.; Balmaseda, J.; Reguera, E. *J. Phys. Chem. C* **2008**, *112*, 15893–15899.
88. Wu, X.; Cao, Y.; Ai, X.; Qian, J.; Yang, H. *Electrochem. Commun.* **2013**, *31*, 145–148.
89. Lu, Y.; Wang, L.; Cheng, J.; Goodenough, J. B. *Chem. Commun.* **2012**, *48*, 6544–6546.
90. Pintado, S.; Goberna-Ferrón, S.; Escudero-Adán, E. C.; Galán-Mascarós, J. R. *J. Am. Chem. Soc.* **2013**, *135*, 13270–13273.
91. Goberna-Ferrón, S.; Hernández, W. Y.; Rodríguez-García, B.; Galán-Mascarós, J. R. *ACS Catal.* **2014**, *4*, 1637–1641.
92. Tabe, H.; Terashima, C.; Yamada, Y. *Catal. Sci. Technol.* **2018**, *8*, 4747–4756.
93. Alsaç, E. P.; Ülker, E.; Nune, S. V. K.; Dede, Y.; Karadas, F. *Chem. - A Eur. J.* **2018**, *24*, 4856–4863.
94. Tabe, H.; Terashima, C.; Yamada, Y. *Catal. Sci. Technol.* **2018**, *8*, 4747–4756.

Chapter 1

Metal Hexacyanoferrates as Oxidation Promoters for Realizing Efficient Photocatalytic Hydrogen Evolution on Metal Sulfide under Visible Light

1.1. Introduction

Visible-light-induced water splitting using semiconductor photocatalysts has attracted considerable attention owing to its potential for clean and sustainable H_2 production from water by utilizing abundant solar energy.[1–5] Among visible-light-responsive photocatalysts, various metal sulfides such as cadmium sulfide (CdS) have been extensively studied because of their narrow bandgaps for visible light absorption and appropriate band levels for both water oxidation and reduction.[1,3,4,6] However, most of them are prone to self-oxidation by photogenerated holes (e.g., $S^{2-} + 2h^+ \rightarrow S$).[7] Because their valence band maxima consist of less electronegative S-2p anions than O-2p ones, the photogenerated holes tend to oxidize such unstable S^{2-} anions. Therefore, the majority of photocatalytic H_2 evolution on metal sulfides has been realized in the presence of an irreversible electron donor such as S^{2-} and/or SO_3^{2-}.[8] One of the most attractive ways to achieve water splitting utilizing such metal sulfides is to employ them in Z-scheme water splitting systems.[5,9] Metal sulfides can be employed as H_2-evolution photocatalysts, coupled with an O_2 evolution photocatalyst via an electron mediator, as demonstrated by Kudo and co-workers, using $(CuGa)_{0.8}Zn_{0.4}S_2$ and $BiVO_4$ photocatalyst via $[Co(terpy)_3]^{3+/2+}$ (terpy: terpyridine).[10,11] However, the number of metal sulfides available in Z-scheme systems is still quite limited, probably due to the insufficient stability of metal sulfides during oxidation of the redox mediator (i.e., the occurrence of self-oxidative deactivation).

It has been recently demonstrated that the surface modification of CdS with cadmium hexacyanoferrate ($K_2Cd[Fe(CN)_6]$, denoted as CdHCF) endows CdS with the ability to generate H_2 stably in a Z-scheme system using $[Fe(CN)_6]^{3-/4-}$ redox mediator.[12] It was revealed that thin layers of CdHCF were formed *in situ* on the CdS surface during an initial period of photoirradiation accompanied by photocorrosion. The photogenerated holes in CdS initially oxidize S^{2-} and thereby generate Cd^{2+} cations dissolved from CdS in the solution; the Cd^{2+} spontaneously and immediately forms insoluble CdHCF species on the CdS surface by reacting with $[Fe(CN)_6]^{4-}$ anions in the solution. A series of experiments indicated that the CdHCF layers efficiently scavenged the photogenerated holes in CdS and facilitated the oxidation of $[Fe(CN)_6]^{4-}$ to $[Fe(CN)_6]^{3-}$ via the redox cycles of Fe^{III}/Fe^{II} in CdHCF. This function of CdHCF promotes the consumption of photogenerated holes in CdS and eventually suppresses further photocorrosion, enabling stable and efficient H_2 evolution on the CdS photocatalyst (Scheme 1-1). The CdHCF modification was also effective at enhancing H_2 evolution on other sulfide photocatalysts such as $ZnIn_2S_4$.[12] It should be noted that the CdHCF particles prepared in advance were loaded onto the surface of $ZnIn_2S_4$ photocatalyst via a simple impregnation method. This

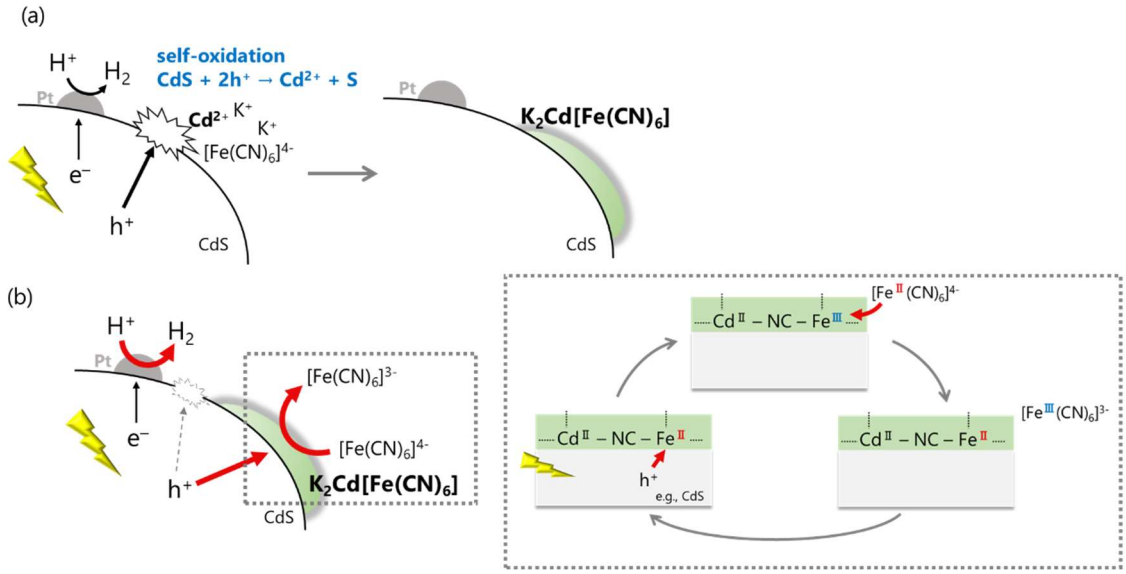

Scheme 1-1. Proposed mechanism of (a) CdHCF formation and (b) stable and efficient H_2 evolution over Pt/CdS photocatalyst modified with CdHCF.

is in stark contrast to the first report on CdS, in which the CdHCF layers were produced accompanied by photocorrosion, thus limiting the key element in hexacyanoferrate to toxic Cd.

CdHCF belongs to the metal hexacyanoferrate (MHCF)/Prussian blue analogue (PBA) family. MHCFs are a class of three-dimensional coordination polymers with the general formula $A_hM_k[Fe(CN)_6]_l \cdot mH_2O$ (*h, k, l, m*: composition ratios; A: alkali metal cation; M: (transition) metal cation), where M and Fe cations are bridged by linear cyanide (CN) ligands (Figure 1-1).[13] MHCFs are regarded as functional materials applicable to various research fields, and the improvement of their performance by metal cation substitution has been extensively studied.[14–17] These attractive features of MHCFs motivated us to explore other Cd-free MHCFs as oxidation promoters (i.e., boosters of photocatalytic H_2 evolution). In the present study, a series of MHCF particles containing different cations were prepared and employed as oxidation promoters of a $[Fe(CN)_6]^{4-}$ electron donor on a $ZnIn_2S_4$ photocatalyst. The fundamental properties of MHCFs, such as redox potential, were examined, and their influence on photocatalytic H_2 evolution is discussed.

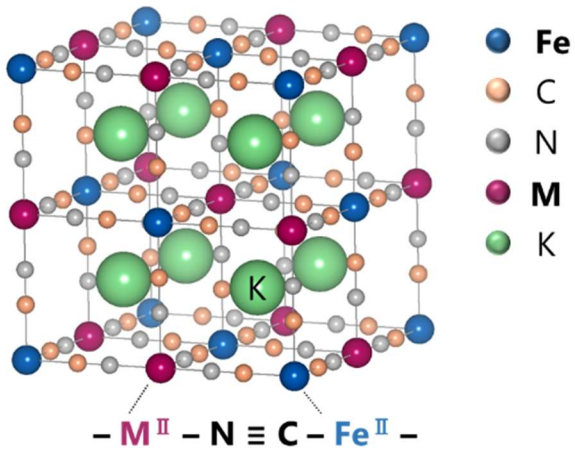

Figure 1-1. Typical structure of a MHCF with the composition of $K_2M[Fe(CN)_6]$.

1.2. Experimental

1.2.1. Materials

$ZnIn_2S_4$ was prepared by a hydrothermal method.[18] $Zn(NO_3)_2 \cdot 6H_2O$ (FUJIFILM Wako Pure Chemical Corporation, 99.5%), $In(NO_3)_3 \cdot 3H_2O$ (FUJIFILM Wako Pure Chemical Corporation, 98%), and CH_3CSNH_2 (FUJIFILM Wako Pure Chemical Corporation, 98%) were dissolved in Milli-Q water (75 mL). The pH of the obtained solution was adjusted to 2 with aqueous HCl (FUJIFILM Wako Pure Chemical Corporation, 1M). The solution was then transferred into a 100 mL Teflon-lined autoclave. The autoclave was sealed, heated to 433 K for 12 h, and then allowed to cool to room temperature (288–298 K). The yellow precipitate produced was centrifuged and thoroughly washed with Milli-Q water and ethanol (FUJIFILM Wako Pure Chemical Corporation, 99.5%) several times, and finally dried in the oven (308 K) under vacuum overnight. The obtained $ZnIn_2S_4$ powder was calcined at 1073 K for 4 h under Ar flow (20 mL min^{-1}). The as-prepared $ZnIn_2S_4$ particles were confirmed to be similar to those previously reported[18] (Figure 1-2). Hereafter, $ZnIn_2S_4$ will be denoted as ZIS for simplicity.

Metal hexacyanoferrate (MHCF, M = Mn, Fe, Co, Ni, Cu, Zn, Ag, In, and Cd) particles were synthesized by a conventional co-precipitation method.[19] An aqueous solution (50 mL) of $K_4[Fe(CN)_6] \cdot 3H_2O$ (FUJIFILM Wako Pure Chemical Corporation, 99.5%) (200 mM) was added to 50 mL of an aqueous solution of metal halide salts, such as $MnBr_2$ and $InCl_3 \cdot 4H_2O$ (50 mM). Then, the mixed solution was stirred for 50 min using a magnetic stirrer. The obtained precipitate, which formed immediately after mixing the two solutions, was collected by centrifugation and washed with Milli-Q water several times, and then dried in the oven (308 K) under vacuum overnight.

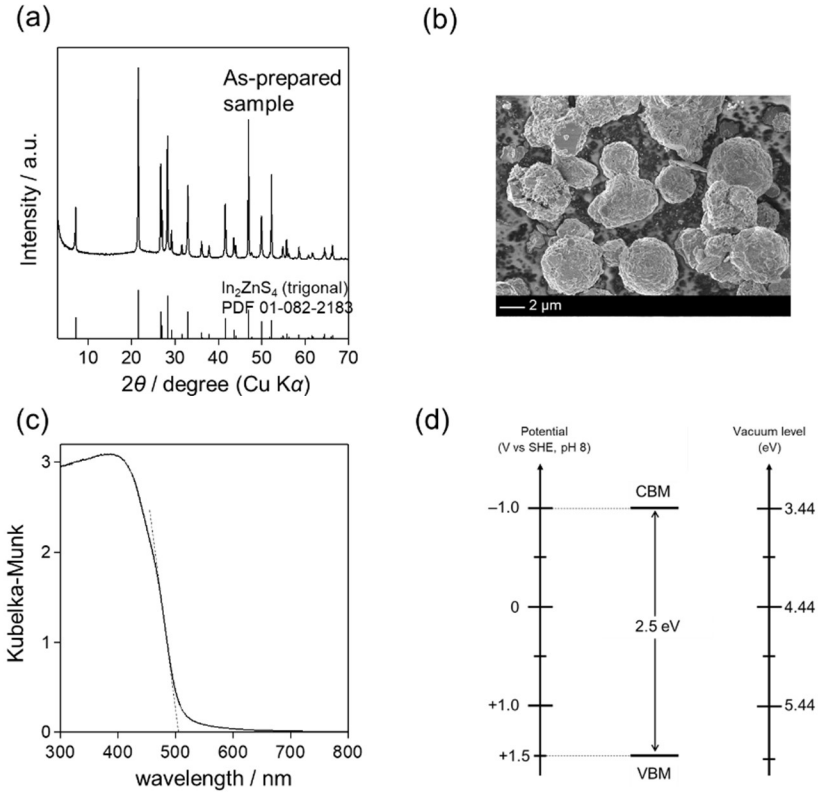

Figure 1-2. Characterization of the as-prepared $ZnIn_2S_4$: (a) XRD patterns, (b) SEM image, (c) UV-vis diffuse reflectance spectrum and (d) band edge position. The valence band maximum (VBM) was estimated from photoelectron yield spectroscopy, the band gap was determined from the absorption edge in Figure 1-2c, and the conduction band minimum (CBM) was calculated as CBM = VBM – band gap.

1.2.2. Surface modification

Particulate Pt as a water reduction cocatalyst was deposited on ZIS by an impregnation method from an aqueous solution containing an appropriate amount of $H_2PtCl_6 \cdot 6H_2O$ (FUJIFILM Wako Pure Chemical Corporation, 99.9%; 1 wt% Pt), followed by heating at 473 K for 2 h under H_2 flow (20 mL min^{-1}). The obtained samples are denoted as Pt/ZIS.

The Pt/ZIS powders were modified with MHCFs via impregnation and subsequent annealing. Pt/ZIS samples were immersed in water dispersed with a certain amount of previously prepared MHCFs (M = Mn, Fe, Co, Ni, Cu, Zn, Ag, In, and Cd). The solution was dried and then heated at 473 K for 0.5 h under Ar flow (20 mL min^{-1}). The loading amount of MHCFs was set to 26–30 mol% Fe to ZIS. The MHCF-modified sample is denoted as MHCF/Pt/ZIS.

1.2.3. Characterization

The prepared samples were characterized by powder X-ray diffraction (XRD; Mini Flex II, Rigaku, X-ray source; Cu Kα) measurements, UV-visible diffuse reflectance spectroscopy (UV-Vis DRS; V-650, JASCO), and attenuated total reflectance-Fourier transform infrared spectroscopy (ATR-FTIR, ATR; ATR Pro One, JASCO, FT-IR; FT-4200, JASCO) using a diamond prism. ATR-FTIR spectra were recorded against air as a background. The morphology of the samples was examined by scanning electron microscopy (SEM; NVision 40, Carl Zeiss- SIINT) and transmission electron microscopy (TEM; JEM-2100F, JEOL). The ionization energy was directly measured by photoelectron yield spectroscopy (BIP-KV201, Bunkoukeiki) in a vacuum ($<5 \times 10^{-2}$ Pa). The Brunauer-Emmett-Teller (BET) surface area was measured using a BELSORP-mini II (Microtrac BEL) at liquid nitrogen temperature (77 K).

1.2.4. Electrochemical measurement

MHCF (M = Mn, Fe, Co, Ni, Cu, Zn, Ag, In, and Cd)-deposited electrodes were prepared on fluorine-doped tin oxide (FTO) glasses using a squeegee method. A slurry of the respective samples in water was pasted on an FTO glass and then heated at 373 K for 1 h under Ar flow (20 mL min^{-1}). The coated area and the deposited amount were fixed at approx. 1.5 × 1.5 cm^2 and 0.5 ± 0.3 mg, respectively. Hereafter, the electrodes are denoted as MHCF/FTO.

Electrochemical measurements were performed in an aqueous borate buffer (BB) solution (0.1 M, pH 8.0) containing 10 mM K_2SO_4 (99.0%; FUJIFILM Wako Pure Chemical Corporation) as an electrolyte under an Ar atmosphere using a three-electrode cell. The prepared MHCF/FTO electrode as the working electrode, a Pt coil as the counter electrode, and Ag/AgCl as the reference electrode were connected to a potentiostat (VersaSTAT 4, AMETEK), and cyclic voltammograms were recorded. The potential of the electrode is reported against the standard hydrogen electrode (SHE).

$$E_{SHE} = E_{Ag/AgCl} + E^{\circ}_{Ag/AgCl} \; (E^{\circ}_{Ag/AgCl} = 0.204 \text{ V at } 298 \text{ K})$$

It is well known that the potential of the Ag/AgCl reference (3 M NaCl) is constant with respect to absolute potentials such as SHE.

1.2.5. Photocatalytic reaction

Photocatalytic reactions were conducted in a Pyrex side-irradiation-type cell connected to a closed gas circulation system. The prepared photocatalyst powder (0.05 g) was

suspended in 250 mL of BB solution (0.1 M, pH 8.0) containing $K_4[Fe(CN)_6]$ (5 mM) as an electron donor. Before the reaction, the suspensions were thoroughly degassed. The reaction solution was irradiated using a 300 W Xe lamp (Cermax, LX-300F) equipped with a cutoff filter (Hoya, L-42) and a cold mirror (Kenko, CM-1) (λ > 400 nm). The temperature of the reaction solution was maintained at 288 K by circulated cooling water. The evolved gases were analyzed by online gas chromatography (GC-8A, Shimadzu; thermal conductivity detector; column: MS 5A column; Ar carrier) directly connected to the closed gas circulation system.

1.3. Results and Discussion

1.3.1. Characterization of MHCF

Figure 1-3 shows XRD patterns of a series of MHCFs (M = Mn, Fe, Co, Ni, Cu, Zn, Ag, In or Cd). All MHCFs except for ZnHCF and AgHCF exhibit diffraction patterns similar to that of $K_2Co[Fe(CN)_6]$ (powder diffraction file, PDF), indicating that these MHCFs have the face-centered cubic structure with the formula $K_2M[Fe(CN)_6]$ (M = Co, Ni, Mn, Cu, Fe or Cd) or KIn[Fe(CN)]. The XRD pattern for ZnHCF indicates a $K_2Zn_3[Fe(CN)_6]$ phase with a rhombohedral structure. Although a detailed structural analysis of AgHCF has never been performed, the present AgHCF particles exhibit almost the same XRD pattern as that of previously reported AgHCF samples.[20] The ATR-FTIR spectra of the MHCF samples (Figure 1-4) contain absorption bands at 2050–2100 cm^{-1}, which are different from those of $K_4[Fe(CN)_6]\cdot 3H_2O$ (2044 cm^{-1}) and its oxidized form $K_3[Fe(CN)_6]$ (2117 cm^{-1}). These bands of MHCFs are assignable to the stretching vibration mode of C≡N in MHCFs,[13] thereby confirming that MHCFs include a three-dimensional framework made up of FeC_6 octahedra and MN_6 octahedra linked together by linear CN ligands.

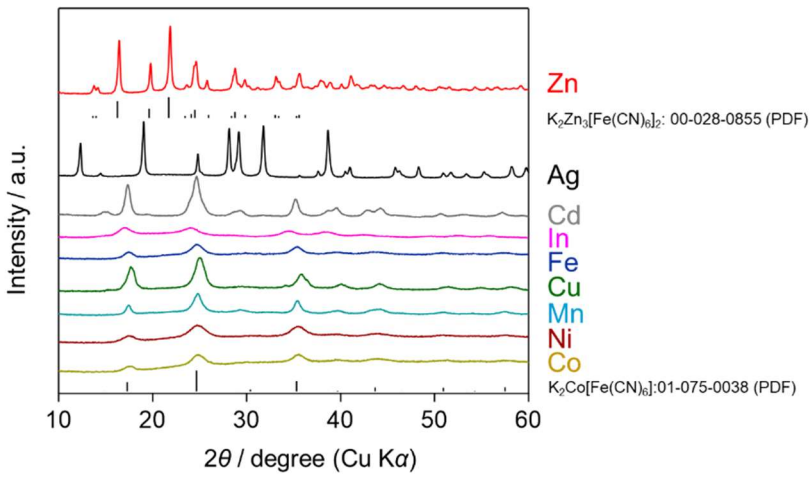

Figure 1-3. XRD patterns of various MHCFs (M = Mn, Fe, Co, Ni, Cu, Zn, Ag, In or Cd).

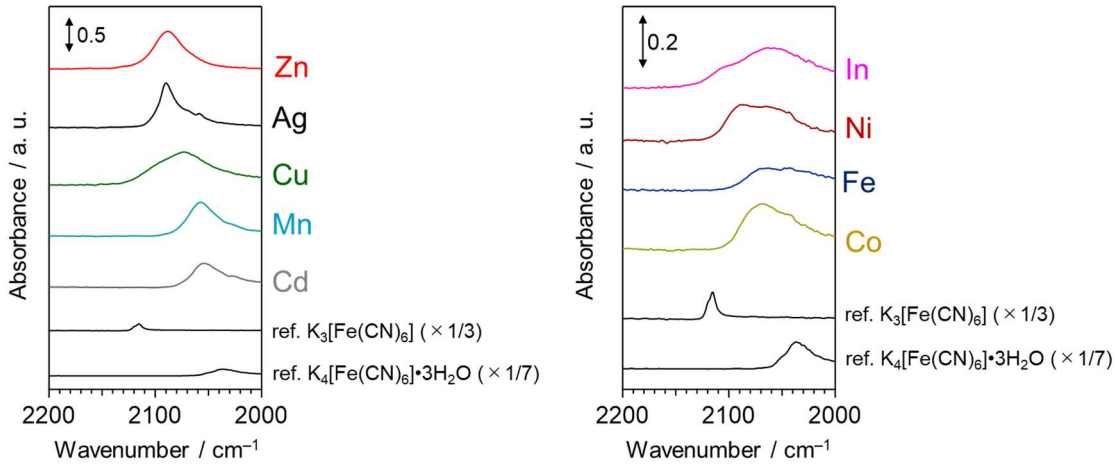

Figure 1-4. ATR-FTIR spectra of a series of MHCFs (M = Mn, Fe, Co, Ni, Cu, Zn, Ag, In or Cd).

Figure 1-5 shows the UV-vis diffuse reflectance spectra of the MHCFs, showing that the absorption properties vary significantly with the M cations. Some MHCFs (M = Co, Ni, Cu, Ag, and Fe) exhibit absorption in the visible light region (longer than 400 nm), which is most probably ascribed to intervalence charge transfer.[21] These visible-light absorptions overlap partially with those of ZIS, implying the occurrence of light shielding by these MHCFs when loaded on the surface of the ZIS photocatalyst. On the other hand, other MHCFs (M = Mn, Zn, and In) exhibit mainly absorption in the UV region.

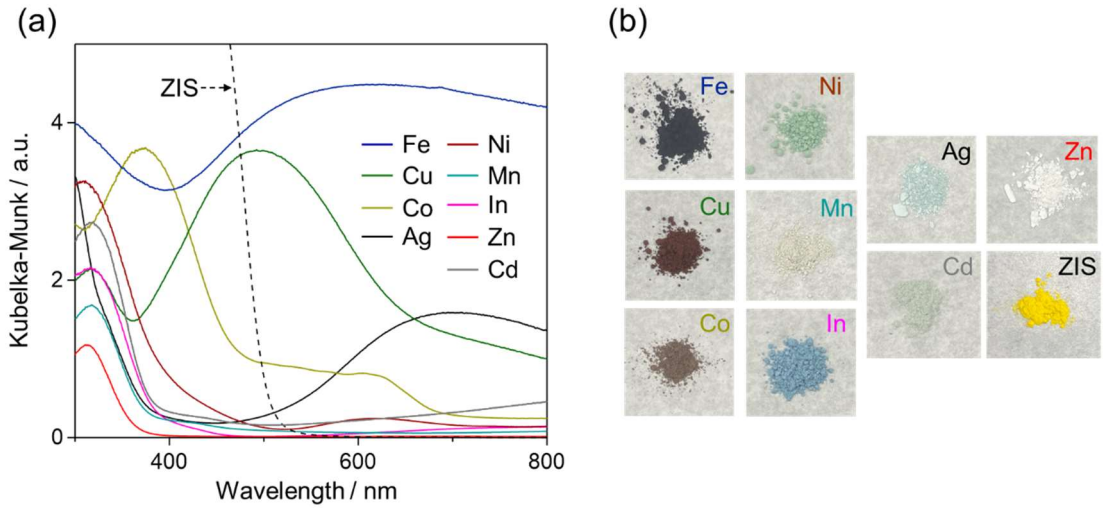

Figure 1-5. (a) UV-vis diffuse reflectance spectra and (b) photographs of various MHCFs (M = Mn, Fe, Co, Ni, Cu, Zn, Ag, In or Cd), along with those of ZIS.

Figure 1-6 shows SEM images of the MHCFs, along with their BET surface areas. Their particle sizes, morphologies, and specific surface areas vary depending on the type of M cations, although the same preparation procedures were employed. The origin of such significant changes in size and morphology is unclear at present. Given the very high BET surface areas of MnHCF and ZnHCF, these samples certainly consist of aggregated primary particles of a much smaller size than the other MHCFs.

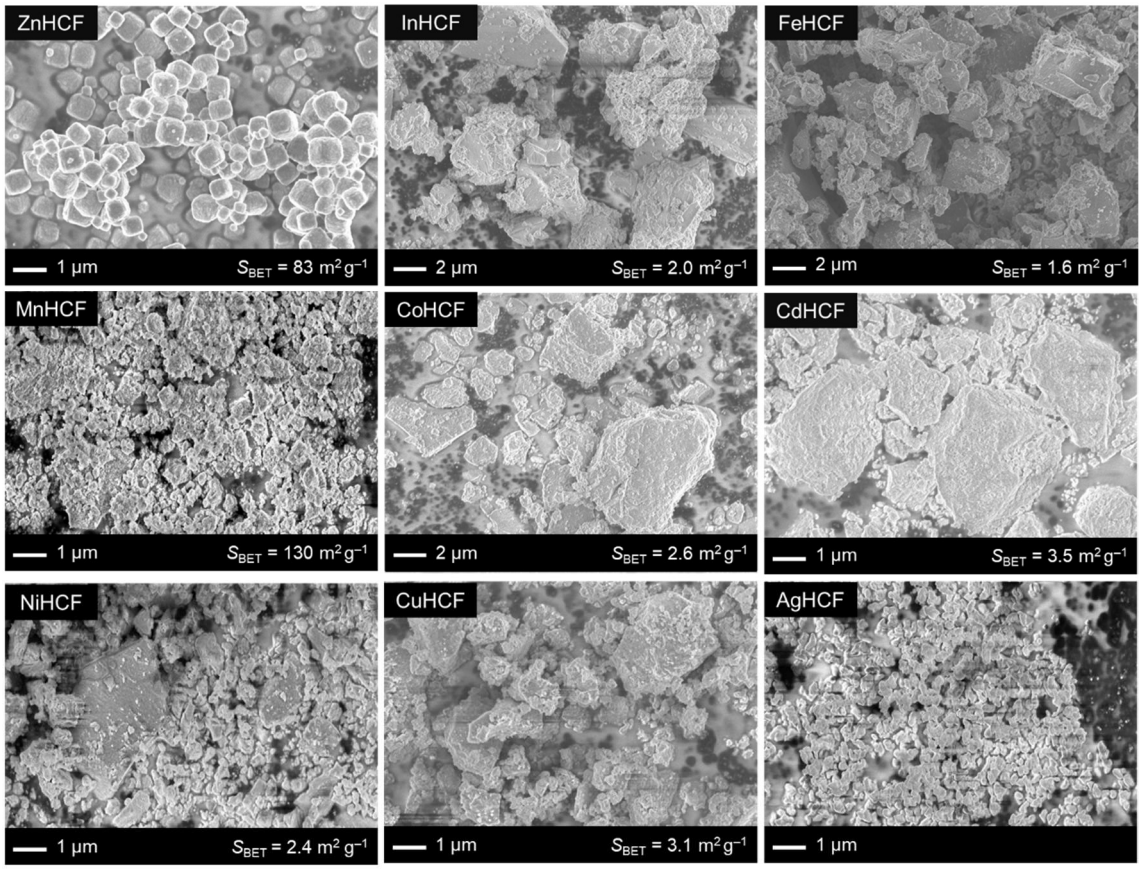

Figure 1-6. SEM images of MHCFs (M = Mn, Fe, Co, Ni, Cu, Zn, Ag, In or Cd).

Figure 1-7 shows the CV profiles of the MHCF-deposited FTO electrode in an aqueous borate buffer (BB) solution containing K_2SO_4 (10 mM). All MHCFs, except AgHCF, show relatively stable redox behavior. A pair of redox waves in MHCFs containing any one of Cd, In, Zn, Mn, or Ni can be ascribed to Fe^{III}/ Fe^{II},[22] while that in CoHCF is derived from Co^{III}/Co^{II}.[23] On the other hand, FeHCF exhibits two pairs of redox waves in FeHCF because both the N-coordinated and C-coordinated Fe species are electroactive. The peaks observed at lower potential or higher potential are assignable to Fe^{III}/Fe^{II} in the former or latter, respectively.[24]

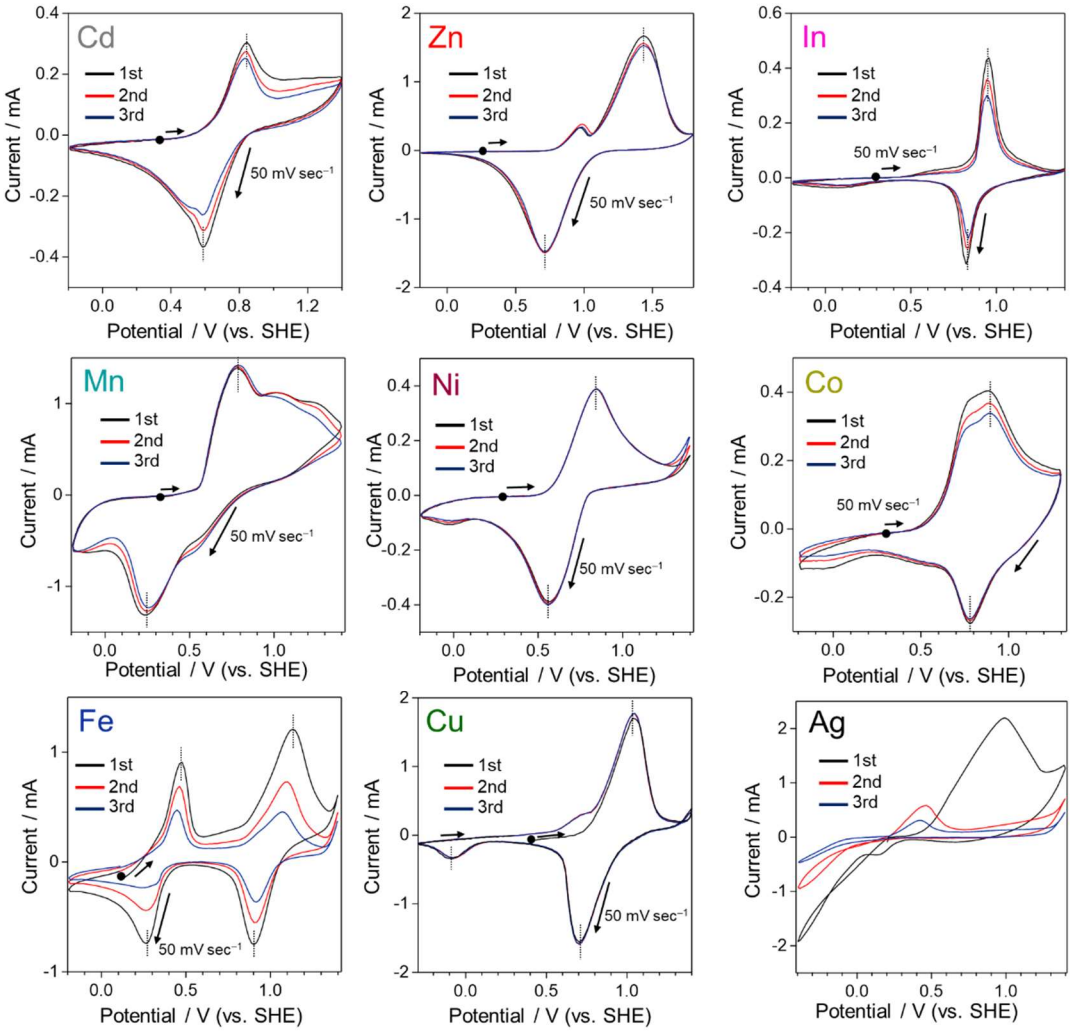

Figure 1-7. CV profiles of the FTO electrode deposited with MHCFs (M = Cd, Zn, In, Mn, Ni, Co, Fe, Cu and Ag) in 40 mL of aqueous borate buffer solution (0.1 M, pH 8.0) containing K_2SO_4 (10 mM).

Taking the MHCF with a composition of $K_2M^{II}[Fe^{II}(CN)_6]$ (M^{II}: electro-inactive cation) as an example, the redox reaction occurring on MHCF can be described by Equation 1, whereby divalent and trivalent iron species coexist during the reaction, as suggested in previous studies:

$$K_2M[Fe^{II}(CN)_6] \rightleftarrows K_{2-x}In[Fe^{II}_{1-x}Fe^{III}_{x}(CN)_6] + xK^+ + xe^-, \quad \text{(Eq. 1)}$$

where x is the number of moles of reacted electrons.

As for CuHCF, it shows a reduction current peak at approximately –0.1 V vs. SHE, in addition to the reversible redox wave for Fe^{III}/Fe^{II} with an $E_{1/2}$ value of approximately

0.88 V vs. SHE. The corresponding oxidation peak is observed at approximately 0.7 V vs. SHE after the second scan cycle, while the separation between reduction and oxidation is unexpectedly large. Although the reasons for this redox behavior, including large separation, are unclear at present, this additional redox couple in CuHCF is most probably ascribed to Cu^{II}/Cu^{I}. Unlike other MHCFs, AgHCF shows irreversible redox behavior; the intensity of the peaks corresponding to both oxidation and reduction drastically decreases after the 2nd cycle, indicating that some irreversible reactions occurred.

Table 1 summarizes the physicochemical and electrochemical properties of various MHCFs. The redox potential E_{redox} was calculated as $E_{redox} = (E_a + E_p)/2$, where E_a and E_p are the anodic and cathodic peak potentials, respectively. As illustrated in Figure 1-8, the redox potentials of Fe^{III}/Fe^{II} in MHCF (M = Fe, Mn, Ni, Cd, Cu, In, Zn) and Co^{III}/Co^{II} in CoHCF are located between the valence band maximum (VBM) of ZIS (1.5 V vs. SHE) and the redox potential of $[Fe(CN)_6]^{3-}/[Fe(CN)_6]^{4-}$ couple (0.36 V vs. SHE). The energy diagram fulfills the thermodynamic requirements for promoting H_2 on ZIS photocatalysts in the presence of $[Fe(CN)_6]^{4-}$ electron donors, as previously reported for CdHCF. In other words, these MHCFs have the potential to capture photogenerated holes in ZIS and oxidize $[Fe(CN)_6]^{4-}$ to $[Fe(CN)_6]^{3-}$.

Table 1-1. Summary of properties of MHCFs

M in MHCF	Crystal structure	Fe/M	S_{BET} / $m^2\ g^{-1}$	redox species	E_{redox} / V_{SHE}	ΔE_p [b] / mV	p_a [c] / mA
Mn	cubic	1	130	Fe^{III}/Fe^{II}	0.52	551	1.40
Cd	cubic	1	3.5	Fe^{III}/Fe^{II}	0.72	263	0.27
Cu	cubic	1	3.1	Fe^{III}/Fe^{II} Cu^{II}/Cu^{I}	0.88 0.31	350 611	1.77 –
Co	cubic	1	2.6	Co^{III}/Co^{II}	0.83	69	0.37
Ni	cubic	1	2.4	Fe^{III}/Fe^{II}	0.71	283	0.39
Fe	cubic	1	1.6	Fe^{III}/Fe^{II} (N) [a] Fe^{III}/Fe^{II} (C) [a]	0.40 1.02	213 229	0.69 0.73
In	cubic	1	2.0	Fe^{III}/Fe^{II}	0.90	105	0.36
Zn	rhombohedral	2/3	83	Fe^{III}/Fe^{II}	0.99	709	1.55

[a] Fe^{III}/Fe^{II} (N) and Fe^{III}/Fe^{II} (C) represent the N-coordinated and C-coordinated Fe species, respectively.

[b] ΔE_p stands for peak separation. $\Delta E_p = E_a - E_p$.

[c] p_a stands for the anodic peak current.

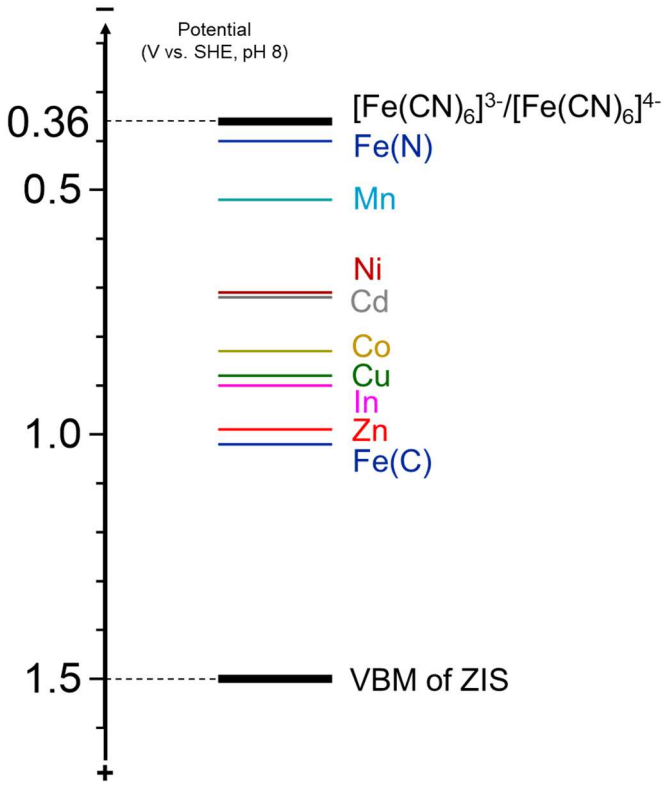

Figure 1-8. Schematic energy diagram of the VBM of ZIS, the redox potential of MHCFs (M = Fe, Mn, Ni, Cd, Co, Cu, In or Zn), and the redox potential of $[Fe(CN)_6]^{3-}$ /$[Fe(CN)_6]^{4-}$. Note that FeHCF has the two redox potentials of N-coordinated and C-coordinated Fe species.

1.3.2. Effects of modification with MHCF on H_2 evolution activity of Pt/$ZnIn_2S_4$

Figure 1-9 shows SEM images of Pt/ZIS particles modified with any one of the various MHCFs (MHCF/Pt/ZIS), in which the surfaces of large Pt/ZIS particles are considerably covered by smaller particles of MHCFs. The ATR-FTIR spectra (Figure 1-10) and XRD patterns (Figure 1-11) of MHCF/Pt/ZIS confirm that the physiochemical properties of MHCFs and $ZnIn_2S_4$ remained unchanged after the MHCF particles were loaded onto Pt/ZIS.

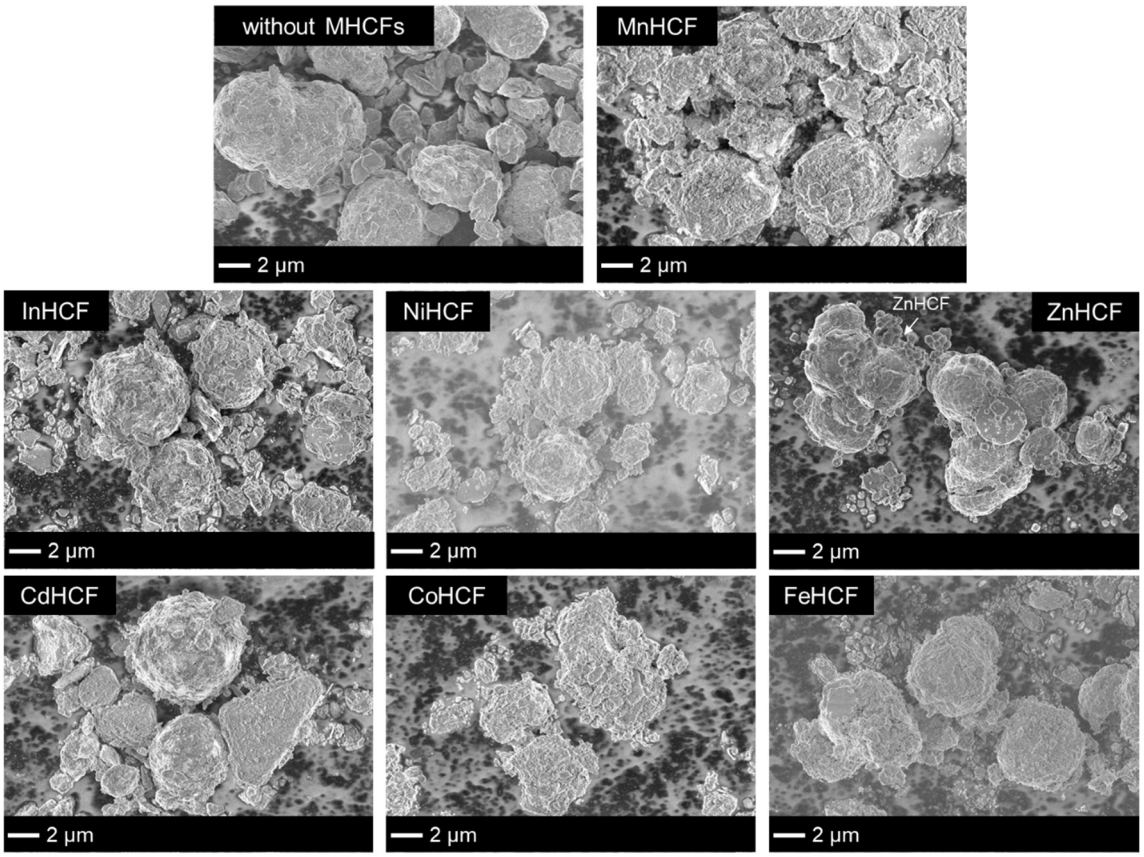

Figure 1-9. SEM images of Pt/ZIS modified with any one of various MHCFs (M = Mn, In, Ni, Zn, Cd, Co or Fe), along with that of Pt/ZIS ("without MHCFs").

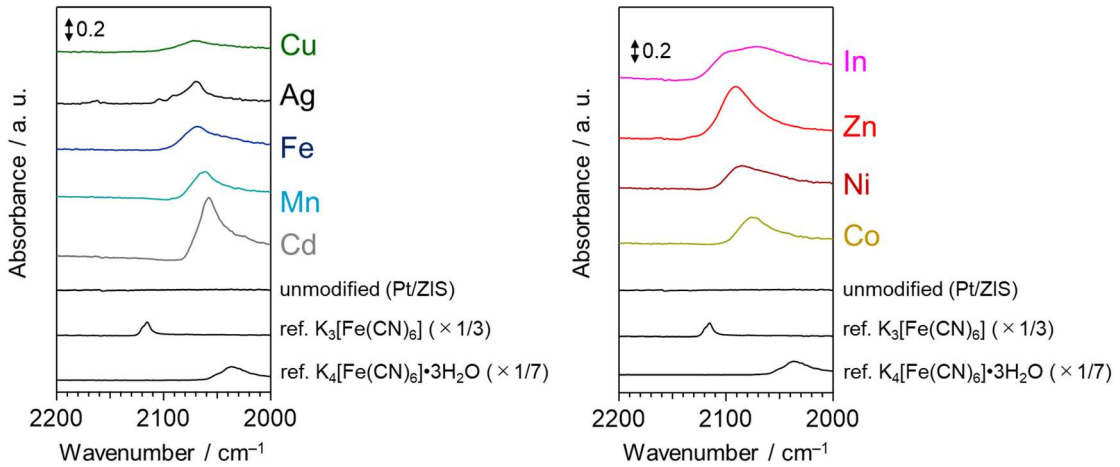

Figure 1-10. ATR-FTIR spectra of MHCF/Pt/ZIS, along with those of unmodified Pt/ZIS, $K_3[Fe(CN)_6]$ and $K_4[Fe(CN)_6]$.

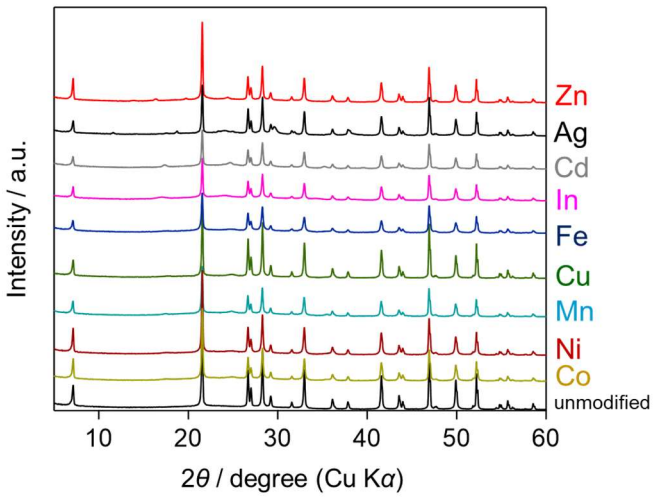

Figure 1-11. XRD patterns of MHCF/Pt/ZIS, along with that of unmodified Pt/ZIS.

Figure 1-12a shows the time courses of H_2 evolution using a series of MHCF/Pt/ZIS photocatalysts in the presence of $[Fe(CN)_6]^{4-}$ as an electron donor under visible-light irradiation. The initial rates are summarized in Figure 1-12b. It was revealed that various MHCFs (M = Mn, In, Co, Fe, Ni, Zn), other than CdHCF, can enhance H_2 evolution on Pt/ZIS, while the degree of their enhancement depends on the M in MHCFs. By contrast, modification with AgHCF or CuHCF completely suppressed photocatalytic H_2 evolution on Pt/ZIS. This deactivation can be understood by the redox behavior of these MHCFs, as shown in Figure 1-7. The irreversible CV behavior of AgHCF, specifically observed at the 1st anodic scan, strongly suggests oxidative decomposition (or deactivation) by photogenerated holes in ZIS. The formed inactive layer probably suppresses the subsequent reaction of holes with $[Fe(CN)_6]^{4-}$ in the solution. Although the CuHCF/FTO electrode exhibited stable redox cycles of $Fe^{III/II}$ with a redox potential suitable for the present reaction, it showed an additional redox cycle likely due to $Cu^{II/I}$, which is different from other MHCFs. Therefore, the most plausible reason for the suppressed H_2 evolution is that the photoexcited electrons in ZIS preferentially reduce the Cu^{II} species in CuHCF instead of water (or H^+).

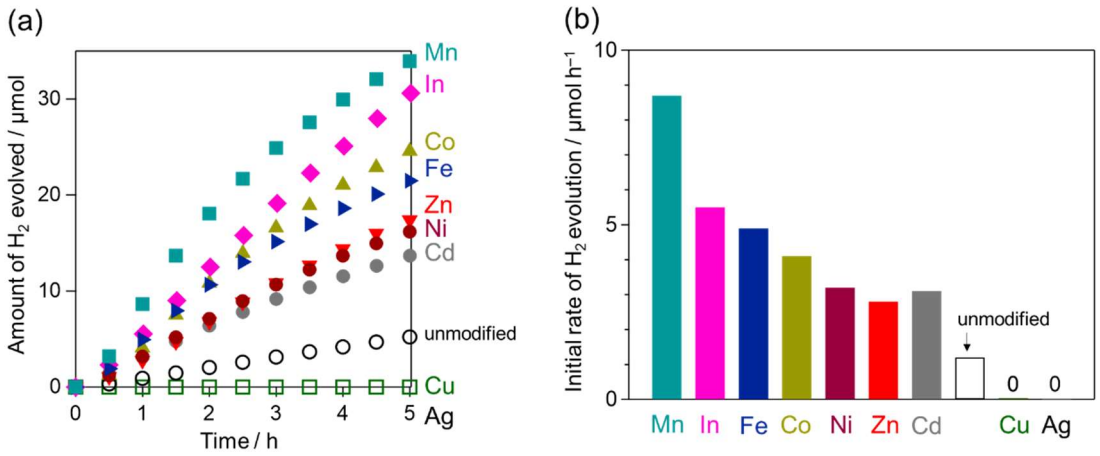

Figure 1-12. (a) Time courses and (b) initial rates of H_2 evolution over MHCF/Pt/ZIS (0.05 g) in aqueous BB solution (250 mL, 0.1 M, pH 8.0) containing $K_4[Fe(CN)_6]$ (5 mM) under visible light irradiation ($\lambda > 400$ nm).

By contrast, the MHCFs (M = Mn, In, Fe, Ni, Zn, and Cd) that enhanced photocatalytic H_2 evolution exhibited stable redox cycles of $Fe^{III/II}$ or $Co^{III/II}$, indicating the importance of stable redox cycles in enabling the MHCFs to be promoters of $[Fe(CN)_6]^{4-}$ oxidation. Although the light-shielding effect of cocatalysts sometimes affects the photocatalytic activity, no simple correlation between the H_2 evolution activities and the light absorption of MHCFs (Figure 1-5) was observed in the present study. As seen in Figure 1-8 and Table 1-1, the redox potentials of Fe^{III}/Fe^{II} in MHCF (M = Fe, Mn, Ni, Cd, In, Zn) and Co^{III}/Co^{II} in MHCF (M = Co) are located at different positions. The difference in redox potentials causes a change in the energy gaps simultaneously for two processes: (1) the oxidation of Fe^{II} or Co^{II} species in MHCF by photogenerated holes in ZIS and (2) the oxidation of $[Fe(CN)_6]^{4-}$ in the solution by Fe^{III} or Co^{III} species generated via process (1). Such a change in energy gaps would affect the efficiency of each electron transfer process and, eventually, the rate of H_2 evolution. However, there is no simple relationship between the redox potential and the rate of H_2 evolution. This is possibly because the energy gaps in the two processes are simultaneously and inversely changed, i.e., the increased gap in process (1) decreases the gap in process (2). Another plausible reason for the elusive influence of redox potential on H_2 evolution is a greater impact of other properties of the MHCFs on the electron transfer processes, such as resistance or particle size. For example, ZnHCF/FTO (see Table 1-1) exhibited the widest peak separation, $\Delta E_p = E_{pa} - E_{pc}$, among the MHCFs used in the present study, suggesting that the redox cycles in ZnHCF should be slower than the other MHCFs, thereby providing the lowest enhancement in H_2 evolution (except for the

Ag and Cu cases). In contrast, InHCF, FeHCF, and CoHCF with a narrower ΔE_p than that of ZnHCF probably provide greater improvement in H_2 evolution. The particle sizes or BET surface areas of MHCFs should also be significant factors for improvement in H_2 evolution activity. Although MnHCF has a wider ΔE_p, it provided the highest H_2 evolution rate among the MHCFs examined in the present study. The BET surface area of MnHCF is the largest (Table 1-1); therefore, MnHCF probably has the highest concentration of active sites for $[Fe(CN)_6]^{4-}$ oxidation. This assumption is supported by the larger value of p_a than those of MHCFs with lower specific surface area (except for ZnHCF), as listed in Table 1-1. Thus, MnHCF/Pt/ZIS exhibited highest H_2 evolution activity despite a wider ΔE_p in MnHCF. To clarify the impact of each property on the H_2 evolution rate, more detailed and systematic experiments employing MHCF samples with similar values of at least one of the fundamental properties, such as particle size, will be required.

1.4. Conclusion

In the present study, a series of metal hexacyanoferrates (MHCFs) were deposited on a metal sulfide photocatalyst, $ZnIn_2S_4$ (ZIS), and the relationship between the types of MHCFs modified on ZIS and the photocatalytic H_2 evolution activity was examined. It was revealed that various MHCFs (M = Mn, In, Fe, Co, Ni, Zn) as well as previously reported CdHCF functioned as oxidation promoters of the $[Fe(CN)_6]^{4-}$ electron donor, and therefore improved the photocatalytic H_2 evolution activity of Pt-loaded ZIS. From electrochemical measurements of MHCF-deposited electrodes, it was elucidated that the key to promotion of H_2 evolution by modification with MHCFs was stable redox cycles of Fe^{III}/Fe^{II} in the MHCFs (M = Mn, In, Fe, Ni, or Zn) and Co^{III}/Co^{II} in CoHCF with the redox potential located between the valence band maxima of photocatalyst materials and the redox potential of $[Fe(CN)_6]^{3-}/[Fe(CN)_6]^{4-}$. The peak separation ($\Delta E_a$) of the redox couple, which reflects the rate of redox reactions and the particle sizes (or specific surface area), which are associated with the concentration of the active sites, is also critical for boosting the oxidation of the $[Fe(CN)_6]^{4-}$ electron donor. The design of MHCFs based on the present study will allow for efficient photocatalytic water splitting employing non-oxide materials such as metal sulfides as H_2 evolution photocatalysts.

References

1. Maeda, K.; Domen, K. J. Phys. Chem. C 2007, 111, 7851–7861.
2. Esswein, A. J.; Nocera, D. G. Chem. Rev. 2007, 107, 4022–4047.
3. Osterloh, F. E. Chem. Mater. 2008, 20, 35.
4. Kudo, A.; Miseki, Y. Chem. Soc. Rev. 2009, 38, 253–278.
5. Abe, R. J. Photochem. Photobiol. C Photochem. Rev. 2010, 11, 179–209.
6. Takayama, T.; Tsuji, I.; Aono, N.; Harada, M.; Okuda, T.; Iwase, A.; Kato, H.; Kudo, A. Chem. Lett. 2017, 46, 616–619.
7. Buehler, N.; Meier, K.; Reber, J. F. J. Phys. Chem. 1984, 88, 3261–3268.
8. Bao, N.; Shen, L.; Takata, T.; Domen, K.; Gupta, A.; Yanagisawa, K.; Grimes, C. A. J. Phys. Chem. C 2007, 111, 17527–17534.
9. Wang, Y.; Suzuki, H.; Xie, J.; Tomita, O.; Martin, D. J.; Higashi, M.; Kong, D.; Abe, R.; Tang, J. Chem. Rev. 2018, 118, 5201–5241.
10. Kato, T.; Hakari, Y.; Ikeda, S.; Jia, Q.; Iwase, A.; Kudo, A. J. Phys. Chem. Lett. 2015, 6, 1042–1047.
11. Iwashina, K.; Iwase, A.; Ng, Y. H.; Amal, R.; Kudo, A. J. Am. Chem. Soc. 2015, 137, 604–607.
12. Shirakawa, T.; Higashi, M.; Tomita, O.; Abe, R. Sustain. Energy Fuels 2017, 1, 1065–1073.
13. De Tacconi, N. R.; Rajeshwar, K.; Lezna, R. O. Chem. Mater. 2003, 15, 3046–3062.
14. Lu, Y.; Wang, L.; Cheng, J.; Goodenough, J. B. Prussian Blue: Chem. Commun. 2012, 48, 6544–6546.
15. Goberna-Ferrón, S.; Hernández, W. Y.; Rodríguez-García, B.; Galán-Mascarós, J. R. ACS Catal. 2014, 4, 1637–1641.
16. Takahashi, A.; Tanaka, H.; Parajuli, D.; Nakamura, T.; Minami, K.; Sugiyama, Y.; Hakuta, Y.; Ohkoshi, S. I.; Kawamoto, T. J. Am. Chem. Soc. 2016, 138, 6376–6379.
17. Tabe, H.; Kitase, A.; Yamada, Y. Appl. Catal. B Environ. 2019, 262, 118101.
18. Chai, B.; Peng, T.; Zeng, P.; Zhang, X.; Liu, X. J. Phys. Chem. C 2011, 115, 6149–6155.
19. Rubin, H. D.; Arent, D. J.; Humphrey, B. D.; Bocarsly, A. B. J. Electrochem. Soc. 1987, 134, 93–101.
20. Zhang, L.; Chen, L.; Zhou, X.; Liu, Z. Sci. Rep. 2015, 5, 18263.
21. Kong, B.; Selomulya, C.; Zheng, G.; Zhao, D. Chem. Soc. Rev. 2015, 44, 7997–8018.
22. Scholz, F.; Dostal, A. Angew. Chem., Int. Ed. Engl. 1995, 34, 2685–2687.
23. Wu, X.; Wu, C.; Wei, C.; Hu, L.; Qian, J.; Cao, Y.; Ai, X.; Wang, J.; Yang, H. ACS Appl. Mater. Interfaces 2016, 8, 5393–5399.
24. Karyakin, A. A. Electroanalysis 2001, 13, 813–819.

Chapter 2

A Stepwise Modification with Metal Hexacyanoferrate Layers for Improving H_2 Evolution on Metal Sulfide Photocatalysts

2.1. Introduction

As described in the introduction of Chapter 1, it has been recently revealed that the surface modification of CdS with a cadmium hexacyanoferrate, $K_2Cd[Fe(CN)_6]$ (CdHCF), enables CdS to function as stable H_2-evolving photocatalyst in Z-scheme system water splitting using $[Fe(CN)_6]^{3-/4-}$ redox mediator.[1] The effective thin layers of CdHCF were spontaneously formed on the surface via the photocorosion of CdS ($CdS + 2h^+ \rightarrow Cd^{2+} + S$) in the initial period of photoirradiation (Scheme 2-1). The dissolved Cd^{2+} cations reacted with $[Fe(CN)_6]^{4-}$ anions in the solution to generate the insoluble CdHCF species on the CdS surface. The CdHCF layers efficiently scavenged the photogenerated holes in CdS and also facilitated the oxidation of $[Fe(CN)_6]^{4-}$ to $[Fe(CN)_6]^{3-}$ via the redox cycles of Fe^{III}/Fe^{II} in CdHCF. This function of CdHCF promotes $[Fe(CN)_6]^{4-}$ oxidation and eventually suppressed the further photocorrosion, enabling the stable and efficient H_2 evolution on CdS photocatalyst.

In Chapter 1, it was revealed that the modification of $ZnIn_2S_4$ surface by various metal hexacyanoferrates (MHCF; M = Mn, In, Fe, Co, Ni, Zn) other than CdHCF via an simple impregnation promoted $[Fe(CN)_6]^{4-}$ oxidation and thereby realized efficient H_2 evolution. The results suggested that particle sizes of MHCF particles, not only their redox potentials, affected the H_2 evolution efficiency. It is well-known that the particle size and dispersion of metal or metal oxide cocatalysts effect remarkably on the photocatalytic activities.[2–4] Thus, a new method enabling modification with smaller particles and/or thin layer of MHCFs is highly desirable for further improvement of H_2 evolution activity. In this chapter, the present author has explored a stepwise method for

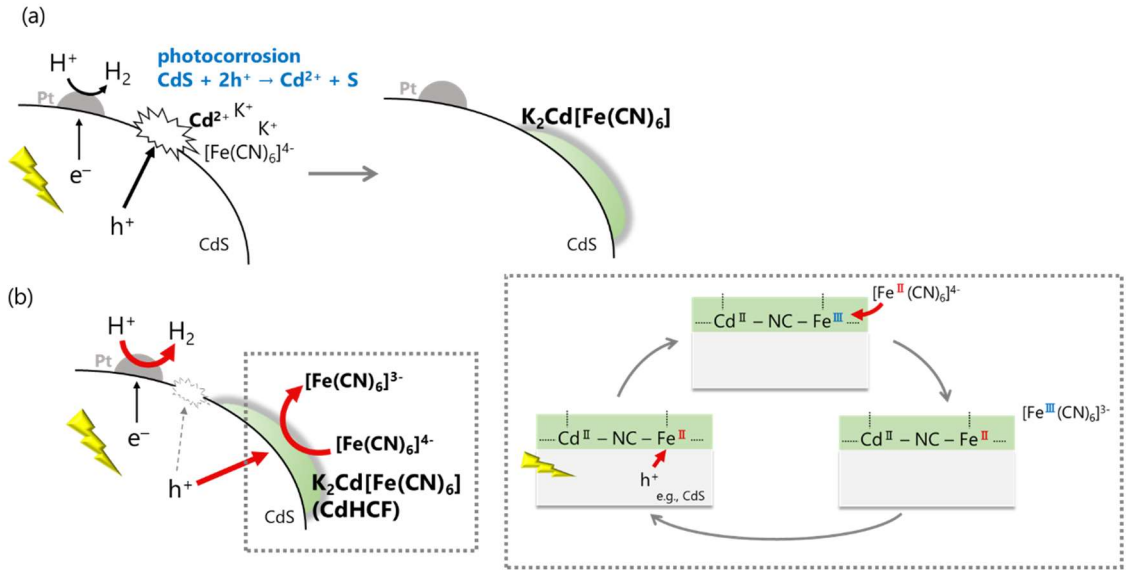

Scheme 2-1. Proposed mechanism of (a) CdHCF formation and (b) stable and efficient H_2 evolution over CdHCF-modified Pt/CdS photocatalyst.

MHCF modification, which was inspired by the spontaneous formation of CdHCF via the photocorrosion of CdS (Scheme 2-1a). At the first step, metal species are loaded on a photocatalyst via an impregnation using an aqueous solution containing metal cation precursors (typically, metal halides). At the second step, the samples loaded with metal cation species were added into aqueous $[Fe(CN)_6]^{4-}$ solution, in which metal cation species react with $[Fe(CN)_6]^{4-}$ to MHCF on the photocatalyst surface. The H_2 evolution activity of Pt-loaded $ZnIn_2S_4$ modified with MHCFs via the newly-developed method was compared with those of samples prepared via the conventional loading of preliminary-prepared MHCF particles.

2.2. Experimental

2.2.1. Sample preparation

$ZnIn_2S_4$ was prepared by a hydrothermal method[5] and subsequent annealing, as described in Chapter 1. Hereafter, $ZnIn_2S_4$ will be denoted as ZIS for simplicity. Metal hexacyanoferrate (MHCF, M = Mn, Co, In, Zn, or Cd) particles were synthesized via the same procedure in Chapter 1 by referring a conventional coprecipitation method.[6]

2.2.2. Surface modification

2.2.2.1. Deposition of Pt cocatalyst

Pt nanoparticles as water reduction cocatalysts were deposited on ZIS by an impregnation method using a $H_2PtCl_6 \cdot 6H_2O$ and subsequently heating under H_2 flow, as described in Chapter 1. The obtained samples are denoted Pt/ZIS.

2.2.2.2. Preparation of metal hexacyanoferrate-modified Pt/ZIS（MHCF/Pt/ZIS）

Direct modification (conventional method)

Pt/ZIS powders were modified with preliminarily-prepared MHCF particles by an impregnation method. Pt/ZIS samples were immersed in a water dispersed with a certain amount of MHCF (M = Mn, Co, In, Zn, or Cd) powders. The solution was dried and then heated at 473 K for 0.5 h under Ar flow (20 mL min^{-1}). Unless otherwise mentioned, the loading amount of MHCFs was set to 26–30 mol% Fe to ZIS. The MHCF-modified sample is denoted as MHCF(d)/Pt/ZIS.

Stepwise modification (new method)

Pt/ZIS particles were suspended in an aqueous solution containing an appropriate amount of metal salts such as $MnBr_2$ and $InCl_3 \cdot 4H_2O$. The solution was dried and then heated at 473 K for 0.5 h under Ar flow (20 mL min^{-1}). Then, the obtained sample was dispersed

in borate buffer (BB) solution (0.1 M, 250 mL, pH 8.0) containing $K_4[Fe(CN)_6]$ (5 mM), and then the mixed solution was stirred for 0.75 h to allow the metal species on the surface to react with $[Fe(CN)_6]^{4-}$. The sample was collected by the centrifugation and washed by Milli-Q water several times, and then dried in the oven (308 K) under vacuum overnight. Unless otherwise mentioned, the loading amount of MHCFs was set to 26–30 mol% Fe to ZIS. They will be denoted as MHCF(s)/Pt/ZIS.

2.2.3. Characterization of materials

The prepared samples were characterized by attenuated total reflectance-Fourier transform infrared spectroscopy (ATR-FTIR, ATR; ATR Pro One, JASCO, FT-IR; FT-4200, JASCO) using a diamond prism. ATR-FTIR spectra were recorded against air as a background. The morphology of the samples was examined by scanning electron microscopy (SEM; NVision 40, Carl Zeiss- SIINT) and transmission electron microscopy (TEM; JEM-2100F, JEOL).

2.2.4. Photocatalytic reactions

Photocatalytic reactions were conducted in a Pyrex side-irradiation-type cell connected to a closed gas circulation system. The prepared photocatalyst powder (0.05 g) was suspended in 250 mL of BB solution (0.1 M, pH 8.0) containing $K_4[Fe(CN)_6]$ (5 mM) as an electron donor. Before the reaction, the suspensions were thoroughly degassed. The reaction solution was irradiated using a 300 W Xe lamp (Cermax, LX-300F) equipped with a cutoff filter (Hoya, L-42) and a cold mirror (Kenko, CM-1) (λ > 400 nm). The temperature of the reaction solution was maintained at 288 K by circulated cooling water. The evolved gases were analyzed by online gas chromatography (GC-8A, Shimadzu; thermal conductivity detector; column: MS 5A column; Ar carrier) directly connected to the closed gas-circulation system. The amount of $[Fe(CN)_6]^{3-}$ generated during the reaction was measured by using a UV-Vis spectrophotometer (UV-1800, Shimadzu).

2.3 Results and Discussion

2.3.1. Characterization of Pt/ZIS modified with MHCFs by the stepwise method

Pt/ZIS photocatalysts were modified with MHCFs (M = Mn, In, Co, Zn, Cd) by the stepwise method, in which the Pt/ZIS powders were firstly modified with each metal salt such as $ZnBr_2$ and then stirred in aqueous $K_4[Fe(CN)_6]$ solution to form MHCFs on the surface of ZIS. Figure 2-1a shows ATR-FTIR spectra of Pt/ZIS modified with these MHCFs via the stepwise method (MHCF(s)/Pt/ZIS). Those of Pt/ZIS modified with preliminarily-prepared MHCFs (direct method) are also shown in Figure 2-1b. The

spectra of MHCF(s)/Pt/ZIS exhibit the absorption bands at 2050–2100 cm^{-1}, which are different from those of $K_4[Fe(CN)_6]\cdot 3H_2O$ (2044 cm^{-1}) and its oxidized form $K_3[Fe(CN)_6]$ (2117 cm^{-1}). These bands of MHCFs-modified samples are assignable to the stretching vibration mode of C≡N in MHCFs.[7] In addition, the peak position of each MHCF(s)/Pt/ZIS was similar to that of MHCF(d)/Pt/ZIS. These results confirm that the surfaces of Pt/ZIS were successfully modified with MHCFs by the stepwise method as well as the direct one.

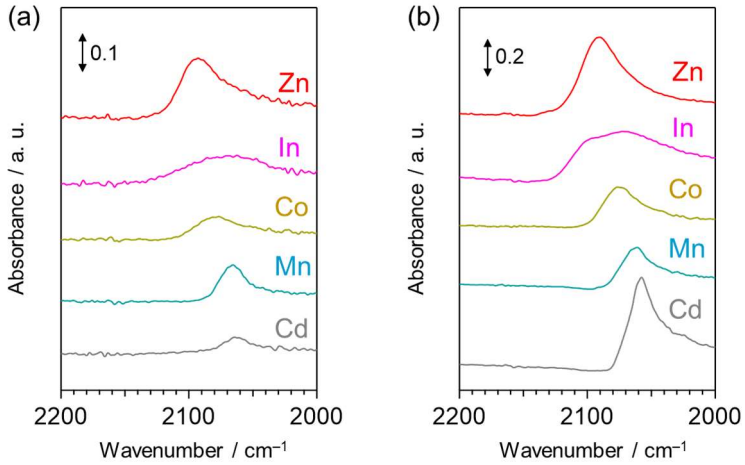

Figure 2-1. IR spectra of Pt/ZIS modified with various MHCFs via (a) the stepwise method and (b) via the direct method.

Figure 2-2 shows SEM images of Pt/ZIS particles modified with MHCFs (M = Zn, Mn, Co or In) via the stepwise or direct method. The particle size of ZnHCF loaded via the stepwise method is smaller than that via the direct one. By contrast, MnHCF, CoHCF and InHCF show similar particle sizes regardless of the deposition method. Figure 2-3 shows TEM images of Pt/ZIS particles loaded with ZnHCF via two different methods (stepwise method or direct one). Obviously, the direct method resulted in aggregated ZnHCF particles on the surface of ZIS with relatively large size (20–50 nm, Figures 2-3a). In stark contrast, the stepwise method brought the surfaces of Pt/ZIS homogeneously coated with thin layers (~20 nm) of MHCF as shown in Figures 2-3b.

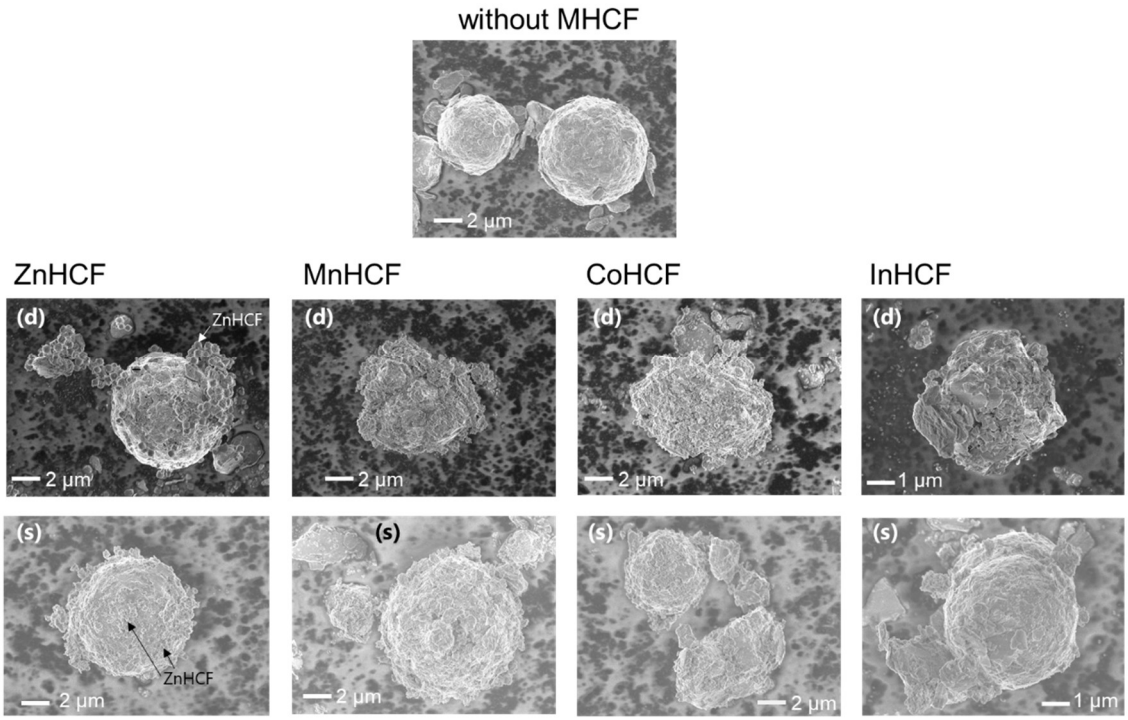

Figure 2-2. SEM images of Pt/$ZnIn_2S_4$ modified with MHCF (M = Zn, Mn, Co or In) via the direct (d) or stepwise method (s) along with that of unmodified Pt/ZIS.

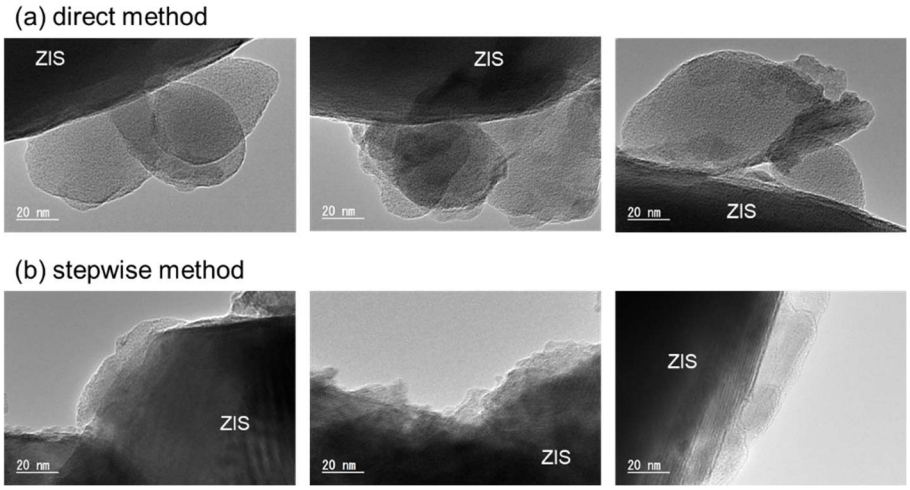

Figure 2–3. TEM images of ZnHCF/Pt/ZIS prepared by two different methods: (a) stepwise or (b) direct.

2.3.2. H_2 evolution over Pt/ZIS modified with MHCFs via the stepwise or direct method

Figure 2-4 shows the initial rates of H_2 evolution on MHCF(s)/Pt/ZIS or MHCF(d)/Pt/ZIS

photocatalysts in the presence of the $[Fe(CN)_6]^{4-}$ electron donor under visible light irradiation. As for ZnHCF, the stepwise method provided the much higher rate of H_2 evolution compared to the direct impregnation. Note that the activities were higher regardless of the loading amount of ZnHCF (Figure 2-5), indicating the effectiveness of the stepwise method. The higher activity can be reasonably explained by the highly dispersed and/or thinner layers of ZnHCFs. Higher dispersion of ZnHCF species on the surface of Pt/ZIS photocatalyst was undoubtedly beneficial for the efficient capture of holes, which generally possess much shorter diffusion length compared with electrons in n-type semiconductor such as ZIS. Simultaneously, the thinner ZnHCF particle layers were probably favorable for the charge transfer from ZIS to ZnHCF surface where the oxidation of $[Fe(CN)_6]^{4-}$ occurs. The stepwise modification was also effective for CdHCF, affording the higher H_2 evolution than the direct method. As shown in Figure 2-6, the thinner layers of CdHCF were also observed, effectively capturing the photogenerated holes in ZIS and oxidizing the $[Fe(CN)_6]^{4-}$ electron donor.

By contrast, the stepwise method for the modification with other MHCFs (M = Mn, Co, or In) induced lower activities than the direct loading method. These finding indicated that the newly-developed stepwise method was effective only for ZnHCF and CdHCF modification. A plausible reason for the lower activity of MHCF(s)/Pt/ZIS will be that the desirable thinner layer of these MHCFs (M = Mn, Co, or In) could not be formed on the surface via the stepwise method, while the origin remains unclear at present.

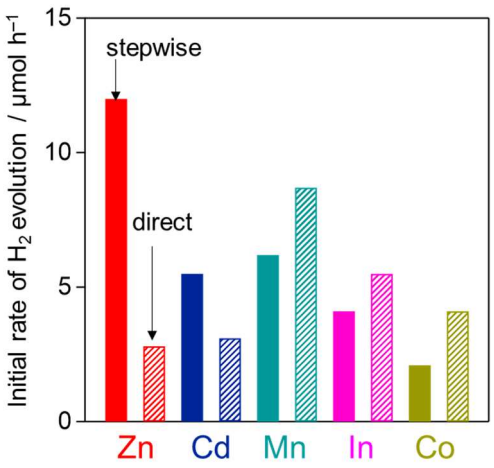

Figure 2-4. Initial rates of H_2 evolution over MHCF/Pt/ZIS (M = Zn, Mn, Co or In) prepared by the different modification methods in 250 mL of BB solution (0.1 M, pH 8.0) containing $K_4[Fe(CN)_6]$ (5 mM) under visible light irradiation.

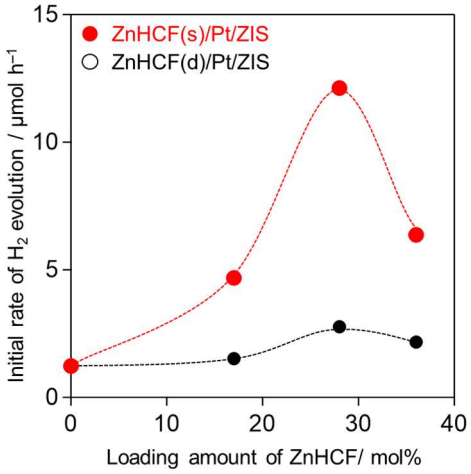

Figure 2-5. Dependence of the loading amount of ZnHCF (mol% as Fe to ZIS) on the initial rates of H_2 evolution over Pt/ZIS in 250 mL of BB aqueous solution (0.1 M, pH 8.0) containing $K_4[Fe(CN)_6]$ (5 mM) under visible-light irradiation.

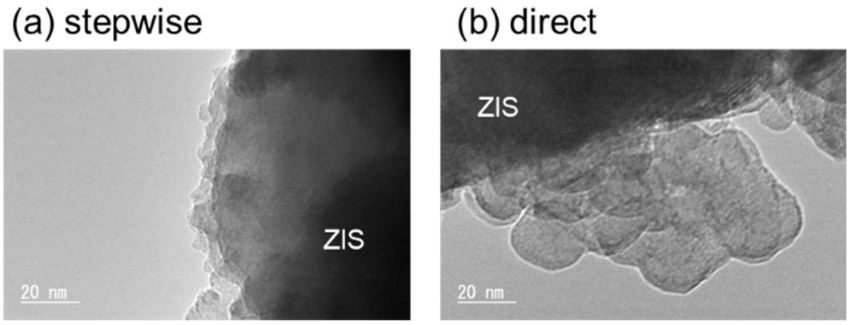

Figure 2-6. TEM images of CdHCF/Pt/ZIS prepared by two different methods: (a) stepwise or (b) direct.

Note that all of the IR bands corresponding to the C≡N stretching vibration in MHCFs were still observed with almost the same absorbances and at the same position even after 5 hours of the reaction, indicating that the stepwise method brought their sufficient durability during the photocatalytic H_2 evolution as well as the direct method.

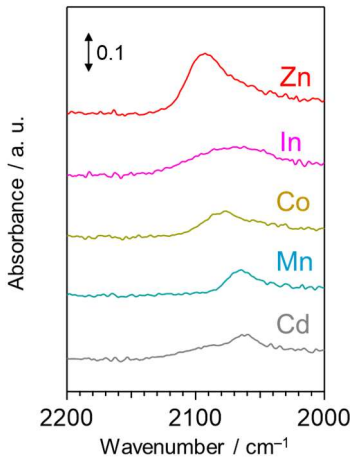

Figure 2-7. ATR-FTIR spectra of MHCF/Pt/ZIS after the reaction.

A longer time irradiation was carried out on the ZnHCF(s)/Pt/ZIS sample, which showed the highest activity, to confirm the occurrence of photocatalytic H_2 evolution by utilizing $[Fe(CN)_6]^{4-}$ as the electron donor. As shown in Figure 2-8, the H_2 evolution continued within 12 h with a slight decrease in the rate probably due to the occurrence of a backward reaction (i.e., competitive reduction of $[Fe(CN)_6]^{3-}$), producing about 70 μmol of H_2 molecules. This amount is larger than that of loaded ZnHCF (estimated to be about 51 μmol). The amount of the oxidative product ($[Fe(CN)_6]^{3-}$) in the solution was determined to be about 72 μmol after the reaction by using the UV-vis spectra of the solution. This value is about half of the value (about 140 μmol) expected from the amount of H_2 evolved by considering the following equations:

(1) $2H^+ + 2e^- \rightarrow H_2$
(2) $[Fe(CN)_6]^{4-} + h^+ \rightarrow [Fe(CN)_6]^{3-}$

The smaller amounts of oxidative products than expected are probably due to the adsorption of $[Fe(CN)_6]^{3-}$ on the surface of photocatalyst particles, as often observed in other half reactions (H_2 or O_2 evolution) using reversible redox mediators such as IO_3^- /I^-.[8] This problem will be solved by combining the ZnHCF(s)/Pt/ZIS photocatalyst with an effective O_2 evolution photocatalyst that can efficiently reduce the $[Fe(CN)_6]^{3-}$ accompanied by oxidation of water to O_2. We can therefore conclude that the zinc hexacyanoferrate, ZnHCF loaded via the stepwise method can function as effective promoters of $[Fe(CN)_6]^{4-}$ oxidation on ZIS photocatalyst, as schematically drawn in Scheme 2-2. The Zn^{2+} species preliminarily loaded on the surface of ZIS react with the

$[Fe(CN)_6]^{4-}$ in the solution, producing the thin layers of ZnHCF species on the surface. The ZnHCF layers effectively capture photogenerated holes in ZIS, resulting that Fe^{II} species in ZnHCF are oxidized to Fe^{III}. Simultaneously, the photoexcited electrons in ZIS are transferred to Pt cocatalysts on which water molecules (or H^+) are reduced to H_2. Finally, the oxidized species (Fe^{III}) in ZnHCF are reduced back to Fe^{II} by accepting electrons from the $[Fe(CN)_6]^{4-}$ electron donor in the solution, producing $[Fe(CN)_6]^{3-}$.

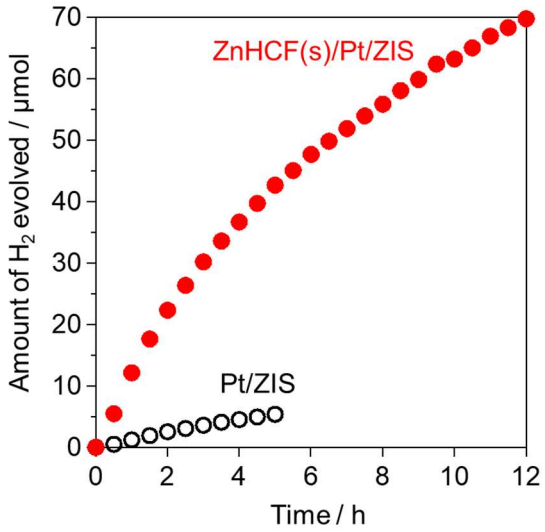

Figure 2-8. Time courses of H_2 evolution over ZnHCF/Pt/ZIS in 250 mL of BB solution (0.1 M, pH 8.0) containing $K_4[Fe(CN)_6]$ (5 mM) under visible light irradiation.

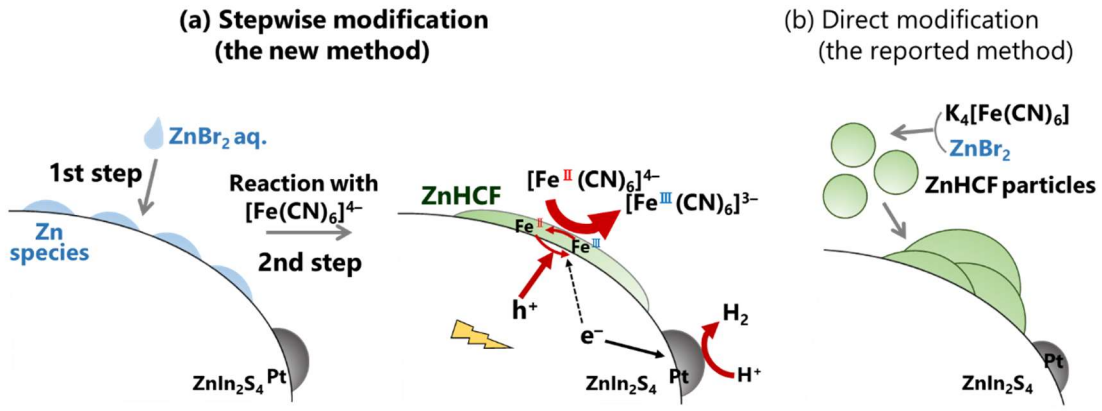

Scheme 2-2. Schematic mechanisms for (a) the surface modification with ZnHCF species via the stepwise method and for the enhanced H_2 evolution on Pt/ZIS photocatalyst in the presence of $[Fe(CN)_6]^{4-}$ electron donor, compared with (b) the modification by the conventional direct method.

2.4. Conclusion

In conclusion, the author successfully developed a stepwise method for the modification with metal hexacyanoferrates (MHCFs). The method was more effective procedure to form thin layer of ZnHCF and CdHCF on the surface of metal sulfide photocatalysts such as $ZnIn_2S_4$ than the conventional loading of preliminary-prepared ZnHCF or CdHCF particles. Thin layers of ZnHCF deposited via stepwise method can captures the photogenerated holes in $ZnIn_2S_4$ and oxidize $[Fe(CN)_6]^{4-}$ electron donor more effectively, thereby inducing the higher H_2 evolution rate on $ZnIn_2S_4$. Although the newly-developed method is less versatile for the formation of thin MHCF layers, the present work serves as an important stepping stone to the more effective loading procedure of MHCFs towards efficient photocatalytic water splitting using visible-light-responsive photocatalysts such as metal sulfides.

References

1. Shirakawa, T.; Higashi, M.; Tomita, O.; Abe, R. *Sustain. Energy Fuels* **2017**, *1*, 1065–1073.
2. Abe, R.; Higashi, M.; Domen, K. *ChemSusChem* **2011**, *4*, 228–237.
3. Gujral, S. S.; Simonov, A. N.; Higashi, M.; Fang, X. Y.; Abe, R.; Spiccia, L. *ACS Catal.* **2016**, *6*, 3404–3417.
4. Li, H.; Lu, D.; Chen, S.; Hisatomi, T.; Vequizo, J. J. M.; Xiao, J.; Wang, Z.; Lin, L.; Xiao, Q.; Sun, Y.; Miseki, Y.; Sayama, K.; Yamakata, A.; Takata, T. and Domen, K. *J. Mater. Chem. A* **2021**, *9*, 13851–13854.
5. Chai, B.; Peng, T.; Zeng, P.; Zhang, X.; Liu, X. J. Phys. Chem. C **2011**, *115*, 6149–6155.
6. Rubin, H. D.; Arent, D. J.; Humphrey, B. D.; Bocarsly, A. B. *J. Electrochem. Soc.* **1987**, *134*, 93–101.
7. De Tacconi, N. R.; Rajeshwar, K.; Lezna, R. O. *Chem. Mater.* **2003**, *15*, 3046–3062.
8. Abe, R. *J. Photochem. Photobiol. C Photochem. Rev.* **2010**, *11*, 179–209.

Chapter 3

Cobalt Hexacyanoferrate as an Effective Cocatalyst Boosting Water Oxidation on Oxynitride TaON Photocatalyst under Visible Light

3.1. Introduction

Artificial photosynthesis including hydrogen production from water and reduction of carbon dioxide (CO_2) by using semiconductor materials has been an active research target due to its considerable potential for solving energy and environmental issues.[1–6] For establishing practical high solar energy conversion efficiencies in artificial photosynthesis systems, effective utilization of photons in visible light region, which accounts for almost half of solar light incident on the Earth's surface, is indispensable, requiring the development of narrow bandgap semiconductors available as photocatalysts or photoelectrodes.[2] In addition, such photocatalyst (or photoelectrode) materials need to efficiently oxidize water to oxygen (O_2) because this reaction ($2H_2O \rightarrow O_2 + 4H^+ + 4e^-$; $E^0 = +1.23$ V vs. standard hydrogen electrode (SHE)) is the key and common process in artificial photosynthesis systems.[1,2,5,6] Loading of appropriate cocatalyst materials that can catalyze water oxidation has proven to be highly effective to improve O_2 evolution on various mixed-anion semiconductors such as oxynitrides (e.g., TaON) under visible light.[7–10] This is probably because the oxidation powers of such mixed-anion compounds are lower compared to those of conventional metal oxides with highly positive valence band maximum at approximately +3.0 V vs. SHE.[11] Such loading of cocatalysts are also effective for maximizing the potential of ultraviolet (UV)-light responsive metal oxides such as Al-doped $SrTiO_3$.[12] Starting from the utilization of conventional electrocatalysts such as RuO_2 and IrO_2,[10,13–17] recent studies on O_2-evolving cocatalysts have focused on the use of inexpensive first-row transition metals (e.g., Co, Fe, Ni), typified by cobalt oxides (CoO_x),[18] (oxy)hydroxides ($CoO_x(OH)_y$),[19,20] phosphates (Co-P_i),[8,21,22] iron oxyhydroxide (FeOOH) and nickel oxyhydroxide (NiOOH).[23] For example, we have demonstrated that the loading of cobalt oxide cocatalysts with adequate approaches drastically improved the O_2 evolution efficiency both on TaON photoanodes and photocatalysts.[8,11,24] However, the number of such active cocatalysts is still limited and the fine tuning of their fundamental properties such as redox potentials is basically difficult, which motivates us to explore different types of materials available as water oxidation cocatalysts.

Herein, we focus on a cobalt-based Prussian blue analogue (PBA) as a cocatalyst for photocatalytic water oxidation. PBA is a coordination polymer in which other metal cations substitute the Fe of Prussian blue ($Fe^{III}_4[Fe^{II}(CN)_3]\cdot nH_2O$), and has a framework structure in which different metal cations are evenly arranged *via* linear cyanide ligands,

as shown in Figure 3-1.[25] It has been demonstrated that the wide variety of compositions and porosity in PBA can be achieved by cation and/or ligand substitutions, thus providing considerable potential for designing various functional materials such as electrodes for secondary ion batteries,[26,27] ion adsorbents,[28] (electro)catalysts,[29–34] and cocatalysts.[35,36] For example, some Co-based PBAs, including cobalt hexacyanoferrate ($K_xCo[Fe(CN)_6]_y{\cdot}nH_2O$) and cobalt hexacyanocobaltate ($K_xCo[Co(CN)_6]_y{\cdot}nH_2O$), have been proven to function as (electro)catalysts for O_2 evolution, in which Co^{II} moieties coordinated to nitrogen atoms in cyanide ligands function as active sites for water oxidation,[29,37] showing comparable activity to that of conventional cobalt oxide (Co_3O_4) in some cases.[37] Moreover, the partial substitution of aliovalent cations or ligands into the structure of Co-based PBAs significantly enhanced (electro)catalytic O_2 evolution activities,[30,31,38] implying their wide and high controllability *via* cation and/or ligand substitutions, as mentioned above. Another attractive feature of Co-based PBA is the stability under a relatively wide range of pH including acidic conditions, as demonstrated by Galán-Mascarós and coworkers.[39] This contrasts with the conventional CoO_x cocatalyst that drastically decreases its activity under pH conditions below 5.[40] In addition, time-resolved spectroscopies analysis on the $BiVO_4$ photoanode modified with Co-based PBA has revealed that largely irreversible hole transfer occurs from $BiVO_4$ to Co-based PBA, retarding charge recombination.[41] We have also demonstrated that $K_2Cd[Fe(CN)_6]$ layers formed on the sulfide photocatalysts (e.g., CdS) efficiently scavenged photogenerated holes and also facilitated the oxidation of $[Fe(CN)_6]^{4-}$ to $[Fe(CN)_6]^{3-}$, providing the stable and efficient H_2 evolution under visible light.[42,43] Despite such attractive features of PBAs as cocatalysts, only few studies have demonstrated the enhanced water oxidation on particulate photocatalysts by PBAs, all of which employed the combination of metal (hydro)oxide photocatalysts (e.g., TiO_2) and strong electron acceptor (i.e., persulfate, $S_2O_8^{2-}$).[44,45]

In the present study, we report that a cobalt hexacyanoferrate $K_xCo[Fe(CN)_6]_y{\cdot}nH_2O$ function as an effective cocatalyst on a visible-light-responsive TaON photocatalyst to improve O_2 evolution in the presence of various electron acceptors such as Ag^+, Fe^{3+} and IO_3^-.

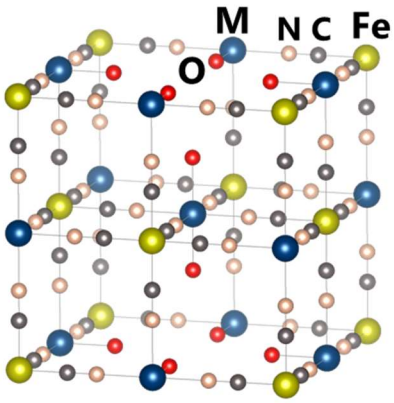

Figure 3-1. Typical structure of metal hexacyanoferrate $A_xM[Fe(CN)_6]_y \cdot nH_2O$ (A: counter cation, M: metal cation, *x*, y, *n*: composition ratio), containing cobalt hexacyanoferrate ($K_xCo[Fe(CN)_6]_y \cdot nH_2O$).

3.2. Experimental

3.2.1. Sample preparation

Particulate TaON sample was synthesized according to a previous report.[46] Briefly, Ta_2O_5 powder (99.99%, Kojundo Chemical Co., Ltd) was placed in a quartz boat and then calcined at 1123 K for 15 h under NH_3 flow (flow rate: 20 mL min^{-1}). Nanoparticles of $K_xCo[Fe(CN)_6]_y \cdot nH_2O$ (denoted as CoHCF hereafter) were prepared by a coprecipitation method by referencing a previous report.[47] 30 mL of aqueous $Co(NO_3)_2$ solution (1 M, prepared from $Co(NO_3)_2 \cdot 6H_2O$, 98.0%; FUJIFILM Wako Pure Chemical Corporation) was added into another 30 mL of aqueous $K_4[Fe(CN)_6]$ solution (0.5 M, prepared from $K_4[Fe(CN)_6] \cdot 3H_2O$, 99.5%; Kishida Chemical Co., Ltd.). The mixture was vigorously stirred for 5 min. The produced precipitate was centrifuged, washed thoroughly three times with Milli-Q water and once with methanol, and finally dried in the oven (308 K) under vacuum for 12 h. As-prepared CoHCF particles were characterized by a series of experiments (Figures 3-2 and 3-3, Table 3-1), confirming the successful preparation of CoHCF nanoparticles with diameters of 20–30 nm basically similar to the previously-reported ones.[39,47] The atomic ratio of CoHCF was determined to be $K_{1.36}Co[Fe(CN)_6]_{0.67} \cdot 4.7H_2O$, which is very close to a previously-reported result.[39]

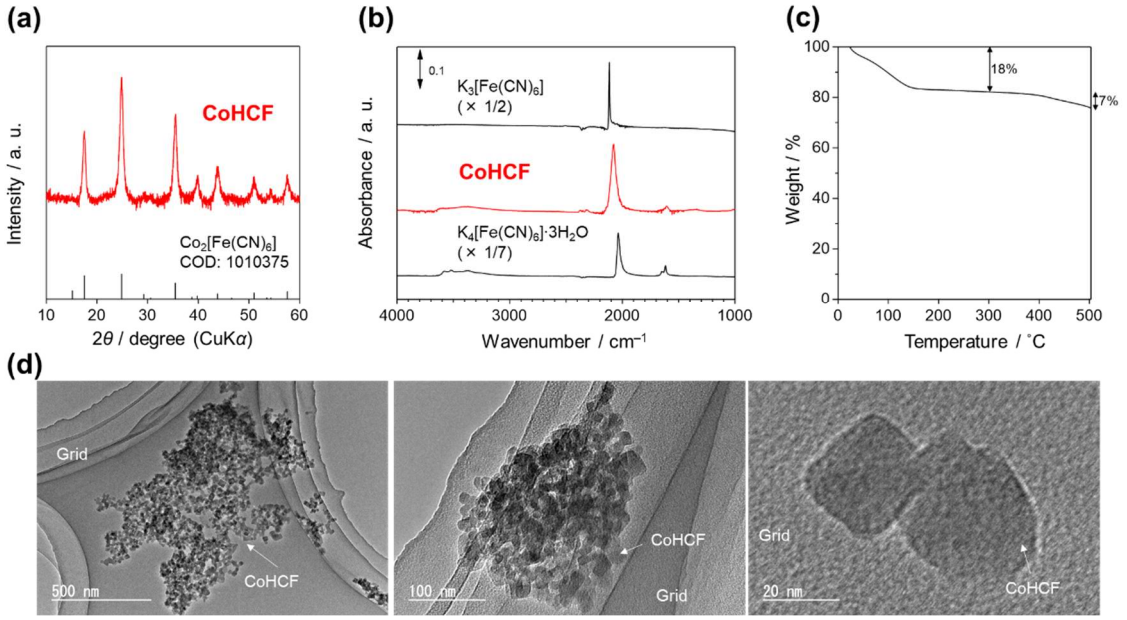

Figure 3-2. Characterization of CoHCF particles: (a) XRD pattern, (b) ATR-FTIR spectra, (c) TG data and (d) TEM images under different magnifications.

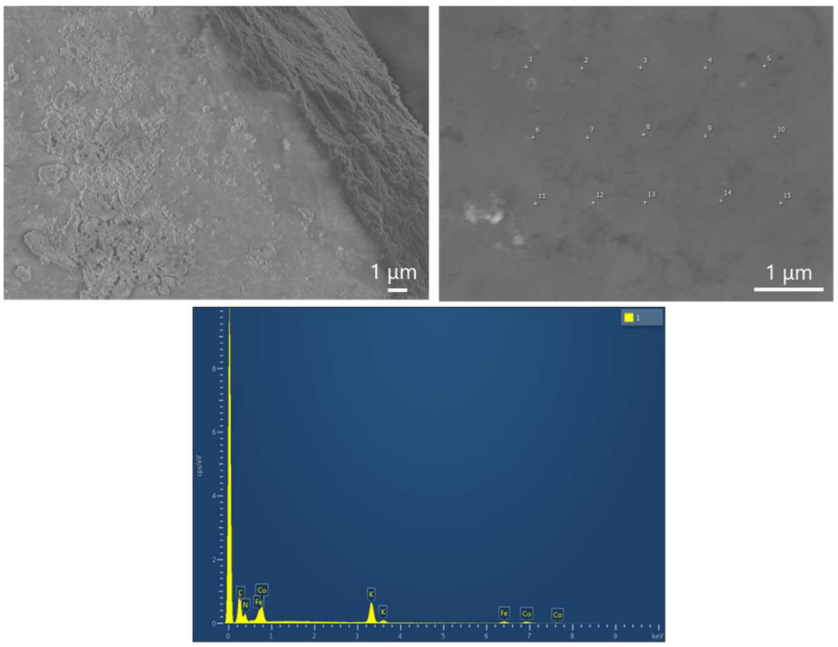

Figure 3-3. SEM images and corresponding EDX spectra of pelletized CoHCF particles.

Table 1. Composition ratio of as-synthesized CoHCF particles estimated by EDX spectra (see Figure 3-3) of pelletized CoHCF particles.

Region	Atomic ratio		
	K	Co	Fe
1	1.18	1	0.65
2	1.44	1	0.69
3	1.25	1	0.69
4	1.00	1	0.61
5	1.19	1	0.69
6	1.38	1	0.69
7	1.47	1	0.73
8	1.31	1	0.69
9	1.29	1	0.59
10	1.64	1	0.71
11	1.25	1	0.63
12	1.38	1	0.69
13	1.29	1	0.65
14	1.57	1	0.71
15	1.79	1	0.64
average	1.36	1	0.67

3.2.2. Surface modification of TaON by CoHCF or Co cation species

Loading of CoHCF nanoparticles onto TaON particles was conducted through an impregnation of CoHCF-dispersed solution. A required amount of CoHCF was dispersed into an appropriate quantity of water containing $K_4[Fe(CN)_6]\cdot 3H_2O$ (12 mol% to CoHCF).[47] Then particulate TaON sample (typically 0.2 g) was added into the dispersed solution (typically 500 μL) and thoroughly agitated; the solution was dried up and then the obtained powder was heated at 373 K for 1 h under Ar flow (20 mL min^{-1}), which will be denoted as CoHCF/TaON hereafter. The amount of CoHCF loaded was fixed to be 0.1 wt% for photocatalysis analysis unless otherwise noted, based on the preliminary optimization of activity for O_2 evolution from $AgNO_3$ solution (10 mM, pH 8) as shown in Figure 3-4. For a comparison, the conventional Co species were loaded onto TaON particles according to our previous report.[11] A particulate TaON (typically 0.2 g) was immersed in a water (typically 500 μL) containing a required amount of $Co(NO_3)_2\cdot 6H_2O$ and agitated well. The suspension was dried up in a hot water bath. Then, the dried sample was heated at 373 K for 1 h in air. Based on the characterizations, the loaded species basically consists of mixture of oxide and hydroxides. Thus, the sample will be denoted

as $CoO_x(OH)_y$/TaON hereafter. The loading amount of $CoO_x(OH)_y$ was set to be 0.1wt% as Co to TaON for photocatalysis analysis unless otherwise noted, according to the optimized results in our previous report.[11]

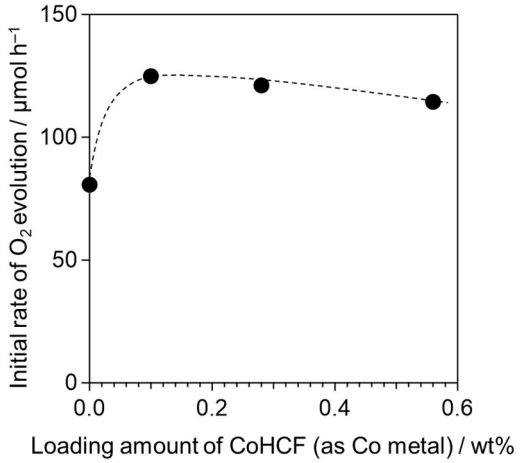

Figure 3-4. Dependence of the loading amount of CoHCF on the initial rate of O_2 evolution over CoHCF/TaON photocatalyst from aqueous $AgNO_3$ solution under visible light irradiation ($\lambda > 400$ nm).

3.2.3. Characterization

The prepared samples and treated samples were characterized by powder X-ray diffraction (XRD; Mini Flex II, Rigaku, X-ray source; Cu Kα) measurement, attenuated total reflectance-Fourier transform infrared spectroscopy (ATR-FTIR, ATR; ATR Pro One, JASCO, FT-IR; FT-4200, JASCO) using a diamond prism. ATR-FTIR spectra were recorded using the absence of the samples in air as the background. Thermogravimetric analysis (TGA) was performed using a STA7200, HITACHI at the heating rate of 10 K min^{-1} up to 773 K in N_2 flow. Scanning electron microscopy (SEM) and energy dispersive X-ray spectroscopy (EDX) were conducted using a NVision 40, Carl Zeiss-SIINT and X-act, Oxford Instruments, respectively. Transmission electron microscopy (TEM) was conducted using a JEM-2100F, JEOL. X-ray photoelectron spectroscopy (XPS) was carried out using a MT-5500, ULVAC-PHI, Inc. (X-ray source: Mg Kα). The binding energies in XP spectra were calibrated with reference to the Au $4f_{7/2}$ peak position (84.0 eV) of the deposited Au metal on the samples.

3.2.4. Stability test of CoHCF and Co cation species

To evaluate the chemical stability of CoHCF nanoparticles, the CoHCF/TaON or $CoO_x(OH)_y$/TaON samples, any of them was suspended in an aqueous solution (pH 8 or pH 3 adjusted by 0.1 M KOH or 1 M HNO_3, respectively), and each solution was stirred for 1 or 5 hours in dark. Subsequently, the samples were centrifuged, washed with Milli-Q water, and then dried in the oven (308 K) under vacuum. The collected particulate samples were characterized by IR spectroscopy, TEM and XP spectroscopy.

3.2.5. Photocatalytic reaction

Photocatalytic activity for water oxidation (i.e., O_2 evolution) was evaluated by using a glass closed gas-circulation system, equipped with an on-line gas chromatograph. A 300 W Xe lamp (LX-300F, Cermax) was used as a light source in combination with a cutoff filter (L-42, Hoya) and a cold mirror (CM-1, Kenko) for visible light irradiation (λ > 400 nm). For O_2 evolution by using Ag^+ as a sacrificial electron acceptor, a photocatalyst sample (0.05 g) was added and suspended in 250 mL of aqueous $AgNO_3$ (99.8%, FUJIFILM Wako Pure Chemical Corporation) solution (10 mM) in a Pyrex glass vessel by means of magnetic stirrer. The pH of the solution was adjusted to 8.0–8.5 or 3 by La_2O_3 (99.99%, FUJIFILM Wako Pure Chemical Corporation) 0.2g or HNO_3 (60~61% (mass/mass), FUJIFILM Wako Pure Chemical Corporation), respectively. Note that La_2O_3, a basic oxide, is well-known as a pH buffer.[46,48,49] The suspension was thoroughly degassed and purged with Ar prior to visible-light irradiation (λ > 400 nm). The evolved gases were analyzed by a gas chromatograph (GC-8A, Shimadzu, TCD detector, Molecular Sieve 5A column, Ar carrier) directly connected to the closed gas-circulation system.

As for photocatalytic O_2 evolution using Fe^{3+}, the CoHCF/TaON sample was further modified with Pt nanoparticles to promote the reduction of Fe^{3+}, as follows. The CoHCF/TaON sample was suspended in an aqueous MeOH solution (80 vol%) containing $H_2PtCl_6 \cdot 6H_2O$ (99.9%, FUJIFILM Wako Pure Chemical Corporation; 0.5 wt% as Pt to CoHCF/TaON) by means of magnetic stirrer. The suspension was thoroughly purged with Ar and then irradiated with visible light using the Xe lamp equipped with the L-42 cutoff filter and the CM-1 under Ar bubbling (50 mL min^{-1}). Hereafter, the obtained sample will be denoted as Pt/CoHCF/TaON. For a comparison, unmodified TaON sample was loaded with Pt alone through the same procedure described above. A suspension of

the prepared photocatalyst powder (0.05 g) in 250 mL of aqueous $FeCl_3$ solution (4 mM) was stirred in a Pyrex glass-made vessel. The photocatalytic activity for O_2 evolution using Fe^{3+} was conducted under same conditions as those to Ag^+ case.

As for photocatalytic O_2 evolution using IO_3^-, $Ru(OH)_xCl_y$ reduction cocatalysts[11] were preloaded on TaON. A particulate TaON (typically 0.2 g) was immersed in a water (typically 500 μL) containing a required amount of $RuCl_3 \cdot nH_2O$ (36–44% as Ru, FUJIFILM Wako Pure Chemical Corporation; 1 wt% as Ru to TaON) and agitated well. The suspension was dried up in a hot water bath. Then, a dried samples were heated at 473 K for 1 h in air. The obtained samples are denoted as Ru/TaON hereafter for simplicity. Ru/TaON samples were subsequently modified with CoHCF *via* the above-described impregnation method.

3.2.6. Photoelectrochemical measurement

Porous photoanodes of TaON were prepared *via* electrophoretic deposition of TaON particles onto Ti substrate (1.5 × 5 cm^2) as previously reported.[8] The coated area was set to be 1.5 × 4 cm^2. The as-prepared electrodes were treated with 50 μL of $TaCl_5$ methanol solution (10 mM) and then dried in air at room temperature. After this process was conducted five times, the electrode was heated in NH_3 flow (10 mL min^{-1}) at 723 K for 30 min. Hereafter, the obtained electrode will be denoted as TaON/Ti. Subsequently, TaON/Ti was modified with CoHCF through a SILAR method by referring a previous report[36] as follows. The TaON/Ti electrodes were dipped in an aqueous $Co(NO_3)_2$ solution (10 min) for 5 min under slow stirring, thoroughly rinsed with Milli-Q water, dipped in an aqueous $K_4[Fe(CN)_6]$ solution (10 mM) for 5 min under stirring and then rinsed with Milli-Q water. This sequence was repeated four times to obtain the CoHCF-modified TaON/Ti electrode, which was denoted as CoHCF/TaON/Ti.

Photoelectrochemical measurements were performed in an aqueous solution of K_2SO_4 (0.1 M, 99.0%; FUJIFILM Wako Pure Chemical Corporation, pH 3, adjusted by H_2SO_4) as an electrolyte under Ar atmosphere using a three-electrode cell. The prepared electrode as the working electrode, Pt coil as the counter electrode, Ag/AgCl as the reference electrode were connected to a potentiostat (VersaSTAT 4, AMETEK), and then linear sweep voltammograms were recorded. The prepared electrodes were irradiated with intermittent visible light using the Xe lamp equipped with a CM-1 cold mirror and an L-42 cutoff filter.

3.3. Results and discussion

3.3.1. Morphology and chemical state of Co species loaded on TaON

Figure 3-5 shows TEM images of particulate TaON samples loaded with CoHCF or $CoO_x(OH)_y$, along with that of unmodified TaON. Some particles with diameters ranging 10–30 nm were found on the surface of CoHCF-modified TaON (Figures 3-5a, b), whereas these particles were not observed on that of unmodified sample (Figure 3-5d). As for the TaON modified with $CoO_x(OH)_y$ (Figure 3-5c), no obvious nanoparticles were found on the TaON surface. However, the presence of Co species (e.g., $Co(OH)_2$) was confirmed by XPS analysis (Figure 3-6a), strongly suggesting that the Co species exist as small clusters of oxides and/or hydroxides. As observed in Figure 3-7, the ATR-FTIR spectrum of the CoHCF/TaON sample exhibited a weak but evident absorption peak assigned to the CN stretching vibration around 2085 cm^{-1}, which is similar to that of as-prepared CoHCF sample, whereas the spectrum of the $CoO_x(OH)_y$/TaON did not exhibit such peak. The XP spectrum (Figure 3-6) of CoHCF/TaON sample exhibited similar peaks of Co2p and Fe2p regions to those observed for as-prepared CoHCF particles. These results indicate the successful modification of the TaON surface by CoHCF nanoparticles without any crucial change in the physicochemical properties of the as-prepared CoHCF.

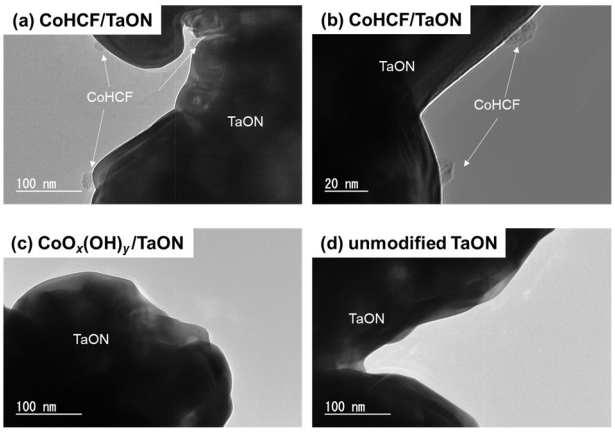

Figure 3-5. TEM images of (a, b) CoHCF-modified, (c) $CoO_x(OH)_y$- modified, and (d) unmodified TaON particles.

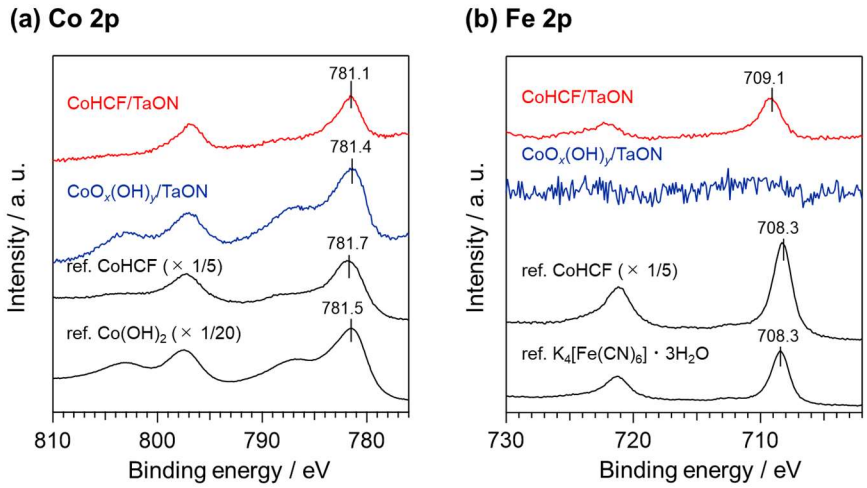

Figure 3-6. XP spectra of CoHCF- or or $CoO_x(OH)_y$-modified TaON particles; (a) Co 2p, (b) Fe 2p region, along with some reference samples.

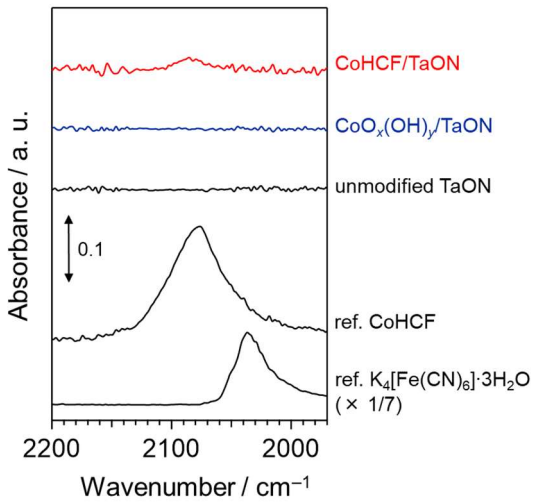

Figure 3-7. ATR-FTIR spectra of CoHCF- or $CoO_x(OH)_y$-modified TaON particles, along with some reference samples.

3.3.2. Photocatalytic O_2 evolution with Ag^+ electron acceptor under basic condition (pH 8)

The effect of CoHCF loading was first evaluated by photocatalytic water oxidation in the presence of Ag^+ as a sacrificial electron acceptor. Herein, the pH value of the solution was set to be 8.0–8.5, in which conventional $CoO_x(OH)_y$ cocatalysts have been proven to improve water oxidation on TaON photocatalysts and photoanodes.[8,11] Note that the pH

of aqueous $AgNO_3$ solution was buffered at 8.0–8.5 by the small amount of La_2O_3 particles added.[46] We preliminary confirmed that CoHCF nanoparticles were stable under this pH condition by the result of simple stirring CoHCF under dark conditions for 5 h (see Figure 3-8).

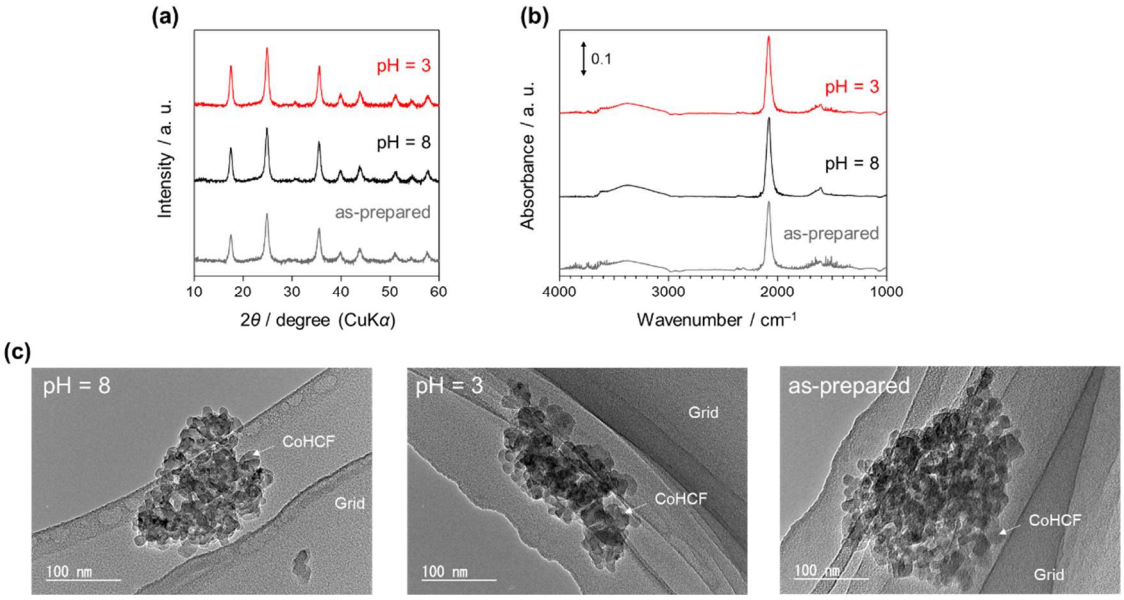

Figure. 3-8. Characterization of CoHCF nanoparticles after stirred in the solution at pH = 8 or 3 (adjusted by KOH or HNO_3, respectively) under the dark condition: (a) XRD patterns, (b) ATR-FTIR spectra and (c) TEM images.

Figure 3-9 shows the time courses of O_2 evolution on TaON samples. As observed, the CoHCF modification enhanced the O_2 evolution on the TaON photocatalyst in a similar manner to the conventional $CoO_x(OH)_y$, whereas the effect of CoHCF was slightly inferior. Note that even the simple addition of Co^{2+} cations (source: $Co(NO_3)\cdot 6H_2O$) into the reaction solution also boosted the O_2 evolution on TaON as seen in Figure 3-9. Adding the same amount of Co^{2+} (as 0.1 wt%) as that for the $CoO_x(OH)_y$/TaON sample provided almost the same activity as $CoO_x(OH)_y$/TaON. Furthermore, even a considerably smaller amount of Co^{2+} (as 0.01 wt%) addition resulted in obvious enhancement (Figure 3-10). The observed enhancement by Co^{2+} addition was probably caused by the spontaneous formation of active species such as $CoO_x(OH)_y$[11,19] on TaON under basic conditions (pH 8). Although the above stability test on CoHCF nanoparticles at pH 8 strongly suggests that CoHCF is stable (i.e., the majority of CoHCF remained), another explanation is that

a small fraction of Co cations dissolved from CoHCF may have formed active species such as $CoO_x(OH)_y$, improving water oxidation.

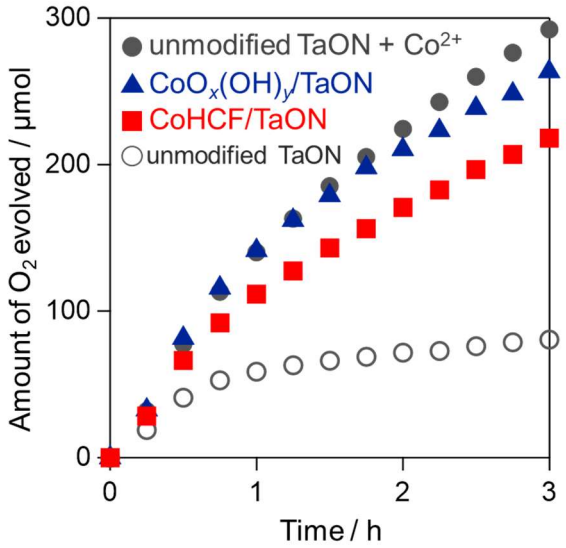

Figure 3-9. Time courses of O_2 evolution over unmodified TaON, CoHCF- or $CoO_x(OH)_y$-modified TaON from aqueous $AgNO_3$ solution (10 mM, 250 mL) at pH 8.0–8.5 under visible light irradiation ($\lambda > 400$ nm)..

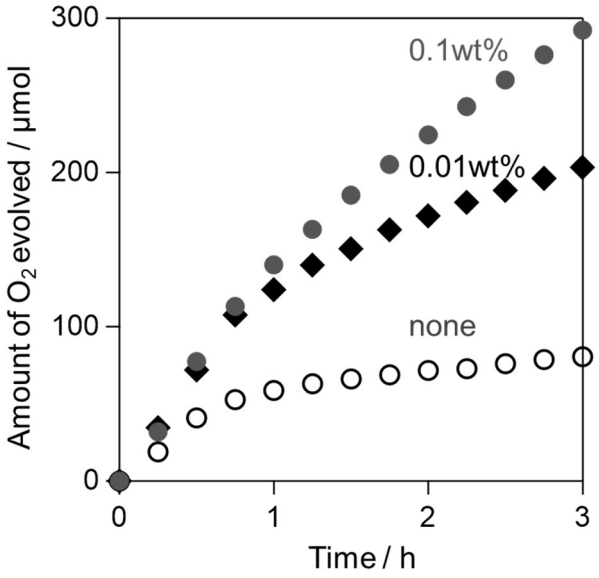

Figure 3-10. Time courses of O_2 evolution over unmodified TaON from aqueous $AgNO_3$ solution (10 mM, 250 mL) at pH 8.0–8.5 in the presence of Co^{2+} (0.01 or 0.1wt% as Co to TaON) under visible light irradiation.

3.3.3. Photocatalytic O_2 evolution with Ag^+ electron acceptor under acidic condition (pH 3)

Given the above results, we evaluated the O_2 evolution under pH conditions at which such simple Co^{2+} addition has a negligibly small effect for enhancing water oxidation on TaON. Figure 3-11 shows the time course of O_2 evolution on TaON samples from acidic (pH 3) aqueous $AgNO_3$ solution under visible light. The simple addition of Co^{2+} cations (as 0.1 wt%) did not significantly enhance the O_2 evolution, indicating that no active species such as hydroxides were formed under this pH condition. In contrast, the loading of CoHCF obviously promoted O_2 evolution on TaON, although the rate of O_2 evolution gradually decreased. Such a decrease in the O_2 evolution rate has been reported for various photocatalysts, not only TaON. This decrease is generally explained by the increased positive charge of photocatalyst surface (e.g., oxides and oxynitrides) due to the decreased pH with the progress of water oxidation ($2H_2O + 4h^+ \rightarrow O_2 + 4H^+$), causing increased electrostatic repulsion between photocatalyst surface and Ag^+.[50] Another possible reason is the light-shielding effect of metallic Ag particles deposited on the TaON surface.[46]

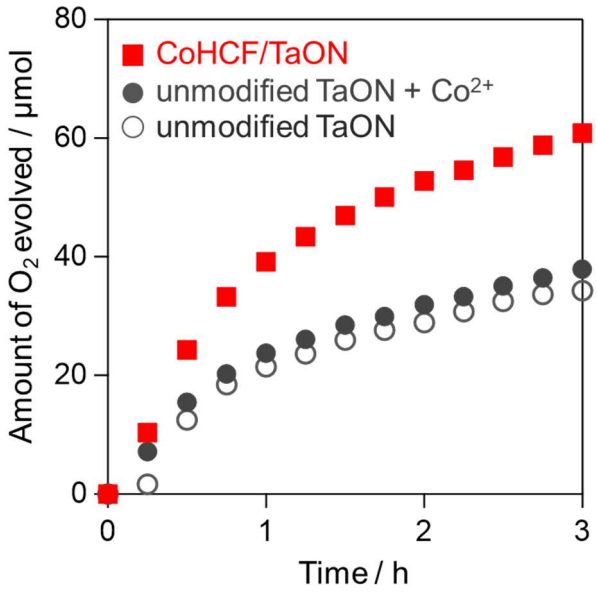

Figure 3-11. Time courses of O_2 evolution over unmodified TaON or CoHCF-modified TaON from aqueous $AgNO_3$ solution (10 mM, 250 mL) at pH 3 under visible light irradiation.

Figure 3-12 shows the photoresponse on TaON photoanodes prepared on Ti metal substrate under visible light. The loading of CoHCF on the TaON significantly enhanced the anodic photocurrent at the entire range of potentials, whereas Co^{2+} addition did not. These findings strongly support the effective function of CoHCF nanoparticles as cocatalysts improving water oxidation by the photogenerated holes on TaON. Although the modification with CoHCFs promoted both the photocatalytic and photochemical water oxidation on TaON, there is still a possibility that the CoHCF species loaded on TaON may not be stable under the acidic condition (pH 3), resulting in a gradual decrease in O_2 evolution rate after 1 h of photoirradiation (Figure 3-11). Unfortunately, the characterization of the photocatalyst samples after the reaction was inhibited by the Ag particles deposited (Figure 3-13).

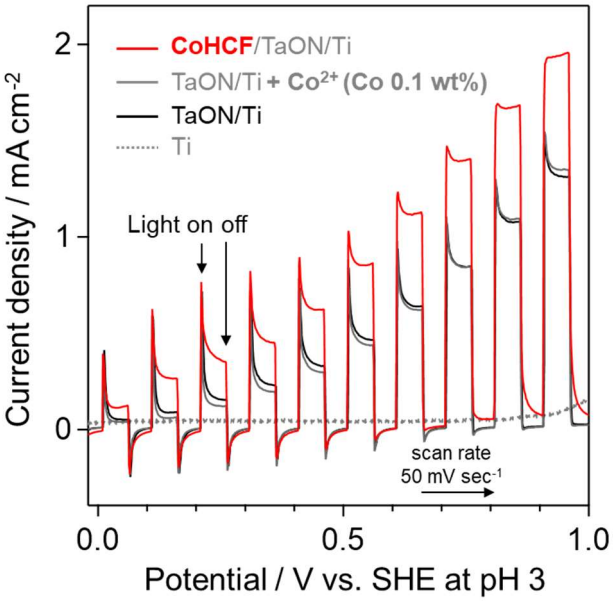

Figure 3-12. Linear sweep voltammograms of CoHCF/TaON/Ti or TaON/Ti electrodes under intermittent irradiation of visible light ($\lambda > 400$ nm). Conditions: counter electrode, Pt coil; reference electrode, Ag/AgCl (3 M KCl); electrolyte, 80 mL of 0.1 M K_2SO_4 aqueous solution (pH 3).

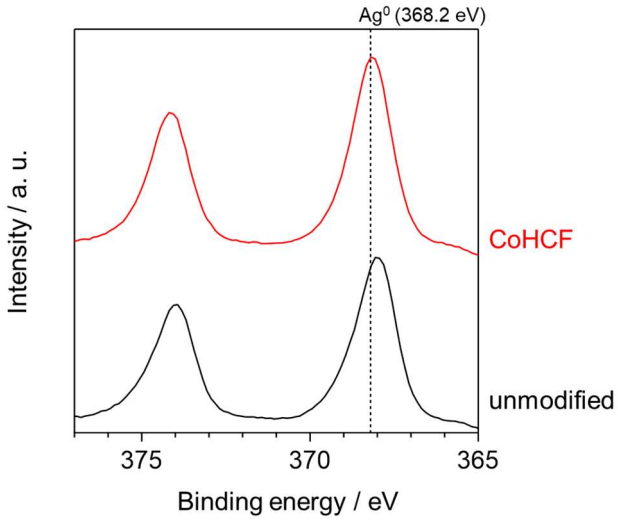

Figure 3-13. XP spectra in Ag 3d region of CoHCF-modified or unmodified TaON after the photocatalytic O_2 evolution from 10 mM $AgNO_3$ aqueous solution (pH 3 adjusted by HNO_3).

To rule out this possibility, the CoHCF/TaON sample was stirred in aqueous HNO_3 solution at pH 3 in the dark for 1 or 5 h (Figures 3-14 and 3-15). Note that the loading amount of CoHCFs was increased to 1wt% to facilitate qualitative and quantitative analysis. As seen in Figure 3-14, no change in the XP and ATR-FTIR spectra was observed even after the acidic treatment for 5 h, indicating the substantial stability of CoHCF at pH 3. Moreover, the CoHCF (0.1wt%)/TaON treated by the acidic treatment for 1 or 5 h showed almost the same activity for O_2 evolution as the untreated one when they were subjected to the reaction at pH 8.0–8.5 (Figure 3-16), strongly supporting the effective function of CoHCF as a cocatalyst. Importantly, the present CoHCF cocatalyst enhanced the O_2 evolution on the TaON photocatalyst even under such acidic conditions where conventional $CoO_x(OH)_y$ cocatalyst cannot because of its dissolution expected by the Pourbaix diagram. The stirring of the $CoO_x(OH)_y$/TaON sample in aqueous HNO_3 solution (pH 3) indeed resulted in the complete dissolution of Co species, as confirmed by XPS (Figures 3-14a, 3-15a); the activity of $CoO_x(OH)_y$/TaON treated with the acid resulted in almost the same as that of the unmodified TaON under the basic condition (pH 8.0–8.5) (see Figure 3-16).

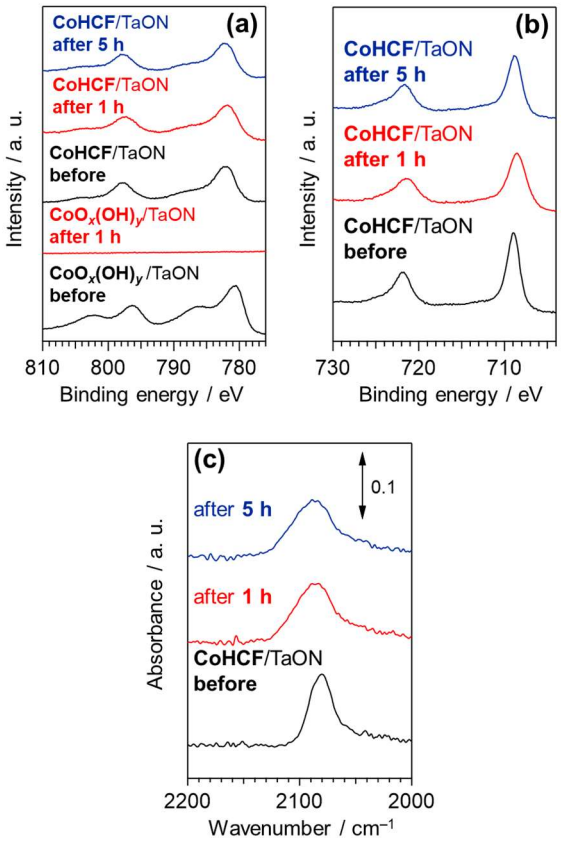

Figure 3-14. Characterization of CoHCF/TaON or $CoO_x(OH)_y$/TaON particles (Co 1wt%) after stirred in aqueous HNO_3 solution (pH 3): (a) XP spectra in Co 2p region, (b) XP spectra in Fe 2p region and (c) ATR-FTIR spectra. Note that the intensity of each XP spectra was calibrated using the peak intensity of Ta $4f_{7/2}$ of pristine $CoO_x(OH)_y$/TaON ('$CoO_x(OH)_y$/TaON before').

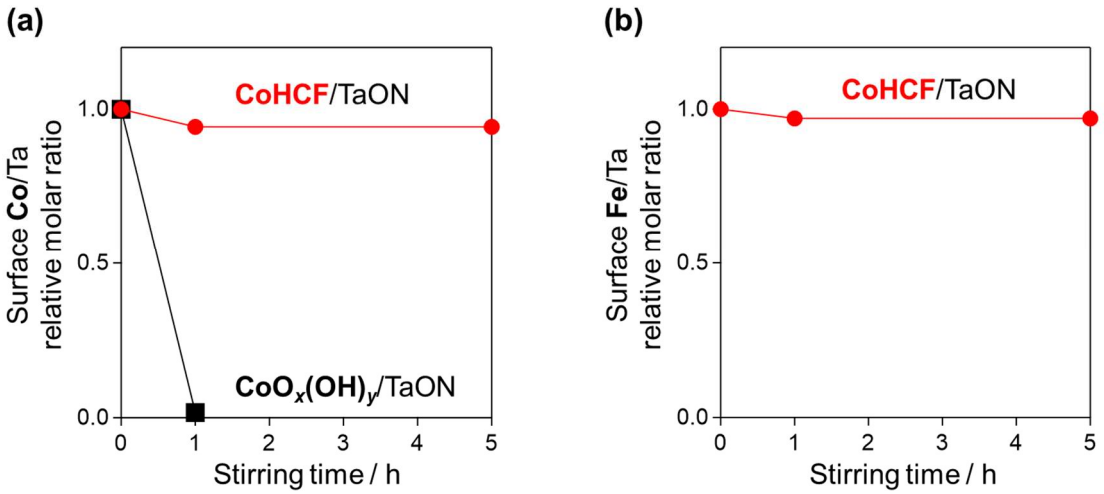

Figure 3-15. (a) Time courses of surface Co/Ta and Fe/Ta molar ratio of CoHCF/TaON particles (Co 1wt%) stirred in HNO_3 aqueous solution (pH 3). Surface Co/Ta and Fe/Ta ratio were determined by the peak areas in XP spectra (Figure 3-14), and normalized by each sample before the acidic treatment.

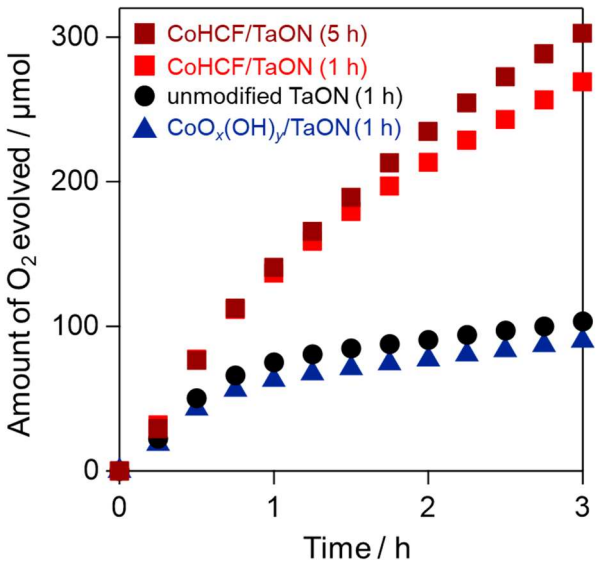

Figure 3-16. Time courses of O_2 evolution over CoHCF- or $CoO_x(OH)_y$-modified or unmodified TaON (Co 0.1 wt%) after stirred in HNO_3 aqueous solution (pH 3). Reaction conditions: photocatalyst mass, 0.05 g; 10 mM $AgNO_3$ aqueous solution (pH 8.0–8.5 adjusted by adding 0.2 g of La_2O_3), 250 mL.

3.3.4. Photocatalytic O_2 evolution with reversible electron acceptors (Fe^{3+} or IO_3^-)

The above findings motivated us to employ the CoHCF/TaON photocatalyst for O_2 evolution with Fe^{3+}/Fe^{2+} redox mediator, which has been demonstrated to effectively employ in Z-scheme water splitting system.[51] This is because the Fe^{3+}/Fe^{2+} couples must be used under highly acidic conditions with pH below 2.5 to avoid precipitation of $Fe(OH)_3$, where conventional $CoO_x(OH)_y$ cannot function. Figure 3-17 shows the time courses of O_2 evolution on various TaON samples in the presence of Fe^{3+} as an electron acceptor. In contrast to the results using the Ag^+ electron acceptor, unmodified TaON showed negligibly low activity, strongly suggesting the necessity of reduction sites for Fe^{3+}. This assumption was justified by the obvious enhancement of O_2 evolution by loading Pt onto TaON as the reduction site. The co-loading of CoHCF and Pt further improved the O_2 evolution because CoHCF functioned as an effective cocatalyst for the oxidation of water to O_2 as described above, thereby resulting in almost continuous O_2 evolution until it reached the stoichiometric amount (250 μmol) expected from the amount of Fe^{3+} added. Both the gradual decrease in the O_2 evolution rate and saturation at nearly 250 μmol can be explained by the deficiency of the Fe^{3+} electron acceptor, but

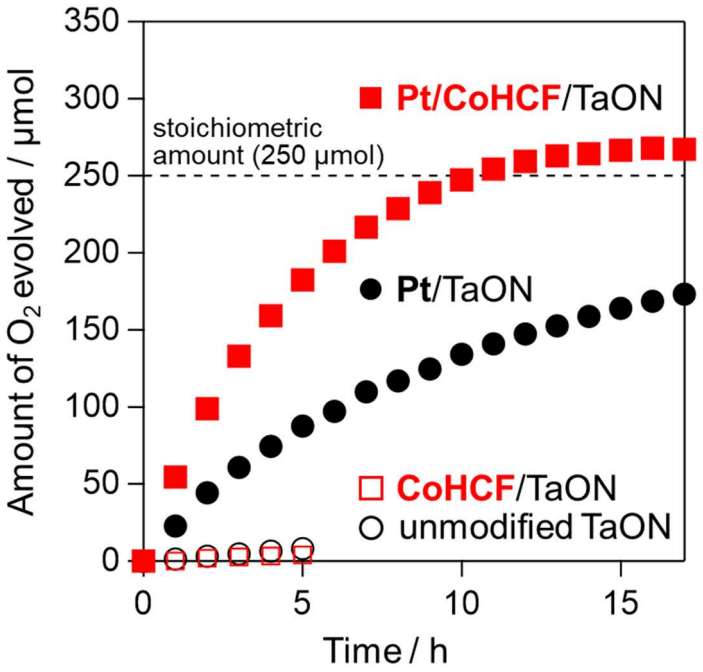

Figure 3-17. Time courses of O_2 evolution over Pt/CoHCF/TaON, Pt/TaON, CoHCF/TaON and TaON photocatalysts from aqueous $FeCl_3$ solution (4 mM, 250 mL) at pH 2.5 under visible light irradiation

the deactivation of photocatalyst and/or CoHCF cannot be completely neglected. As seen in Figure 3-18, both the IR peak and XP spectra derived from CoHCF obviously decreased after the reaction (1st run shown in Figure 3-17), implying deactivation to some extents. Indeed, the rate of O_2 evolution in the 2nd run with the recycled CoHCF/Pt/TaON sample was lower than that in the 1st run. However, the O_2 evolution rate was higher than

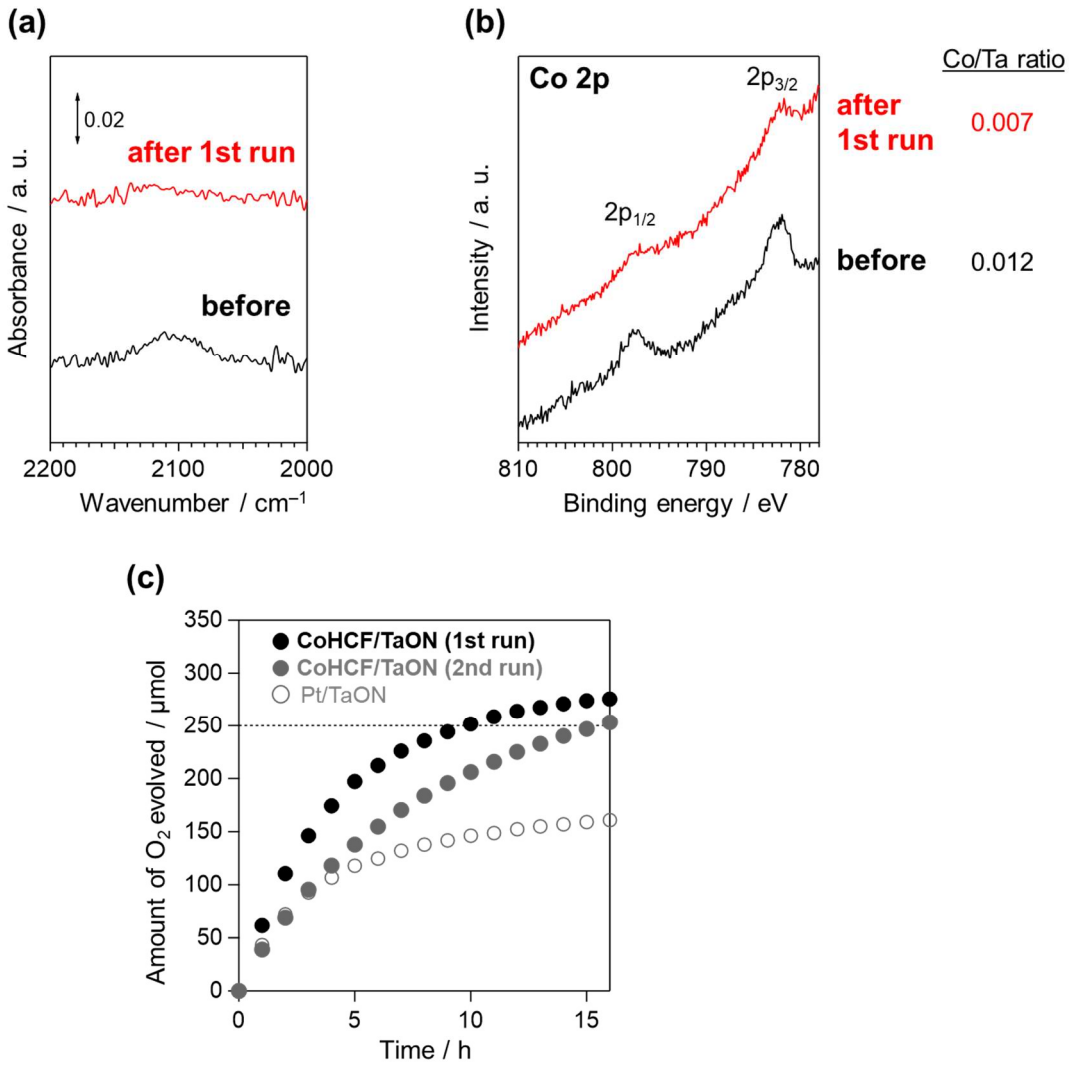

Figure 3-18. Stability of Pt/CoHCF/TaON particles. (a) ATR-FTIR spectra and (b) XP spectra of Pt/CoHCF/TaON particles before and after the photocatalytic O_2 evolution from aqueous $FeCl_3$ solution. (c) Repeatability test of the photocatalytic O_2 evolution over Pt/CoHCF/TaON photocatalysts under visible light irradiation (λ > 400 nm). Conditions: photocatalyst mass, 0.2 g; 4 mM $FeCl_3$ aqueous solution (pH 2.5 adjusted by 1 M HCl), 250 mL.

that of Pt/TaON and it continued up to the expected amount (250 μmol). These results prove that the CoHCF species can also function as effective cocatalysts for O_2 evolution in the Fe^{3+}/Fe^{2+} redox system, not only for the sacrificial O_2 evolution with Ag^+. In addition, CoHCF also promoted the photocatalytic O_2 evolution in the presence of IO_3^- as a reversible electron donor, which is often used as a redox mediator (i.e., IO_3^-/ I^-) in various Z-scheme systems,[52] as shown in Figure 3-19. Note that the Ru-based cocatalyst was co-loaded onto TaON to catalyze the multi-electron reduction of IO_3^-. These findings imply a relatively high availability of CoHCF for improving water oxidation in various systems, although the deactivation observed in the Fe^{3+} electron acceptor system indicated the need for further investigation on CoHCF such as optimization of the modification procedure on photocatalyst surfaces.

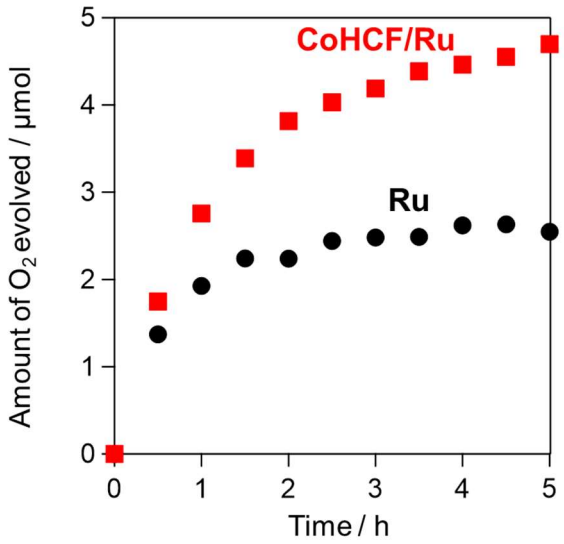

Figure 3-19. Time courses of O_2 evolution over CoHCF/Ru/TaON or Ru/TaON photocatalysts from aqueous KIO_3 solution (1 mM, 250 mL) at pH 3 under visible light irradiation.

3.4. Conclusion

In summary, we revealed that cobalt hexacyanoferrate (CoHCF) nanoparticles functioned as effective cocatalysts on a visible-light-responsive TaON photocatalyst for promoting O_2 evolution, not only showing the activity comparable to that of the conventional $CoO_x(OH)_y$ under basic conditions (pH 8), but also clearly enhancing the activity even under acidic conditions (pH 3), where $CoO_x(OH)_y$ does not work due to chemical

dissolution. Such high durability under acidic conditions of CoHCF made it possible to promote the O_2 evolution on TaON in the presence of the reversible Fe^{3+} electron acceptor, suggesting the possibility of improved efficiency of Z-scheme type water splitting based on Fe^{3+}/Fe^{2+} or other redox couples. However, as indicated by the gradual deactivation of the CoHCF-modified TaON in the Fe^{3+} electron acceptor system, the stability of the present CoHCF cocatalyst on the photocatalyst, as well as its catalytic activity, has much room for improvement. As such hexacyanoferrates have considerable potentials because of their high controllability in various properties *via* cation and/or ligand substitutions, further systematic investigation for understanding the function and elemental steps in hexacyanoferrate materials coupled with photocatalysis may shed light on the development of a new class of highly efficient cocatalysts for photocatalytic water splitting.

References

1. Kudo, A.; Miseki, Y. *Chem. Soc. Rev.* **2009**, *38*, 253–278.
2. Abe, R. J. Photochem. Photobiol. C Photochem. Rev. **2010**, *11*, 179–209.
3. Wang, Q.; Domen, K. Chem. Rev. **2020**, *120*, 919–985.
4. Fabian, D. M.; Hu, S.; Singh, N.; Houle, F. A.; Hisatomi, T.; Domen, K.; Osterloh, F. E.; Ardo, S. *Energy Environ. Sci.* **2015**, *8*, 2825–2850.
5. Yamazaki, Y.; Takeda, H.; Ishitani, O. *J. Photochem. Photobiol. C Photochem. Rev.* **2015**, *25*, 106–137.
6. Dalle, K. E.; Warnan, J.; Leung, J. J.; Reuillard, B.; Karmel, I. S.; Reisner, E. *Chem. Rev.* **2019**, *119*, 2752–2875.
7. Ishikawa, A.; Takata, T.; Kondo, J. N.; Hara, M.; Kobayashi, H.; Domen, K. *J. Am. Chem. Soc.* **2002**, *124*, 13547–13553.
8. Higashi, M.; Domen, K.; Abe, R. *J. Am. Chem. Soc.* **2012**, *134*, 6968–6971.
9. Higashi, M.; Domen, K.; Abe, R. *J. Am. Chem. Soc.* **2013**, *135*, 10238–10241.
10. Maeda, K.; Domen, K. *Angew. Chemie - Int. Ed.* **2012**, *51*, 9865–9869.
11. Iwase, Y.; Tomita, O.; Higashi, M.; Abe, R. *Sustain. Energy Fuels* **2017**, *1*, 748–754.
12. Takata, T.; Jiang, J.; Sakata, Y.; Nakabayashi, M.; Shibata, N.; Nandal, V.; Seki, K.; Hisatomi, T.; Domen, K. *Nature* **2020**, *581*, 411–414.
13. Harriman, A.; Pickering, I. J.; Thomas, J. M.; Christensen, P. A. *J. Chem. Soc. Faraday Trans. 1 Phys. Chem. Condens. Phases* **1988**, *84*, 2795–2806.
14. Darwent, J. R.; Mills, A. *J. Chem. Soc. Faraday Trans. 2 Mol. Chem. Phys.* **1982**, *78*, 359–367.
15. Higashi, M.; Abe, R.; Ishikawa, A.; Takata, T.; Ohtani, B.; Domen, K. *Chem. Lett.* **2008**, *37*, 138–139.
16. Higashi, M.; Domen, K.; Abe, R. *Energy Environ. Sci.* **2011**, *4*, 4138–4147.
17. Maeda, K.; Higashi, M.; Siritanaratkul, B.; Abe, R.; Domen, K. *J. Am. Chem. Soc.* **2011**, *133*, 12334–12337.
18. Zhang, F.; Yamakata, A.; Maeda, K.; Moriya, Y.; Takata, T.; Kubota, J.; Teshima, K.; Oishi, S.; Domen, K. *J. Am. Chem. Soc.* **2012**, *134*, 8348–8351.
19. Zhang, G.; Zang, S.; Wang, X. *ACS Catal.* **2015**, *5*, 941–947.
20. Lyu, H.; Hisatomi, T.; Goto, Y.; Yoshida, M.; Higashi, T.; Katayama, M.; Takata, T.; Minegishi, T.; Nishiyama, H.; Yamada, T.; Sakata, Y.; Asakura, K.; Domen, K. *Chem. Sci.* **2019**, *10*, 3196–3201.

21. Kanan, M. W.; Nocera, D. G. *Science* **2008**, *321*, 1072–1075.
22. Zhong, D. K.; Choi, S.; Gamelin, D. R. *J. Am. Chem. Soc.* **2011**, *133*, 18370–18377.
23. Tae Woo Kim and Kyoung-Shin Choi. *Science* **2014**, *343*, 990–994.
24. Gujral, S. S.; Simonov, A. N.; Higashi, M.; Fang, X. Y.; Abe, R.; Spiccia, L. *ACS Catal.* **2016**, *6*, 3404–3417.
25. De Tacconi, N. R.; Rajeshwar, K.; Lezna, R. O. *Chem. Mater.* **2003**, *15*, 3046–3062.
26. Lu, Y.; Wang, L.; Cheng, J.; Goodenough, J. B. *Chem. Commun.* **2012**, *48*, 6544–6546.
27. Lee, H. W.; Wang, R. Y.; Pasta, M.; Lee, S. W.; Liu, N.; Cui, Y. *Nat. Commun.* **2014**, *5*, 5280.
28. Asai, M.; Takahashi, A.; Tajima, K.; Tanaka, H.; Ishizaki, M.; Kurihara, M.; Kawamoto, T. *RSC Adv.* **2018**, *8*, 37356–37364.
29. Goberna-Ferrón, S.; Hernández, W. Y.; Rodríguez-García, B.; Galán-Mascarós, J. R. *ACS Catal.* **2014**, *4*, 1637–1641.
30. Yamada, Y.; Oyama, K.; Gates, R.; Fukuzumi, S. *Angew. Chemie - Int. Ed.* **2015**, *54*, 5613–5617.
31. Aksoy, M.; Nune, S. V. K.; Karadas, F. *Inorg. Chem.* **2016**, *55*, 4301–4307.
32. Isaka, Y.; Oyama, K.; Yamada, Y.; Suenobu, T.; Fukuzumi, S. *Catal. Sci. Technol.* **2016**, *6*, 681–684.
33. Tabe, H.; Terashima, C.; Yamada, Y. *Catal. Sci. Technol.* **2018**, *8*, 4747–4756.
34. Yamane, M.; Tabe, H.; Kawakami, M.; Tanaka, H.; Kawamoto, T.; Yamada, Y. *Inorg. Chem.* **2020**, *59*, 16000–16009.
35. Shaddad, M. N.; Arunachalam, P.; Labis, J.; Hezam, M.; Al-Mayouf, A. M. *Appl. Catal. B Environ.* **2019**, *244*, 863–870.
36. Hegner, F.; Herraiz-Cardona, I.; Cardenas-Morcoso, D.; Lopez, N.; Galán-Mascarós, J. R.; Gimenez, S. *ACS Appl. Mater. Interfaces* **2017**, *9*, 37671–37681.
37. Pintado, S.; Goberna-Ferrón, S.; Escudero-Adán, E. C.; Galán-Mascarós, J. R. *J. Am. Chem. Soc.* **2013**, *135*, 13270–13273.
38. M. Pires, B.; Hegner, F. S.; Bonacin, J. A.; Galán-Mascarós, J. R. *ACS Appl. Energy Mater.* **2020**, *3*, 8448–8456.
39. Han, L.; Tang, P.; Reyes-Carmona, Á.; Rodríguez-García, B.; Torréns, M.; Morante, J. R.; Arbiol, J.; Galán-Mascarós, J. R. *J. Am. Chem. Soc.* **2016**, *138*, 16037–16045.
40. Higashi, M.; Kato, Y.; Iwase, Y.; Tomita, O.; Abe, R. *J. Photochem. Photobiol. A Chem.* **2021**, *419*, 113463.
41. Moss, B.; Hegner, F. S.; Corby, S.; Selim, S.; Francàs, L.; López, N.; Giménez, S.; Galán-

Mascarós, J. R.; Durrant, J. R. *ACS Energy Lett.* **2019**, *4*, 337–342.

42. Shirakawa, T.; Higashi, M.; Tomita, O.; Abe, R. *Sustain. Energy Fuels* **2017**, *1*, 1065–1073.
43. Matsuoka, H.; Higashi, M.; Nakada, A.; Tomita, O.; Abe, R. *Chem. Lett.* **2018**, *47*, 941–944.
44. Akbari, S. S.; Karadas, F. *ChemSusChem* **2020**, *14*, 679–685.
45. Gundogdu, G.; Ulusoy Ghobadi, T. G.; Sadigh Akbari, S.; Ozbay, E.; Karadas, F. *Chem. Commun.* **2021**, *57*, 508–511.
46. Hitoki, G.; Takata, T.; Kondo, J. N.; Hara, M.; Kobayashi, H.; Domen, K. *Chem. Commun.* **2002**, *2*, 1698–1699.
47. Gotoh, A.; Uchida, H.; Ishizaki, M.; Satoh, T.; Kaga, S.; Okamoto, S.; Ohta, M.; Sakamoto, M.; Kawamoto, T.; Tanaka, H.; Tokumoto, M.; Hara, S.; Shiozaki, H.; Yamada, M.; Miyake, M.; Kurihara, M. *Nanotechnology* **2007**, *18*, 1–6.
48. Kasahara, A.; Nukumizu, K.; Takata, T.; Kondo, J. N.; Hara, M.; Kobayashi, H.; Domen, K. *J. Phys. Chem. B* **2003**, *107*, 791–797.
49. Wang, Q.; Nakabayashi, M.; Hisatomi, T.; Sun, S.; Akiyama, S.; Wang, Z.; Pan, Z.; Xiao, X.; Watanabe, T.; Yamada, T.; Shibata, N.; Takata, T.; Domen, K. *Nat. Mater.* **2019**, *18*, 827–832.
50. Ohtani, B.; Okugawa, Y.; Nishimoto, S. I.; Kagiya, T. *J. Phys. Chem.* **1987**, *91*, 3550–3555.
51. Kato, H.; Hori, M.; Konta, R.; Shimodaira, Y.; Kudo, A. *Chem. Lett.* **2004**, *33*, 1348–1349.
52. Wang, Y.; Suzuki, H.; Xie, J.; Tomita, O.; Martin, D. J.; Higashi, M.; Kong, D.; Abe, R.; Tang, J. *Chem. Rev.* **2018**, *118*, 5201–5241.

Chapter 4

Indium Hexacyanoferrate Overcomes a Limitation in Z-scheme Water Splitting with an Fe^{3+}/Fe^{2+} Redox Mediator: Activating Photocatalysts by Boosting Redox Mediator Oxidation

4.1. Introduction

Water splitting using particulate photocatalysts has been extensively studied because of the significant potential of this technology for large-scale clean hydrogen (H_2) production.[1–5] Although the utilization of a wide portion of the visible spectrum is indispensable for achieving practically sufficient solar-to-hydrogen (STH) conversion efficiencies, there are few examples of visible-light-driven water splitting systems using a single photocatalyst.[6–9] This is primarily due to the strict requirements for the properties of semiconductor materials, including a band gap that is narrower than 3.1 eV, band levels suitable for both water reduction and oxidation, and high stability. Z-scheme-type water splitting, in which two separate and distinct photocatalysts are applied for H_2 and O_2 evolution, respectively, has been demonstrated to enable the use of various visible-light-responsive photocatalysts that do not meet the above criteria.[10,11]

Because a redox couple, such as IO_3^-/I^-, Fe^{3+}/Fe^{2+}, plays a key role in electron transfer between the two photocatalysts in the majority of Z-scheme systems, designing efficient forward electron migration through rational control over the redox reactions is crucial to achieve highly efficient water splitting. However, there are only a few examples of Z-scheme systems in which surface redox reactions are intentionally controlled.[12,13] The majority of previous Z-scheme water splitting studies using such redox couples have relied on the specific affinity between the photocatalyst surface and each redox species, such as the selective adsorption of either redox couple onto the photocatalyst surface. For example, it has been demonstrated that IO_3^- preferentially adsorbs onto the surfaces of rutile TiO_2 or WO_3 particles, whereas I^- cannot, allowing these photocatalysts to oxidize water even in the presence of considerably high concentrations of I^-.[2] Actually, many photocatalysts exhibit negligible H_2 or O_2 evolution, despite the suitability of their band levels for reactions with redox mediators. This problem is typified by the narrow selection of H_2 evolution photocatalysts applicable to the system using the Fe^{3+}/Fe^{2+} redox couple.[11,14] Because the Fe^{3+}/Fe^{2+} redox couple offers several practical advantages, including a simple one-electron transfer process and visible-light transparency under typical operating conditions, its application in Z-scheme water splitting systems has been extensively studied.[10,11,14] However, the only sufficiently effective H_2 evolution photocatalyst employing an Fe^{2+} electron donor is Rh-doped $SrTiO_3$ (STO:Rh), originally developed by Kudo and coworkers.[15] In contrast, the availability of efficient O_2 evolution photocatalysts is considerably greater (e.g., WO_3,[14] $BiVO_4$,[14] H_2WO_4,[16,17] TiO_2:Ta,N,[18] and Bi_4NbO_8Cl[19]). Notably, undoped STO exhibits low H_2 evolution activity in the presence of an Fe^{2+} electron donor under UV light irradiation.[14] This implies that Rh doping of STO is

essential for efficient H_2 evolution when an Fe^{2+} electron donor is used. The Rh^{4+} species generated from the electron photoexcitation of the Rh^{3+} donor level to the conduction band of STO presumably serve as specific sites for Fe^{2+} oxidation. Thus, to widen the choice of H_2 evolution photocatalysts applicable in Z-scheme systems involving Fe^{3+}/Fe^{2+} redox couples, Fe^{2+} oxidation sites should be rationally designed on the photocatalyst surface via surface modification such as cocatalyst loading. However, such cocatalysts have not yet been reported.

Here, we focused on Prussian blue analogues containing metal hexacyanoferrates (MHCFs) as new cocatalysts for Fe^{2+} oxidation. MHCFs are a class of three-dimensional coordination polymers with a general formula of $A_hM_k[Fe(CN)_6]_l \cdot mH_2O$ (Figure 4-1; *h, k, l, m*: composition ratios; A: alkali metal cation; M: (transition) metal cation), where M and Fe ions are bridged by cyanide (CN) ligands.[20] The MHCF family has attracted considerable attention as functional materials applicable in various technologies, such as in electrochromic devices,[21,22] adsorbents,[23,24] electrodes for secondary batteries[25,26], and (electro)catalysis.[27–29] Recently, we have demonstrated that the surface modification of metal sulfide or selenide photocatalysts with MHCF (A = K^+, M = Cd^{II}, Zn^{II}, or In^{III}) promoted photocatalytic H_2 evolution in the presence of $[Fe(CN)_6]^{4-}$ as an electron donor by promoting $[Fe(CN)_6]^{4-}$ oxidation via the reversible Fe^{III}/Fe^{II} redox cycles in MHCFs.[30,31] These findings motivated us to employ MHCFs as promoters for Fe^{2+} oxidation, and thereby activate the photocatalyst materials that have so far been regarded as inactive for H_2 evolution from aqueous Fe^{2+} solutions.

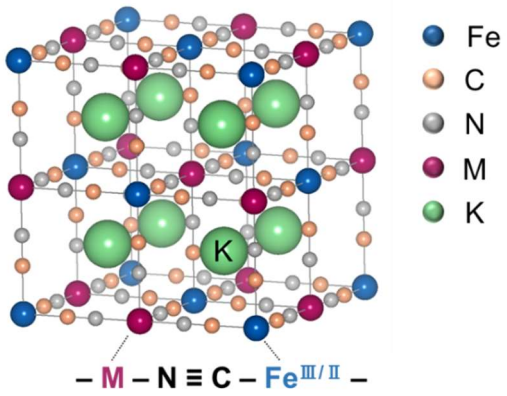

Figure 4-1. Typical structure of metal hexacyanoferrate, $K_2M[Fe(CN)_6]$.

In this study, we modified the surface of a TaON-based photocatalyst reported to show trivial photocatalytic H_2 evolution activity in aqueous solutions containing Fe^{2+} electron donors even after Pt deposition,[32] with indium hexacyanoferrate (InHCF) nanoparticles to endow it with H_2 evolution capabilities. We demonstrated that the co-loading of InHCF and an appropriate H_2 evolution cocatalyst onto TaON considerably enhanced the photocatalytic H_2 evolution rate, thereby realizing an efficient Fe^{3+}/Fe^{2+}-based Z-scheme water splitting system employing an H_2 evolution photocatalyst other than conventional STO:Rh.

4.2. EXPERIMENTAL

4.2.1. Sample preparation

ZrO_2-modified TaON particles as the model H_2 evolution photocatalysts were synthesized by a previously reported method with a modification.[33] First, $ZrO(NO_3)_2 \cdot 2H_2O$ (99.0%; Kanto Chemical Co., Inc.) and Ta_2O_5 (99.9%; Kojundo Chemical Laboratory Co., Ltd.) powders were mixed with a small amount of methanol (MeOH, 99.8%; FUJIFILM Wako Pure Chemical Corporation). The molar ratio of Zr to Ta is set to be 0.1. After dried in an oven at 343 K for 1 h, the resulting powder was heated in air at 1073 K for 2 h using an Al_2O_3 crucible. And then, the as-prepared ZrO_2/Ta_2O_5 powder was calcined at 1123 K for 15 h under NH_3 flow (12 mL min^{-1}). As-prepared ZrO_2-modified TaON particles were confirmed to be similar to the previous-reported one[33] (Figure 4-2). ZrO_2-modified TaON will be denoted as TaON for simplicity hereafter.

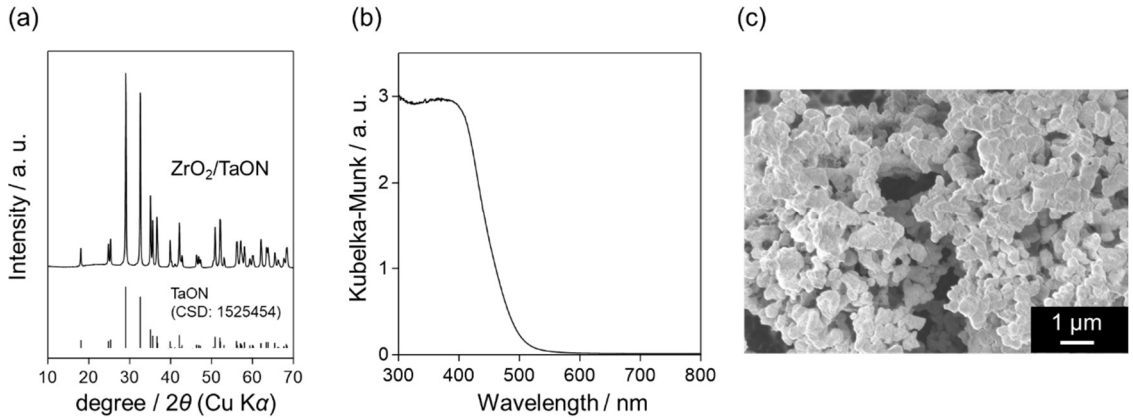

Figure 4-2. (a) XRD patterns, (b) Diffuse reflectance spectra and (c) SEM images of as-prepared ZrO_2/TaON particles.

$BaTaO_2N$,[34,35] Ta_3N_5,[36] $Sm_2Ti_2S_2O_5$[37] were synthesized as an another H_2 evolution photocatalyst, according to the literature. $BiVO_4$[38] and surface-treated WO_3[12,39] as O_2 evolution photocatalysts for Z-scheme water splitting were prepared according to the previous reports.

Indium hexacyanoferrate (denoted as InHCF, composition: $KIn[Fe(CN)_6]$) nanoparticles were prepared by a coprecipitation method by referencing the previous report.[40] An aqueous solution 30 mL of $InCl_3 \cdot 4H_2O$ (30 mmol, 99.95%; Kanto Chemical Co., Inc.) was added to an aqueous solution 60 mL of $K_4[Fe(CN)_6] \cdot 3H_2O$ (30 mmol, 99.5%; Kishida Chemical Co., Ltd.). The reaction mixture was vigorously stirred for 5 min by using a magnetic stirrer. The resulting precipitate was centrifuged (3700 rpm), washed with water three times and MeOH once, and dried in an oven at 308 K under vacuum. The oxidized form of InHCF (denoted as InHCF-ox) was also synthesized by the above method, except for the use of $K_3[Fe(CN)_6]$ (30 mmol, 99.0%; FUJIFILM Wako Pure Chemical Corporation) instead of $K_4[Fe(CN)_6] \cdot 3H_2O$. Zinc hexacyanoferrate ($K_2Zn_3[Fe(CN)_6]$, ZnHCF) and iron(II) hexacyanoferrate ($K_2Fe(II)[Fe(CN)_6]$, FeHCF) were also synthesized by the above method for InHCF preparation, except for the use of $ZnBr_2$ (45 mmol, 99.9%; FUJIFILM Wako Pure Chemical Corporation) and $FeCl_2 \cdot 4H_2O$ (30 mmol, 99.0%; FUJIFILM Wako Pure Chemical Corporation), respectively, instead of $InCl_3 \cdot 4H_2O$.

4.2.2. Surface modification

Any one of Pt, Rh or $Rh_xCr_{2-x}O_3$ species as H_2 evolution cocatalysts was loaded on TaON particles, as follows. Pt particles were loaded onto TaON by an impregnation method. TaON powder was immersed in an aqueous solution containing the required amount of $H_2PtCl_6 \cdot 6H_2O$ (99.9%; FUJIFILM Wako Pure Chemical Corporation) and placed into a hot water bath. After the solution was evaporated, the resulting powder was calcined at 473 K for 1 h under H_2 flow (20 mL min^{-1}). Rh and $Rh_xCr_{2-x}O_3$ particles were loaded on TaON by a photodeposition method. TaON powder was immersed in an aqueous MeOH solution (20 vol%) containing the required amount of $Na_3RhCl_6 \cdot nH_2O$ (>80.0%; Kanto Chemical Co., Inc.) or both $Na_3RhCl_6 \cdot nH_2O$ and K_2CrO_4 (99.0%; FUJIFILM Wako Pure Chemical Corporation) for Rh and $Rh_xCr_{2-x}O_3$, respectively. The suspension was purged by Ar gas to remove dissolved air and then exposed to visible light (λ > 400 nm) through a 300 W Xe lamp (LX-300F, Cermax) equipped with a CM-1 cold mirror and a cutoff filter (HOYA, L42) under Ar bubbling (50 mL min^{-1}). The Rh- or $Rh_xCr_{2-x}O_3$-depositied samples were collected by filtration and then dried in an oven at 308 K under vacuum. Each deposited reduction cocatalyst was determined by X-ray

photoelectron spectroscopy and X-ray absorption fine structure spectroscopy (Figures 4-3, 4-4). Unless otherwise noted, the amount of added Pt or Rh precursor was set to be 1wt% as each metal with respect to TaON and that of added Cr was set to be 1.5wt%, based on the results in Table 4-1.

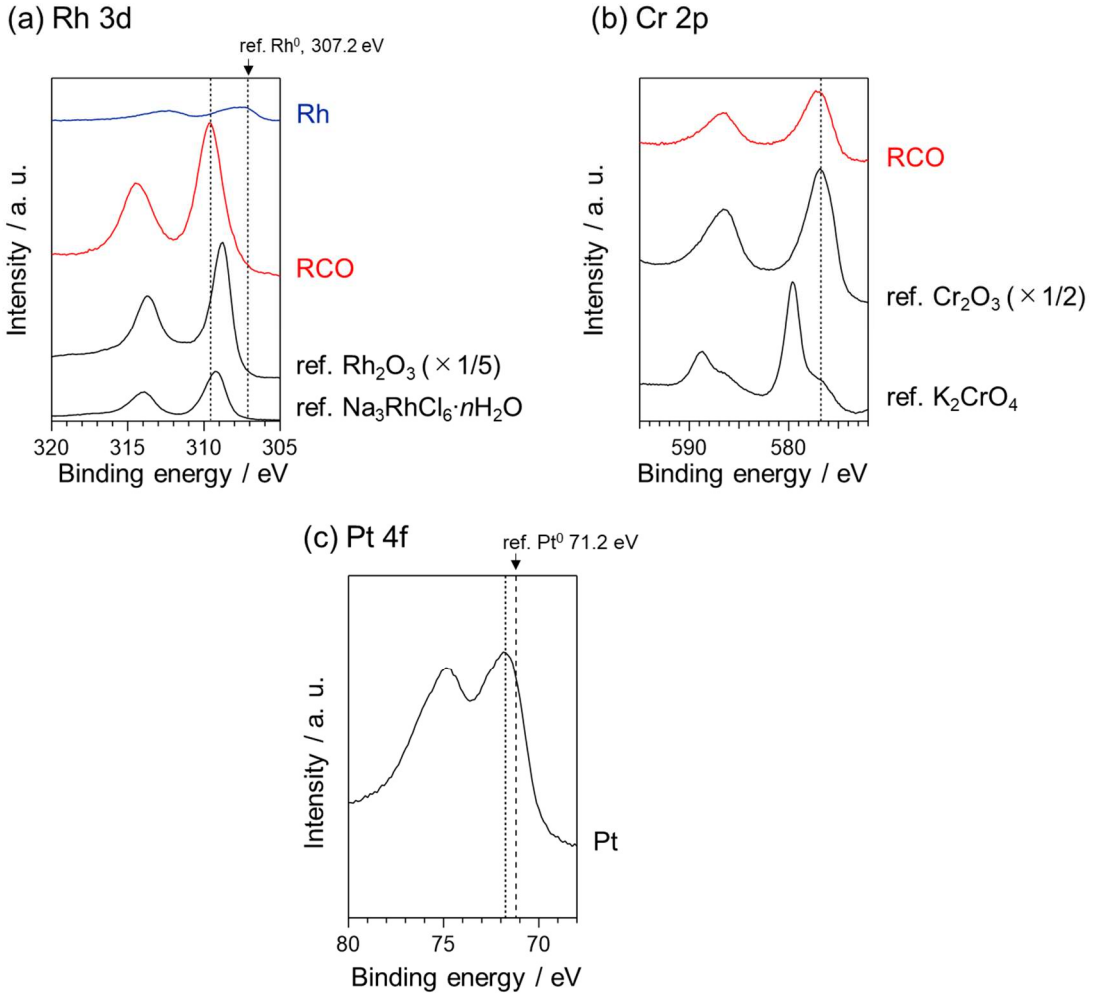

Figure 4-3. XP spectra of TaON particles loaded with various reduction cocatalysts; (a) Rh 3d, (b) Cr 2p, (c) Pt 4f region, along with some references.

The peak positions of ref. Rh^0 and ref. Pt^0 were referred to *Handbook of X-ray Photoelectron Spectroscopy: A Reference Book of Standard Spectra for Identification and Interpretation of XPS data; Physical Electronics Division, Perkin-Elmer Corporation, 1992.*

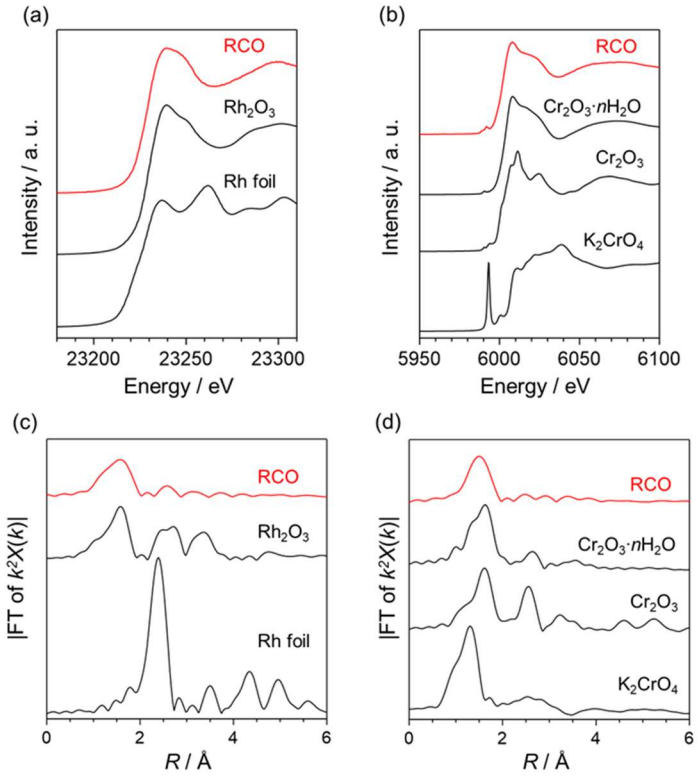

Figure 4-4. (a) Rh-K and (b) Cr-K edge XANES spectra, and Fourier transforms (FT) of the k^2-weighted (c) Rh-K and (d) Cr-K edge EXAFS spectra of RCO/TaON, along with those of some reference samples. Note that Cr_2O_3 nH_2O was prepared by hydrolysis of $Cr(NO_3)_3$ $9H_2O$.

Table 4-1. Initial rates of H_2 evolution over TaON modified with various amount of RCO and InHCF under visible light irradiation.

Rh added / wt%	Cr added / wt%	InHCF[a] / mol%	Activity / μmol h^{-1}
0.50	0.75	10	51.9
1.00	1.50	10	123
1.50	2.25	10	84.0
1.00	0.50	10	77.8
1.00	3.00	10	93.2
1.00	1.50	5	63.9
1.00	1.50	15	103

Reaction conditions: photocatalyst, 0.05 g; aqueous $FeCl_2$ solution (5 mM, pH 2.5), 250 mL.

[a] Loaded amount of InHCF was determined based on Fe content in InHCF which was regarded as $KIn[Fe(CN)_6]$.

Reduction-cocatalysts-loaded or unloaded TaON powder was modified with InHCF nanoparticles via an impregnation method. TaON samples were immersed in a water dispersed with a certain amount of InHCF particles. The solution was dried up and then heated at 373 K for 1 h under Ar flow (20 mL min^{-1}). Unless otherwise noted, the loading amount of InHCF was 10 mol% as Fe in InHCF with respect to TaON based on the assumption that the composition of InHCF nanoparticles was $KIn[Fe(CN)_6]$. The loading amount was determined based on the results in Table 4-1. InHCF-modified sample is denoted as InHCF/$Rh_xCr_{2-x}O_3$/TaON, for example. For a control experiment, the modification with $InCl_3$ instead of InHCF nanoparticles was conducted via the same procedure.

4.2.3. Characterization

The prepared samples were characterized by powder X-ray diffraction (XRD; Mini Flex II, Rigaku, X-ray source; Cu Kα) measurement, UV–visible diffuse reflectance spectroscopy (UV–vis DRS; V-650, JASCO) and attenuated total reflectance-Fourier transform infrared spectroscopy (ATR-FTIR, ATR; ATR Pro One, JASCO, FT-IR; FT-4200, JASCO) using a diamond prism. ATR-FTIR spectra were recorded against air as a background. The crystal structures were drawn using the VESTA program.[41] The samples were also characterized by scanning electron microscopy (SEM; NVision 40, Carl Zeiss-SIINT), transmission electron microscopy (TEM; JEM-2100F, JEOL), and X-ray photoelectron spectroscopy (XPS; MT-5500, ULVAC-PHI, Inc., X-ray source: Mg Kα). The binding energies in XP spectra were calibrated with reference to the Au $4f_{7/2}$ peak position (84.0 eV) of the deposited Au metal on the samples. X-ray absorption fine structure (XAFS) experiments were carried out at the PF-AR NW10A. The Brunauer-Emmett-Teller (BET) surface area was measured by using a BELSORP-mini II (Microtrac BEL) at liquid nitrogen temperature (77 K). ζ potentials of InHCF/TaON, TaON and InHCF were measured in aqueous solution using a ζ potential analyzer (Zetasizer Nano ZS, Malvern Instruments). The pH of the solution was adjusted by1 M aqueous HCl.

4.2.4. Electrochemical and photoelectrochemical measurements.

InHCF, TaON, InHCF/TaON electrode was prepared on a conductive FTO glass by a squeegee method. A slurry of the respective samples in water was pasted on a FTO glass and then heated at 373 K for 1 h under Ar flow (20 mL min^{-1}). The coated area and the deposited amount were fixed at approx. 1.5 × 1.5 cm^2 and 1.0 ± 0.3 mg, respectively.

The reduction cocatalyst (i.e., Pt, Rh or $Rh_xCr_{2-x}O_3$) -deposited electrode was prepared through a spin-coating technique. For the deposition of Pt or Rh species, a methanol–water mixed solution (1:1, 20 μL) containing $H_2PtCl_6 \cdot 6H_2O$ or $Rh(NO_3)_3$ (10 mM, 80.0%; Kanto Chemical Co., Inc.) was dropped on a conductive fluorine-doped tin oxide (FTO) glass (1.5 × 2.5 cm^2), spin-coated (500 rpm, 5 s followed by 1000 rpm, 120 s), and then heated at 473 K for 1 h under an H_2 flow (20 mL min^{-1}). For $Rh_xCr_{2-x}O_3$, the same procedure was applied except for the use of a methanol–water mixed solution (1:1, 20 μL) containing $Rh(NO_3)_3$ (10 mM) and $Cr(NO_3)_3$ (30 mM, 98.0%–103.0%; Kanto Chemical Co., Inc.) and calcination at 673 K in air.

Electrochemical or photoelectrochemical measurements were performed in an aqueous solution of K_2SO_4 (0.1 M, 99.0%; FUJIFILM Wako Pure Chemical Corporation, pH 2.5, adjusted by H_2SO_4) as an electrolyte under Ar atmosphere using a three-electrode cell. The prepared electrode as the working electrode, Pt coil as the counter electrode, Ag/AgCl as the reference electrode were connected to a potentiostat (VersaSTAT 4, AMETEK), and then cyclic voltammograms or linear sweep voltammograms were recorded. For photoelectrochemical measurement, the photocatalyst electrodes were irradiated with intermittent visible light ($\lambda > 400$ nm) by a 300 W Xe lamp equipped with a CM-1 cold mirror and an L-42 cutoff filter. In some cases, $FeCl_3$ (5–20 mM, 99.0%–102.0%; FUJIFILM Wako Pure Chemical Corporation) or $FeCl_2$ (1 mM) was added to the electrolyte solution.

4.2.5. Photocatalytic reaction.

Photocatalytic reactions were conducted in Pyrex side-illuminated reaction vessel connected to a glass closed gas-circulation system. A 300 W Xe lamp was used as a light source in combination with a CM-1 cold mirror and an L-42 cutoff filter for illumination with visible light ($\lambda > 400$ nm). For the photocatalytic H_2 evolution, the prepared photocatalyst powder (0.05 g) was dispersed in 250 mL of aqueous $FeCl_2$ solution (5 mM, pH 2.5 adjusted with HCl). The suspension was irradiated with visible light after thoroughly degassed and purged with Ar. The evolved gases were analyzed by a gas chromatograph (GC-8A, Shimadzu, TCD detector, MS 5A column, Ar carrier) directly connected to the closed gas-circulation system. In some cases, aqueous $FeCl_2$ solution (1 or 2.5 mM, pH 2.5) or aqueous MeOH solution (20vol%) was used as the reaction solution.

To measure the apparent quantum efficiency (AQE), a monochromatic light (λ = 420 nm) was used with a Xe lamp (MAX-303, Asahi Spectra Co., Ltd.).

For the photocatalytic Z-scheme water splitting under visible light, the same

experimental setting was applied, except the use of $BiVO_4$ or the surface-treated WO_3 powder in addition to the InHCF/$Rh_xCr_{2-x}O_3$/TaON photocatalyst (0.05 g each) and an aqueous $FeCl_2$ solution (2 mM, pH 2.5 adjusted with HCl). Z-scheme water splitting was also conducted under the simulated solar irradiation. A solar simulator (HAL-320, ASAHI SPECTRA, AM 1.5G, 100 mW cm^{-2}) was used as a light source. InHCF/$Rh_xCr_{2-x}O_3$/TaON and the surface-treated WO_3 powder (0.05 g each) was dispersed in 100 mL of aqueous $FeCl_2$ solution (2 mM, pH 2.5 adjusted with HCl). After thoroughly degassed and purged with Ar, the suspension was irradiated with the solar simulator. The evolved gases were analyzed by a gas chromatograph (GC-8A, Shimadzu, TCD detector, MS 5A column, Ar carrier) directly connected to the closed gas-circulation system. The STH was determined by Equation 1.

$$\text{STH}\ (\%) = (R(H_2) \times \Delta G) / (P \times S) \times 100, \qquad \text{(Eq. 1)}$$

where $R(H_2)$, ΔG, P and S, respectively describe the rate of H_2 evolution during the water-splitting, the Gibbs energy for the reaction (237 kJ mol^{-1}), the photon energy intensity (100 mW cm^{-2}), and the irradiation area (approx. 15 cm^{-2}).

4.2.6. Chemical reaction of Fe^{2+} and an oxidized form of InHCF (InHCF-ox). InHCF-ox (100 μmol as $In[Fe^{III}(CN)_6]$) powder was added to 100 mL of aqueous $FeCl_2$ solution (0.9 mM, pH 2.5 adjusted by 1M HCl), and then the solution was stirred by a magnetic stirrer under the dark condition. The quantitative analysis of Fe^{2+} and Fe^{3+} in the solution was performed by a colorimetric method as follows. A portion of sample aliquots (1 mL) was withdrawn from the solution after each interval of stirring and filtered by a syringe filter (Millex, Millipore) to remove the InHCF-ox particles. As for Fe^{2+}, 50 μL of the supernatant solution was added to the mixture of 2,4,6-tris(2-pyridyl)-1,3,5-triazine (TPTZ; 1.0 mM, 700 μL) and acetate buffer (pH 5.2, 2 M, 2.1 mL) in a quartz cell to form the Fe(II)–TPTZ complex.[42,43] The amount of Fe^{2+} was determined based on the peak absorbance at 597 nm attributed to Fe(II)–TPTZ complex[42,43] by using UV–vis spectroscopy (UV-1800, Shimadzu). As for Fe^{3+}, 500 μL of the filtered solution after the reaction and 2000 μL of HCl (6 M) were mixed in a quartz cell, and then the UV–vis absorption spectra of the solution were measured. The amount of dissolved Fe^{3+} was estimated based on the absorbance at 430 nm.

4.3. RESULTS AND DISCUSSION

4.3.1. Characterization of InHCF nanoparticles

Indium hexacyanoferrate (InHCF) nanoparticles were prepared according to a previously published method for the preparation of MHCF nanoparticles containing either Fe, Co, or Ni cations, but not In.[40] Although no crystallographic data has been reported in the ICDD for InHCF, the XRD patterns of the fabricated InHCF particles (Figure 4-5a) resembled those of previously reported InHCF samples with relatively large particle sizes (~200 nm).[44,45] The ATR-FTIR spectrum (Figure 4-6a) of the InHCF samples contained absorption bands at ~2100–2070 cm^{-1}, assignable to the stretching vibration mode of C≡N, as is generally observed in MHCFs,[20] differing markedly from those of $K_4[Fe(CN)_6]\cdot 3H_2O$ (2044 cm^{-1}) and its oxidized form $K_3[Fe(CN)_6]$ (2117 cm^{-1}). Because InHCFs exhibit mainly absorption in the UV region (Figure 4-6b), they do not hinder the visible-light absorption of TaON photocatalysts. The TEM images of the InHCF samples (Figure 4-5b) revealed irregularly shaped nanoparticles with diameters < 100 nm. The surface area was estimated to be 39.7 $m^2\,g^{-1}$ by employing N_2 absorption measurements and the BET method. The elemental composition of the InHCF sample, $K_hIn_k[Fe(CN)_6]_l$, (*h, k, l*: composition ratios) was tentatively estimated using surface-sensitive XPS, because bulk analysis using energy-dispersive X-ray spectroscopy is complicated by the overlap of the In Lα and K Kα peaks. The XPS analysis results indicated that the ratio of K:In:Fe (*h*:*k*:*l*) near the surface was approximately 0.7:1.0:0.9, implying that the as-synthesized InHCF sample consisted predominantly of $KIn[Fe(CN)]_6$, that is, *h*:*k*:*l* = 1:1:1, along with a fraction of In-rich phases, such as $In_4[Fe(CN)_6]_3$ (i.e., *h*:*k*:*l* = 0:4:3). The results of Le Bail refinement of the experimental XRD pattern (Figure 4-7) also supported the assumption that the present InHCF sample was mainly composed of $KIn[Fe(CN)]_6$ species. The MHCFs employed should exhibit good reversibility of the Fe^{III}/Fe^{II} redox cycle, with a redox potential appropriate for targeted photocatalysis. As shown in Figure 4-5c, reversible redox behavior with sharp peaks was observed, and the half-wave potential (0.93 V vs. SHE, pH 2.5) of Fe^{III}/Fe^{II} agreed well with the literature values,[46,47] which is appropriate for the oxidation of Fe^{2+} cations in aqueous solution, i.e., more positive than that of Fe^{3+}/Fe^{2+} (0.77 V vs. SHE, pH 2.5). The redox reaction occurring on InHCF can be described by Equation 2, where divalent and trivalent iron species coexist, as suggested in previous studies:

$$KIn[Fe^{II}(CN)_6] \rightleftharpoons K_{1-x}In[Fe^{II}_{1-x}Fe^{III}_{x}(CN)_6] + xK^+ + xe^-, \qquad \text{(Eq. 2)}$$

where x is the number of moles of reacted electrons.

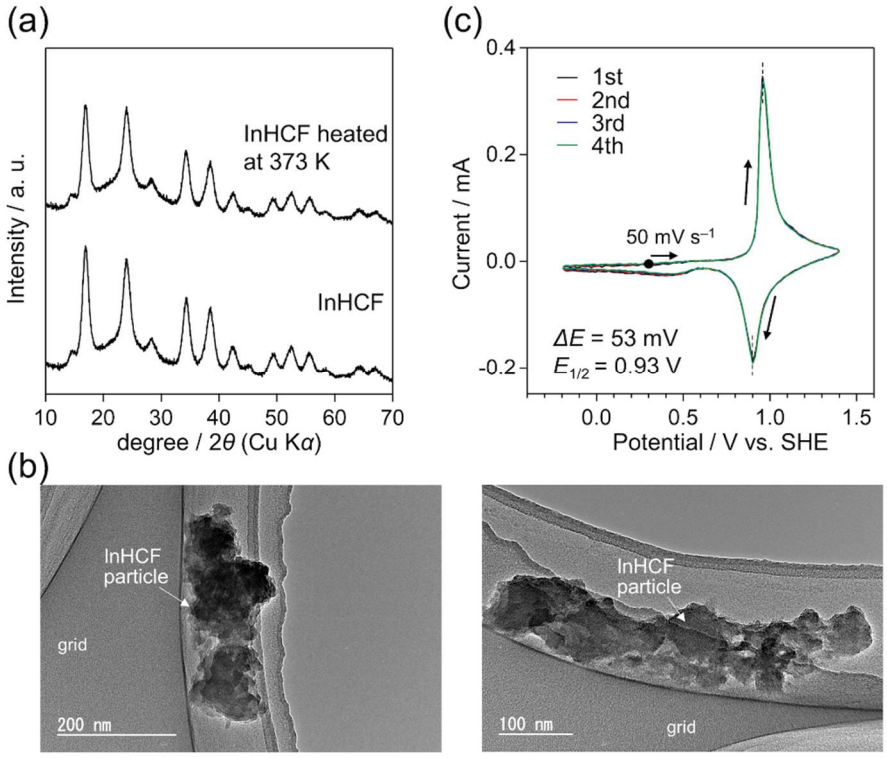

Figure 4-5. Characterization of InHCF nanoparticles: (a) XRD patterns, (b) TEM images, and (c) cyclic voltammograms obtained using an InHCF-nanoparticle-deposited FTO electrode at a scan rate of 50 mV s^{-1} in aqueous K_2SO_4 solution (0.1 M, 40 mL) at pH 2.5.

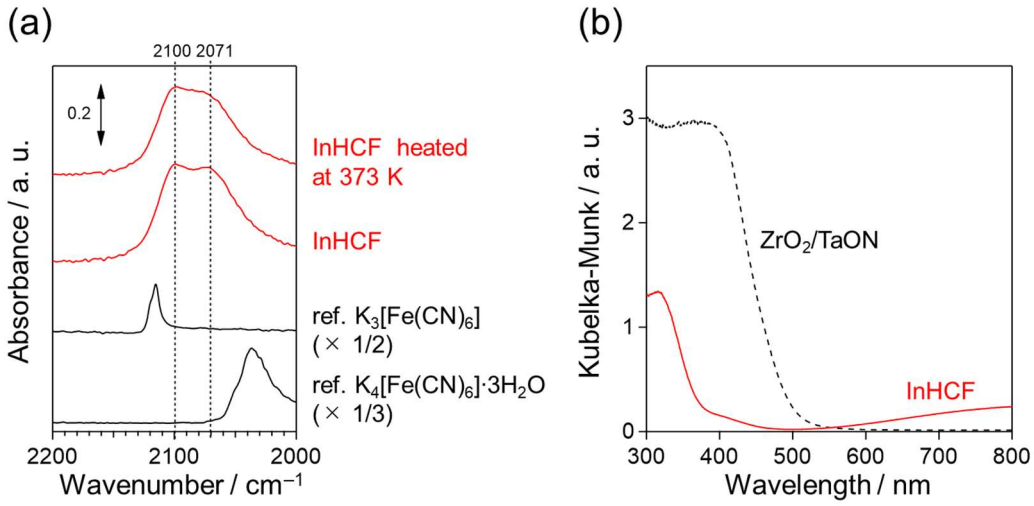

Figure 4-6. (a) ATR-IR spectra and (b) DRS spectra of InHCF nanoparticles, along with some references.

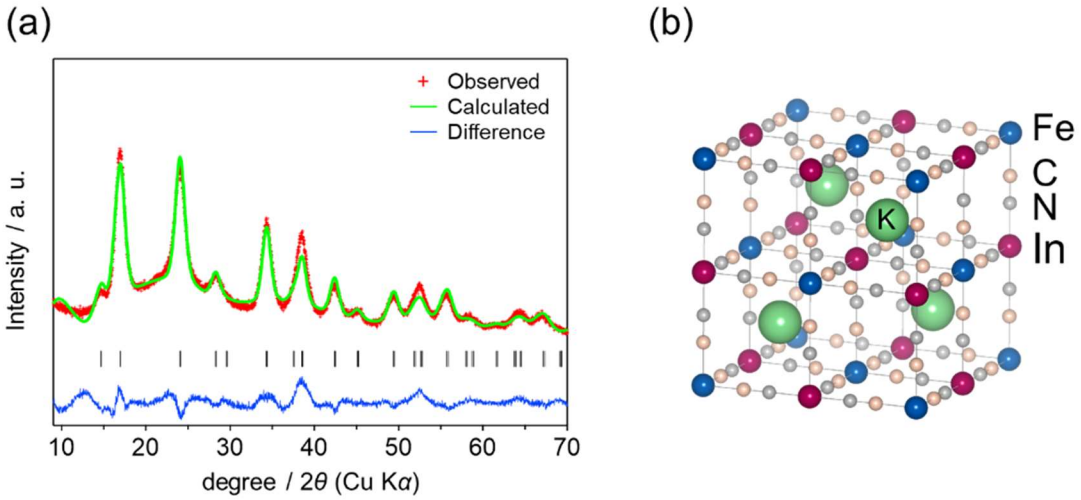

Figure 4-7. (a) Le Bail refinement of experimental XRD pattern of InHCF nanoparticle for $KIn[Fe(CN)_6]$ and (b) crystal structure of $KIn[Fe(CN)_6]$.

4.3.2. Characterization of TaON modified with a conventional H_2-evolution cocatalyst and InHCF.

Figure 4-8 shows TEM images of TaON loaded with a well-known H_2 evolution cocatalysts ($Rh_xCr_{2-x}O_3$, Pt, or Rh), along with that of the unmodified sample. Hereafter, $Rh_xCr_{2-x}O_3$ is denoted as RCO for simplification. Nanoparticles of RCO with an average diameter of 2 nm were highly dispersed on the surface of the TaON. In contrast, Pt and Rh particle sizes were not homogeneous and were larger than those of RCO, with inferior dispersion. Figure 4-9 shows TEM images of the RCO/TaON sample further modified with InHCF (InHCF/RCO/TaON), wherein it is evident that the TaON surface was densely covered by a layer of InHCF particles with a thickness of 20–100 nm. Although the relatively thick InHCF layers obscured the preloaded RCO nanoparticles in the TEM images, characterization using XPS, XRD, and ATR-FTIR confirmed the presence of RCO species as well as the retention of their physicochemical properties (Figures 4-10, 4-11). Likewise, it was confirmed that the physicochemical properties of InHCF remained unchanged after loading onto TaON. Similar results were observed for the InHCF/Pt/TaON and InHCF/Rh/TaON samples (Figures 4-12~4-15).

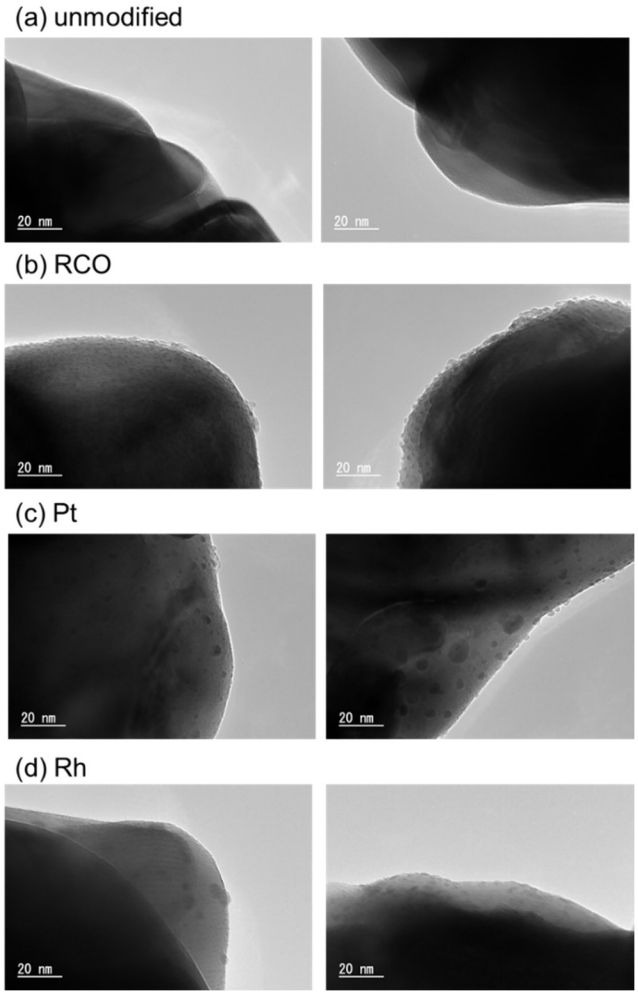

Figure 4-8. TEM images of (a) unmodified TaON particles or (b –d) TaON particles loaded with various reduction cocatalysts.

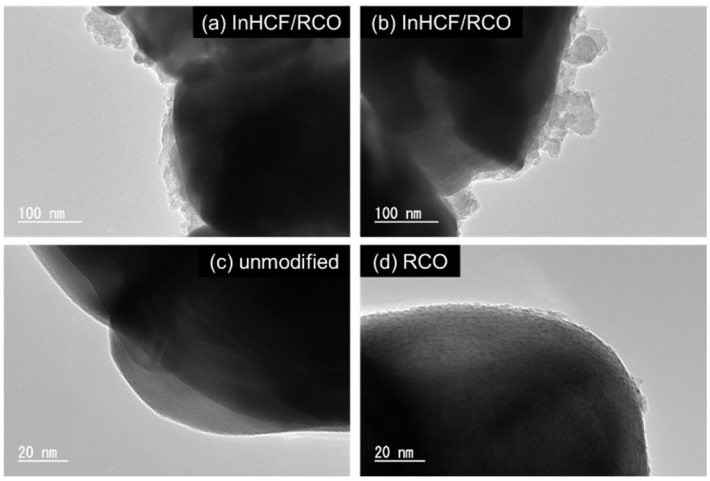

Figure 4-9. TEM images of (a,b) InHCF/RCO/TaON, (c) unmodified TaON, and (d) RCO/TaON.

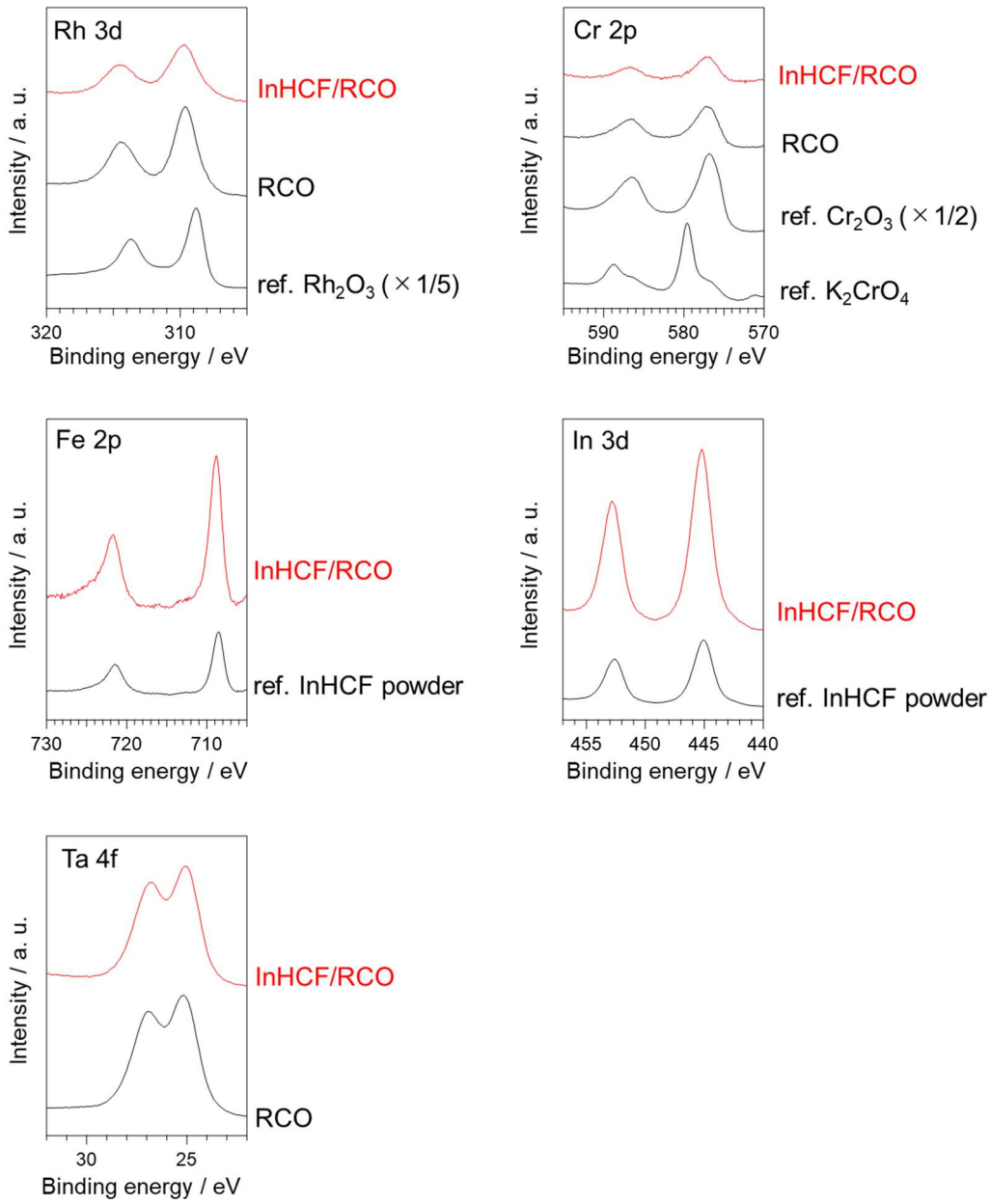

Figure 4-10. XP spectra of InHCF/RCO/TaON, along with those of some reference samples. Note that the XP spectra of InHCF/RCO/TaON were normalized by the intensity of Ta $4f_{7/2}$ peak of RCO/TaON.

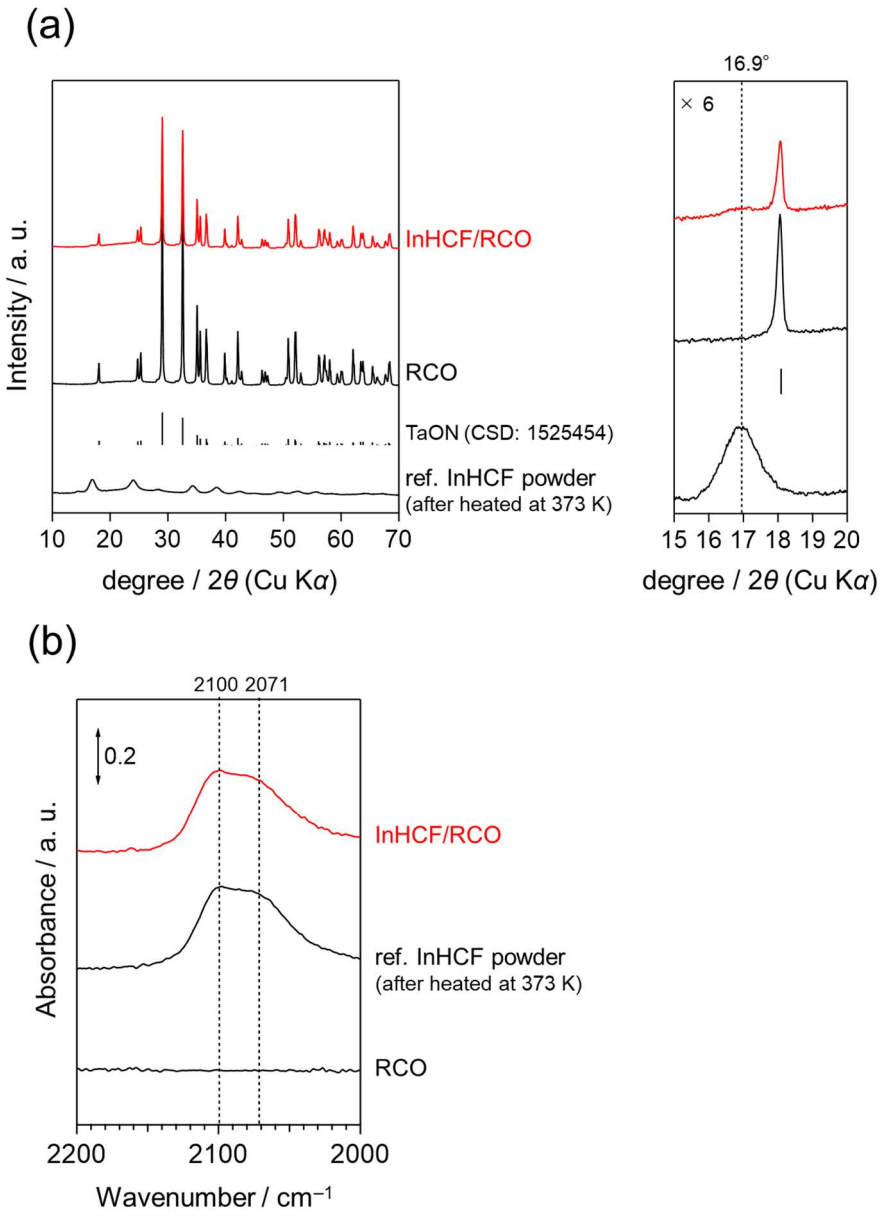

Figure 4-11. (a) XRD patterns and (b) ATR-FTIR spectra of InHCF/RCO/TaON, along with those of RCO/TaON and InHCF powder as references.

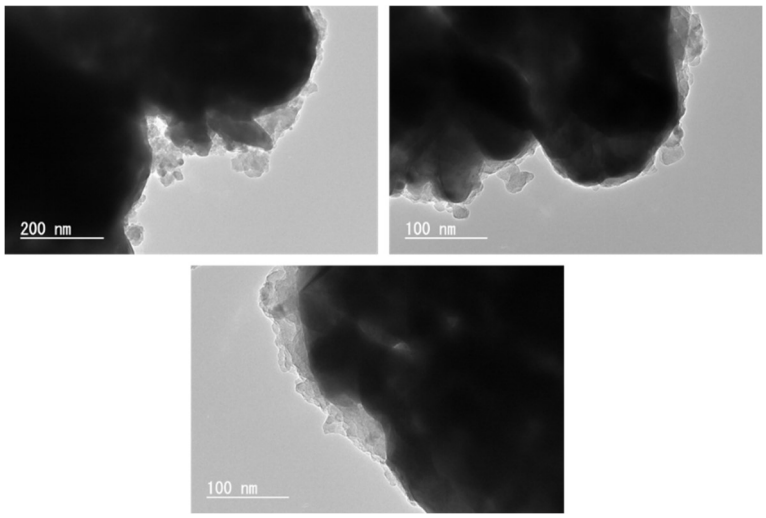

Figure 4-12. TEM images of InHCF/Pt/TaON.

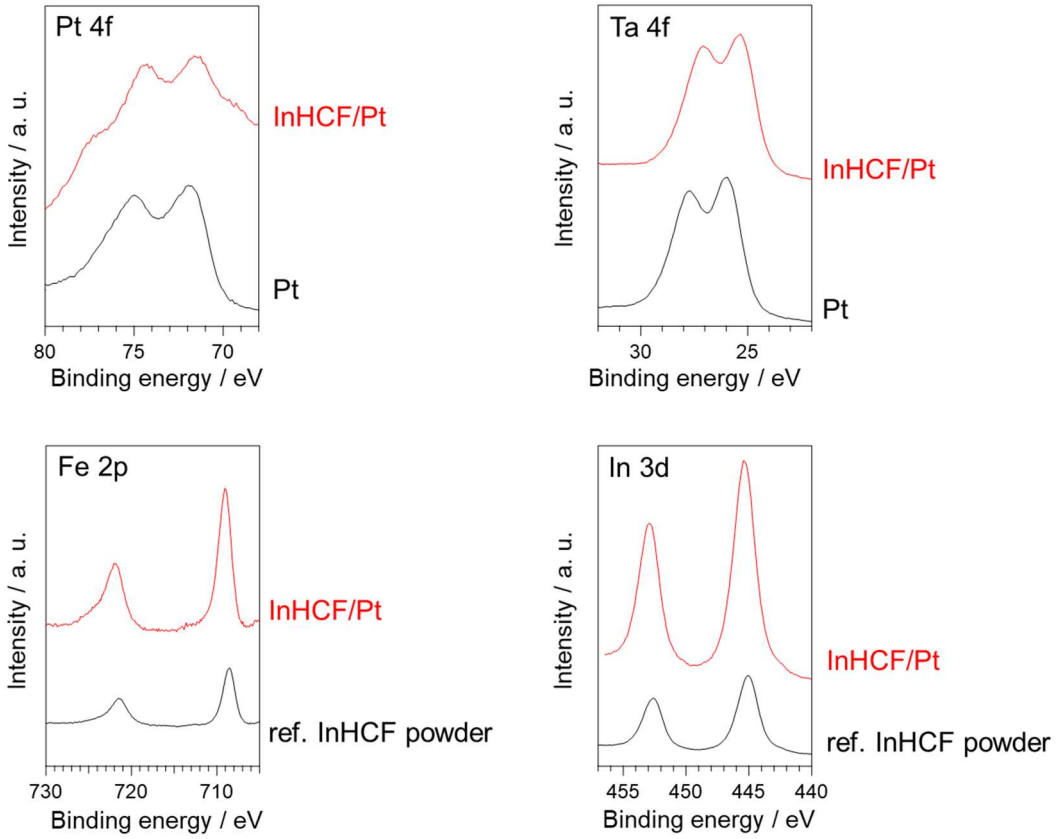

Figure 4-13. XP spectra of InHCF/Pt/TaON, along with those of some reference samples. Note that the XP spectra of InHCF/Pt/TaON were normalized by the intensity of Ta $4f_{7/2}$ peak of Pt/TaON.

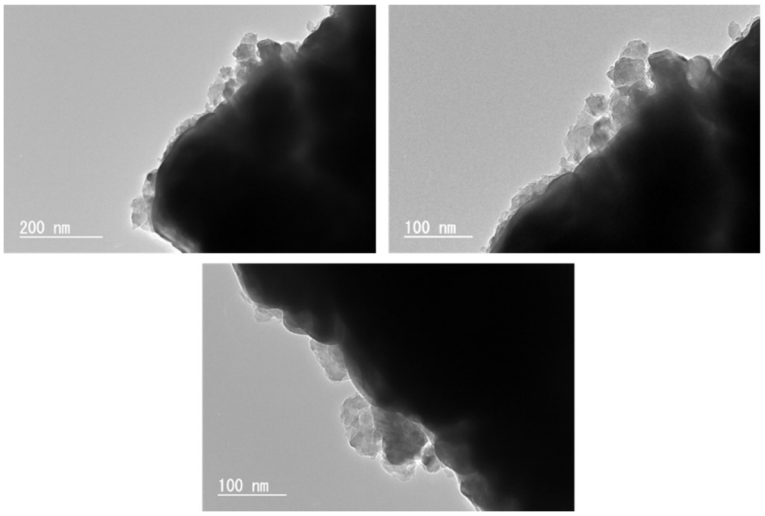

Figure 4-14. TEM images of InHCF/Rh/TaON.

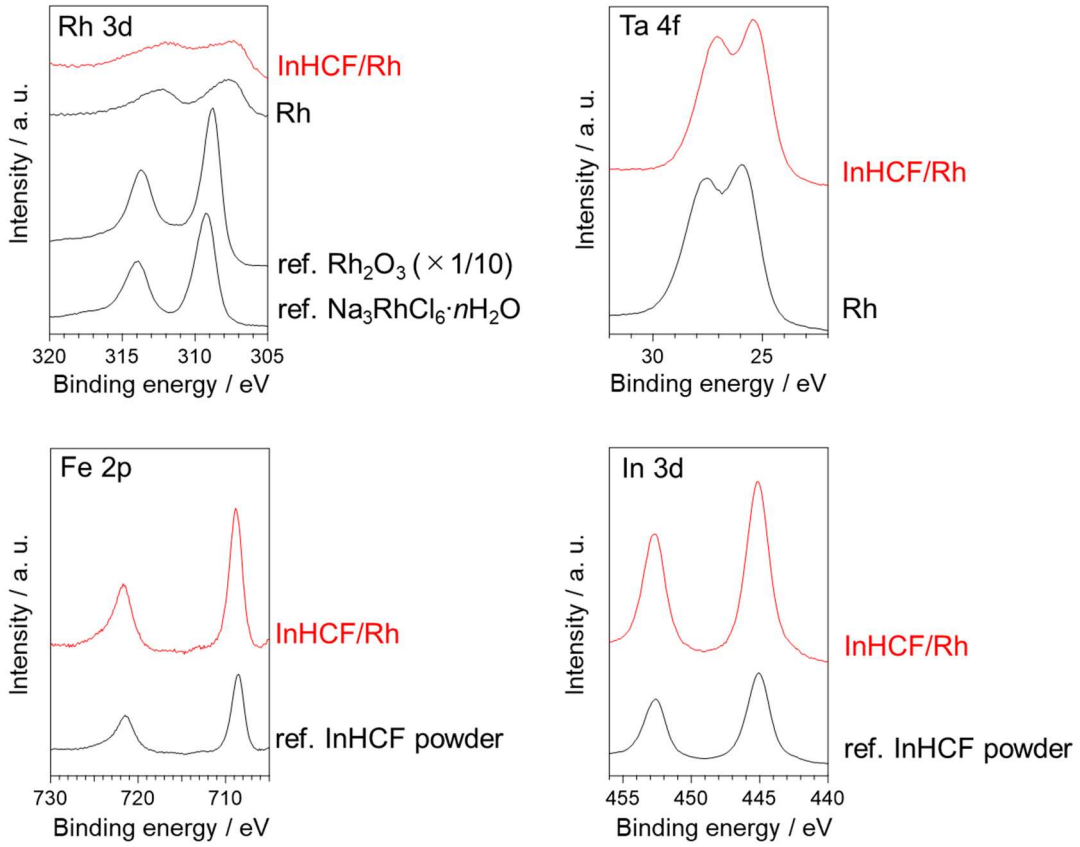

Figure 4-15. XP spectra of InHCF/Rh/TaON, along with those of some reference samples. Note that the XP spectra of InHCF/Rh/TaON were normalized by the intensity of Ta $4f_{7/2}$ peak of Rh/TaON.

4.3.3. Effects of InHCF modification on H_2 evolution in the presence of Fe^{2+} electron donor

Figure 4-16 shows the H_2 evolution using TaON photocatalysts and an Fe^{2+} electron donor under visible-light irradiation (λ > 400 nm). Modification with either InHCF or RCO slightly enhanced the H_2 evolution activity; however, the resulting H_2 evolution rates were still exceedingly low (< 5 μmol h^{-1}). In contrast, the co-loading of InHCF and RCO resulted in H_2 evolution at a significantly higher rate (123 μmol h^{-1}). The total amount of generated H_2 reached 659 μmol, which is close to the stoichiometric amount calculated based on the amount of added Fe^{2+} (1250/2 = 625 μmol), strongly implying that almost all Fe^{2+} cations were oxidized to Fe^{3+} by the photogenerated holes on TaON, accompanied by stoichiometric water reduction to H_2. The higher stoichiometric amount of H_2 produced can be rationalized by considering the oxidation of residual organic contaminants by holes, given that a small amount of H_2 (14 μmol) was generated from InHCF/RCO/TaON in the absence of Fe^{2+} (Figure 4-17). Neither modification with $InCl_3$ nor the simple addition of InHCF nanoparticles to the solution improved the activity of RCO/TaON (Figure 4-18), indicating that the loading of InHCF species onto the TaON surface is essential for enhancing H_2 evolution. Importantly, no changes were observed in the XPS and ATR-FTIR spectra of InHCF/RCO/TaON after the reaction (Figure 4-19). The apparent H_2 evolution quantum efficiency of InHCF/RCO/TaON under similar conditions, but with monochromatic light, was 1.2% at 420 nm. Figure

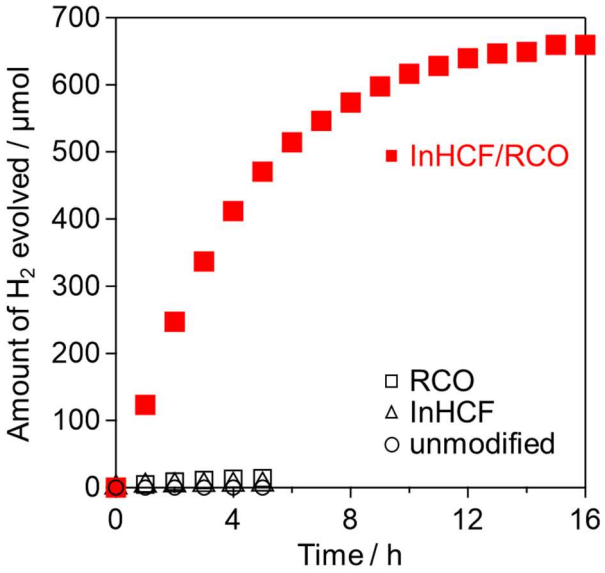

Figure 4-16. H_2 evolution with time over InHCF/RCO/, RCO/, or InHCF/TaON and unmodified TaON in aqueous $FeCl_2$ solution (5 mM, 250 mL) at pH 2.5 under visible light irradiation (λ > 400 nm).

4-20 shows a comparison of the H_2 evolution activities of InHCF-modified and unmodified TaON preloaded with Pt or Rh instead of RCO. In both cases, co-loading promoted H_2 evolution, although the rates were substantially lower than those of InHCF/RCO/TaON.

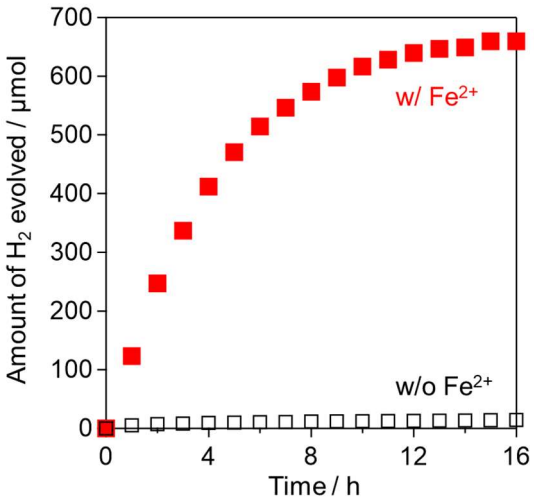

Figure 4-17. Time courses of H_2 evolution of InHCF/RCO/TaON photocatalysts from aqueous solution in the presence or absence of $FeCl_2$ (5 mM, 250 mL) at pH 2.5 under visible light irradiation.

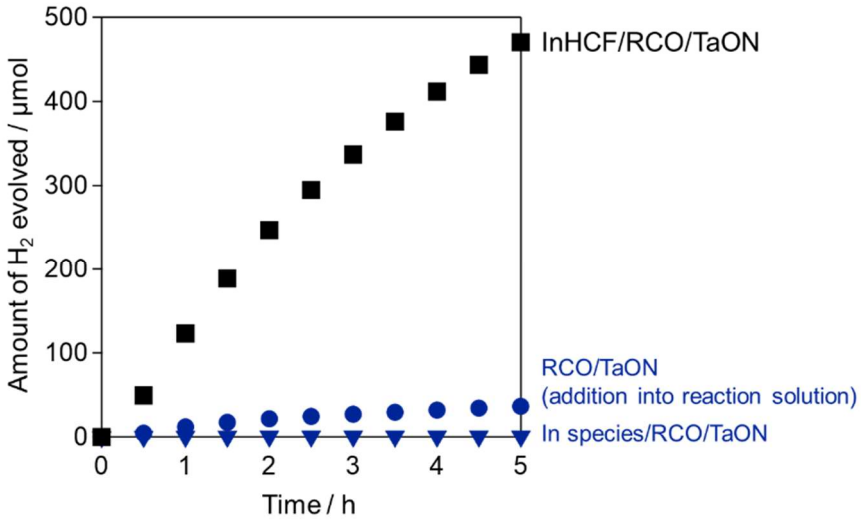

Figure 4-18. The effect of the addition of InHCF into the reaction solution (blue circle) and the modification with In species (precursor: $InCl_3$, blue triangle) on the H_2 evolution over RCO/TaON from aqueous $FeCl_2$ solution (5 mM, 250 mL) at pH 2.5 under visible light irradiation.

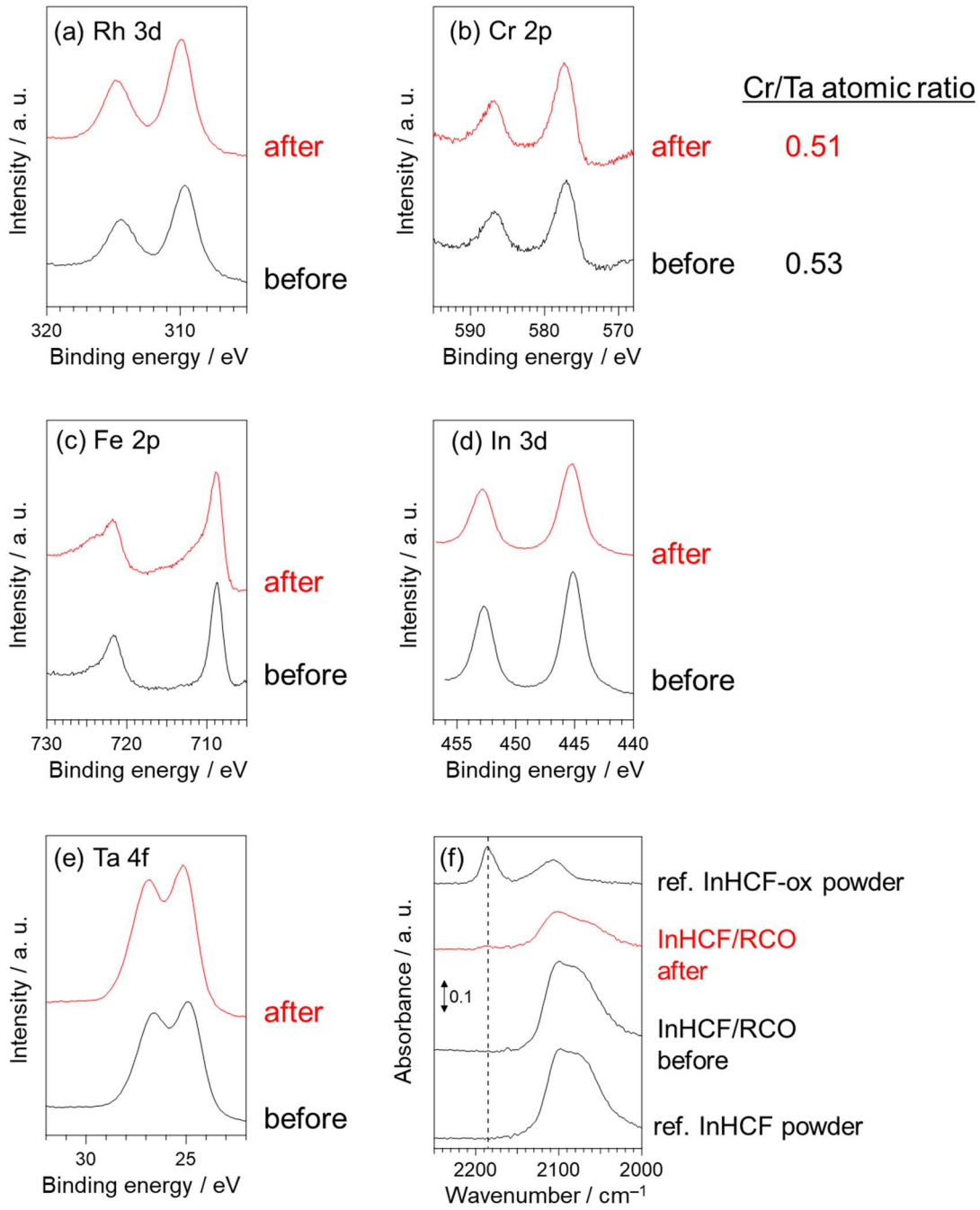

Figure 4-19. (a)–(e) XP spectra and (f) ATR-FTIR spectra of InHCF/RCO/TaON after 10 h of visible-light irradiation in aqueous $FeCl_2$ solution (5 mM, 250 mL) at pH 2.5.

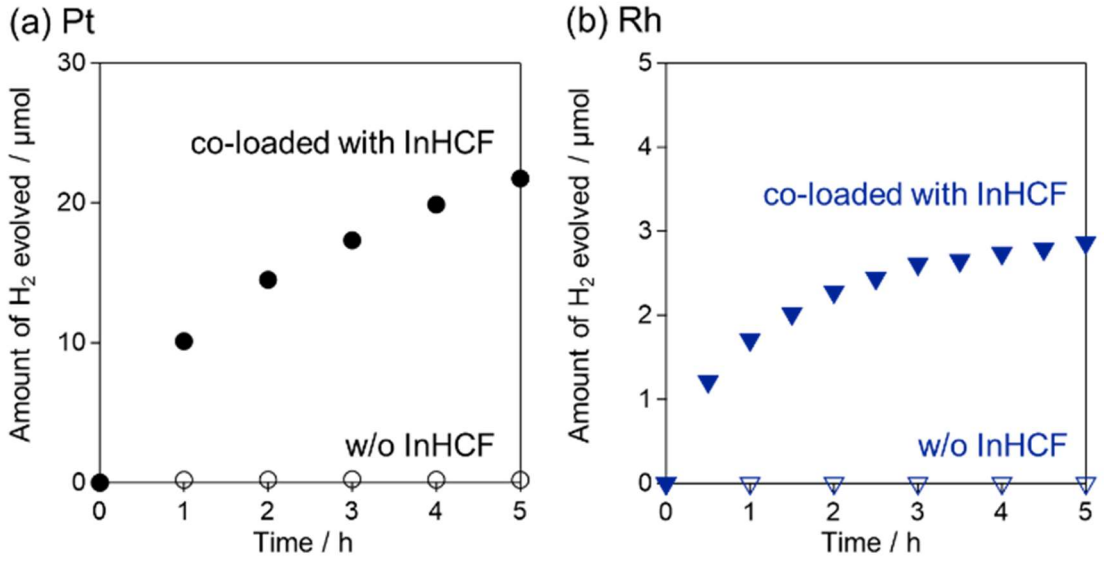

Figure 4-20. H_2 evolution with time over InHCF-modified or unmodified (a) Pt/TaON or (b) Rh/TaON in aqueous $FeCl_2$ solution (5 mM, 250 mL) at pH 2.5 under visible light irradiation.

4.3.4. Mechanism of H_2 evolution enhancement due to co-modification of TaON with InHCF and RCO

The above results indicate that the InHCF species endow the originally inactive TaON photocatalyst with H_2 evolution activity using an Fe^{2+} electron donor. Presumably, the InHCF species function as specific Fe^{2+} oxidation sites, similar to the Rh^{3+} species doped in $SrTiO_3$ semiconductor particles.[11] This assumption is strongly supported by the finding that co-modification with InHCF promoted H_2 evolution from aqueous Fe^{2+}, regardless of the type of reduction cocatalyst (RCO, Pt, or Rh), to a greater or lesser extent (Figures 4-16, 4-20). Notably, TaON loaded solely with InHCF did not exhibit H_2 evolution when methanol (MeOH) was used as an irreversible electron donor (< 0.1 μmol h^{-1}), indicating the inertness of InHCF for H_2 evolution.

Figure 4-21 shows the photoelectrochemical measurement results for InHCF/TaON or unmodified TaON particles deposited on a conductive FTO electrode; evidently, InHCF modification led to a 7- to 12-fold increase in the photocurrent in the presence of Fe^{2+}, indicating the favorable catalytic activity of the InHCF species for the oxidation of Fe^{2+}. As mentioned above, the redox potential of Fe^{III}/Fe^{II} in InHCF was determined to be ~+0.93 V vs. SHE at pH = 2.5 (Figure 4-5c); the photogenerated holes in TaON (valence band maximum of 2.05 V at pH 2.5[48]) can thermodynamically oxidize the Fe^{II} species in InHCF. In addition, the oxidized forms of InHCF, $In[Fe^{III}(CN)_6]$

(InHCF-ox) particles, were revealed to oxidize Fe^{2+} cations in aqueous solution at pH 2.5. As shown in Figure 4-22, the amount of Fe^{2+} in the solution spontaneously decreased by 15 μmol, accompanied by an increase in Fe^{3+} (11 μmol). Thus, Fe^{2+} oxidation is most likely promoted through the Fe^{III}/Fe^{II} redox cycles in InHCF, whereby the photogenerated holes in TaON oxidize Fe^{II} in InHCF to Fe^{III}, and then the resulting Fe^{III} species oxidize Fe^{2+} cations in the solution to Fe^{3+}, as illustrated in Scheme 4-1. It should be noted that InHCF loading on TaON led to an increase in the photocurrent, even in the absence of Fe^{2+} (Figure 4-21c), suggesting that the InHCF species capture the photogenerated holes in TaON to some extent. Therefore, it can be concluded that the InHCF nanoparticles loaded onto the TaON photocatalyst surface functioned as an effective cocatalyst for Fe^{2+} oxidation by photogenerated holes of TaON, thereby drastically enhancing the H_2 evolution initiated by photoexcited electrons on H_2 evolution cocatalysts, such as RCO.

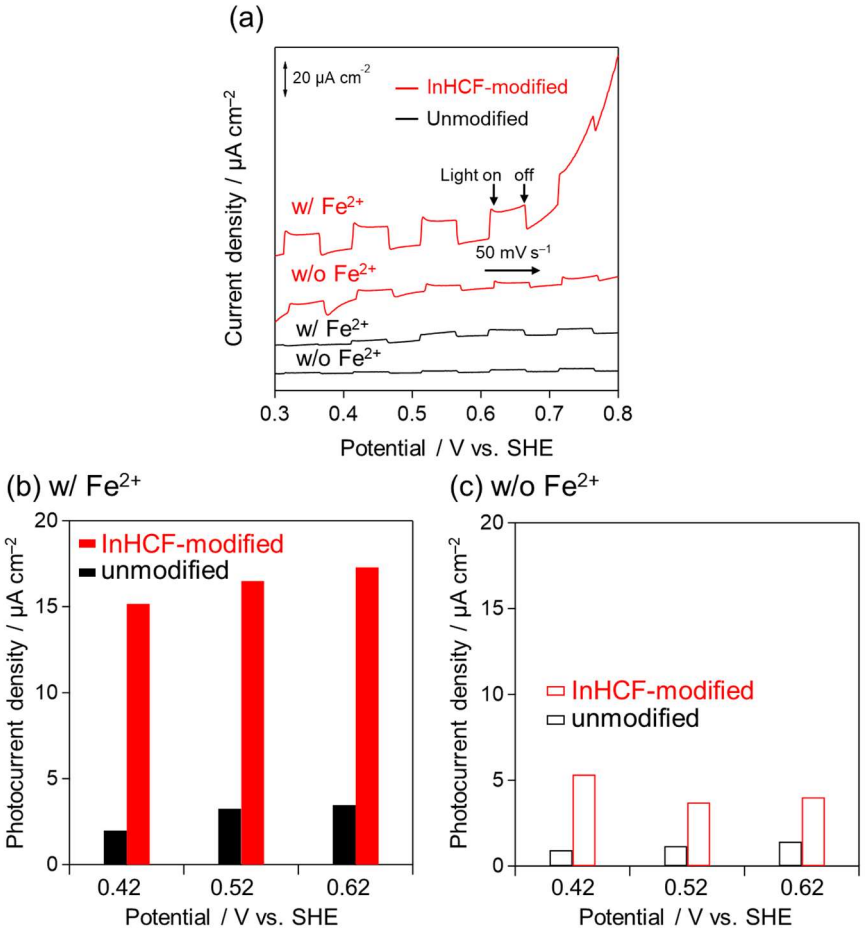

Figure 4-21. (a) Linear sweep voltammograms and (b) photocurrent densities of InHCF-modified or unmodified TaON/FTO in aqueous K_2SO_4 solution (0.1 M, 80 mL) at pH 2.5 with (w/) and without (w/o) $FeCl_2$ (1 mM) under visible light irradiation.

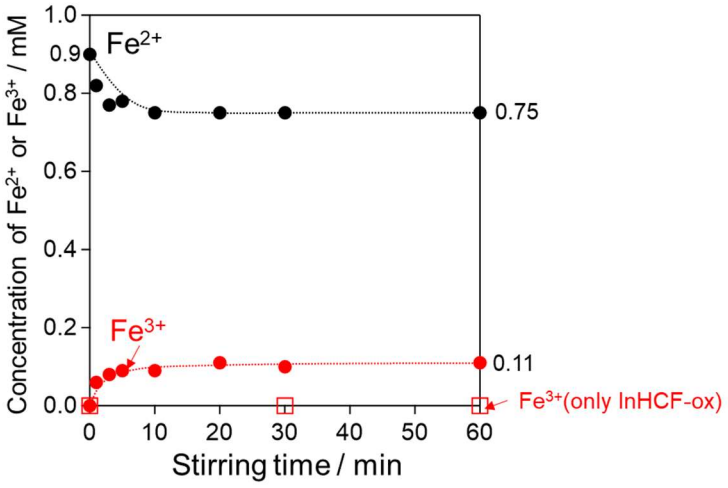

Figure 4-22. Time courses of concentration of Fe^{2+} or Fe^{3+} in 100 mL of $FeCl_2$ aqueous solution (initial concentration of Fe^{2+}, 0.9 mM; pH 2.5), in which the oxidized form of InHCF (InHCF-ox) particles (100 μmol) was dispersed. Note that the blank experiment was also conducted in aqueous solution without Fe^{2+} at pH 2.5 and denoted as "Fe^{3+}(only InHCF-ox)".

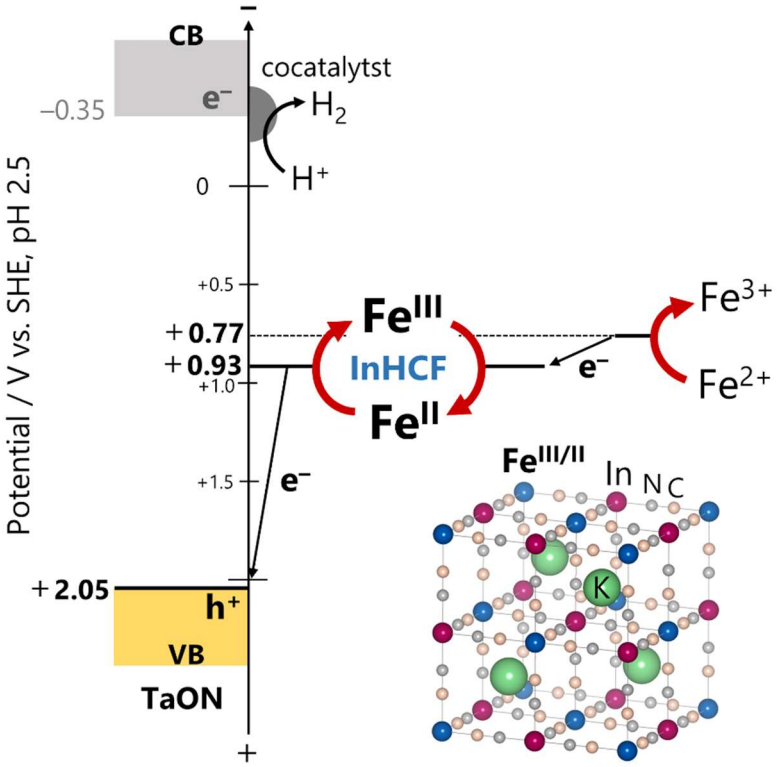

Scheme 4-1. Proposed mechanism of Fe^{2+} oxidation promotion through Fe^{III}/Fe^{II} redox cycles in InHCF.

An important finding was that the combination of InHCF with RCO specifically and drastically promoted H_2 evolution from aqueous Fe^{2+}, whereas that of InHCF and conventional Pt did not (Figures 4-16, 4-20). Because metallic Pt exhibits the lowest overpotential for water (or H^+) reduction,[49] the loading of Pt as a cocatalyst has been proven to enhance H_2 production by various photocatalysts, including TaON, in the presence of appropriate electron donors.[15,32,50] However, when a reversible redox species, such as Fe^{2+} or I^-, is used as an electron donor, Pt metal also catalyzes backward reactions, such as the reduction of Fe^{3+} or I_3^-(IO_3^-),[11,51] significantly lowering the H_2 evolution rate. Indeed, H_2 evolution on Pt/TaON from an aqueous MeOH solution was nearly completely suppressed by the addition of Fe^{3+} cations to the solution (Figure 4-23), indicating a preference for Fe^{3+} reduction over that of H^+. Preferential Fe^{3+} reduction by Pt is further supported by the electrochemical measurement results shown in Figures 4-24a, b; Pt (or Rh) loading onto an FTO substrate led to a significant shift in the onset potential of Fe^{3+} reduction from ~0.4 to 0.8 V (vs. SHE). Although a reduction peak was also generated at ~0.7 V by the RCO-loaded FTO electrode during the cathodic scan (Figure 4-24c), it was independent of the Fe^{3+} concentration. In contrast, the reduction peak with the onset potential of ~0.4 V increased with increasing Fe^{3+} concentration. These results indicate that RCO is considerably less active than Pt toward Fe^{3+} reduction, whereas the RCO cocatalyst has been proven to promote H_2 production on various photocatalysts.[52–54]

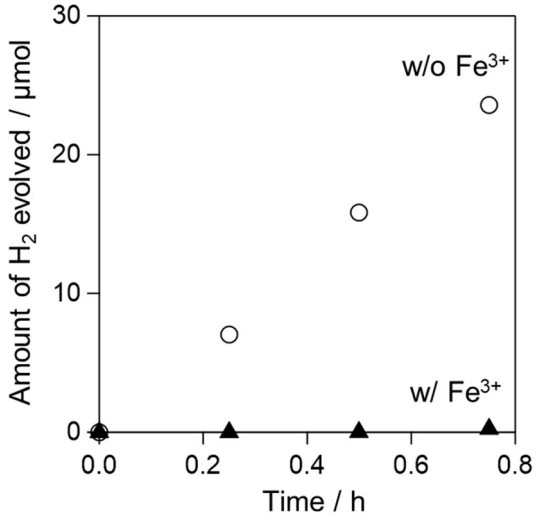

Figure 4-23. Time courses of H_2 evolution of Pt/TaON photocatalysts from aqueous MeOH solution (20 vol%, 250 mL) at pH 2.5 with (w/) or without (w/o) $FeCl_3$ (1 mM) under visible light irradiation.

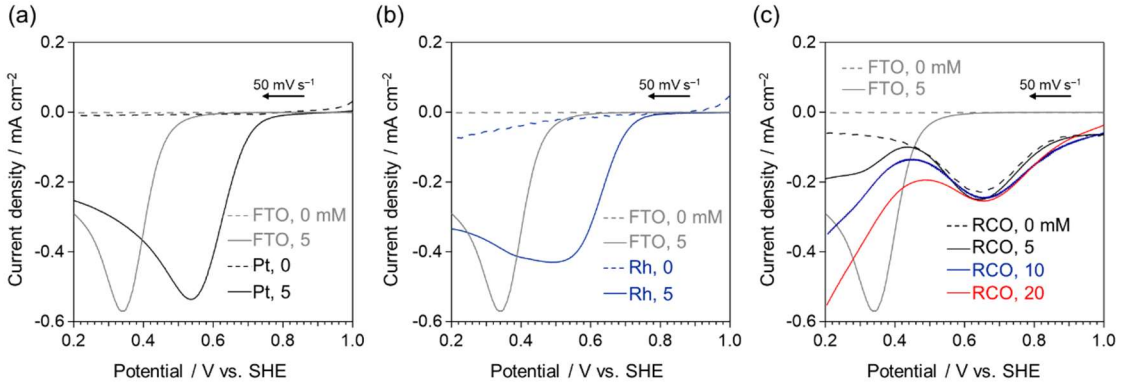

Figure 4-24. (a) Linear sweep voltammograms of (a) Pt-, (b) Rh- or (c) RhCr-deposited FTO in K_2SO_4 aqueous solution (0.1 M, 40 mL) at pH 2.5 in the presence of $FeCl_3$ (0–20 mM), along with those of bare FTO.

The proposed mechanism for the activation of TaON by the co-loading of the InHCF and RCO cocatalysts is illustrated in Schemes 1 and 2. As with most photocatalysts, the surface of TaON is inactive toward the oxidation of Fe^{2+} cations; therefore, the majority of the photoexcited electrons and photogenerated holes recombine even when the photocatalyst is loaded with an effective H_2 evolution cocatalyst, such as Pt or RCO, resulting in negligible H_2 evolution activity (Scheme 2a). Although InHCF loading can promote the photocatalytic oxidation of Fe^{2+} cations to Fe^{3+}, the generated Fe^{3+} cations are preferentially reduced back to Fe^{2+} by the co-loaded Pt (Scheme 2b). By employing RCO as a cocatalyst, which is less active for Fe^{3+} reduction than Pt, water (H^+) reduction by photoexcited electrons and Fe^{2+} oxidation by photogenerated holes proceed efficiently on RCO and InHCF, respectively, ultimately activating the TaON photocatalyst for H_2 production using an Fe^{2+} electron donor (Scheme 2c).

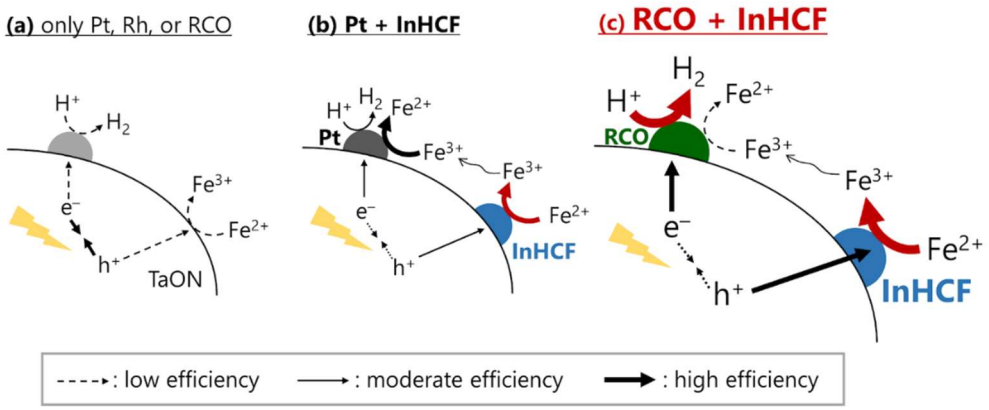

Scheme 2. Proposed mechanism for H_2 evolution enhancement through co-modification of TaON with InHCF and RCO using an Fe^{2+} electron donor.

Interestingly, the developed InHCF/RCO/TaON photocatalyst is capable of stoichiometric H_2 evolution (see Figure 4-16); in other words, it oxidizes Fe^{2+}, even when this cation is present at low concentrations. As shown in Figure 4-25, while the ζ potential of unmodified TaON was considerably positive (+36 mV) at pH 2.5, InHCF modification led to a drastic change in the surface potential to negative values (–14 mV). Thus, it appears that InHCF loading facilitates the approach of Fe^{2+} to the photocatalyst surface, accelerating its oxidation, even at low Fe^{2+}concentrations. This assumption is supported by the observation of enhanced H_2 evolution in the presence of low concentrations of Fe^{2+} (Figure 4-26).

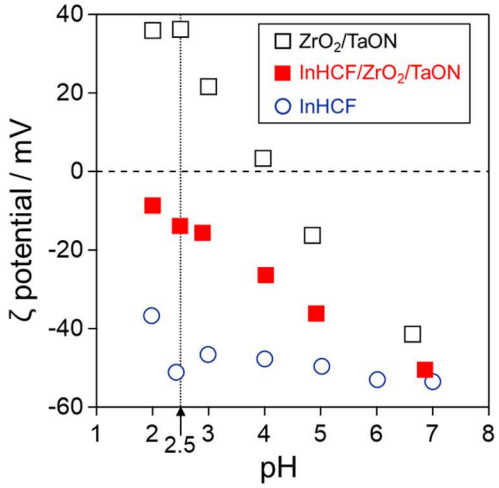

Figure 4-25. ζ potentials of InHCF-modified or unmodified TaON particles, along with that of tje InHCF nanoparticle as references.

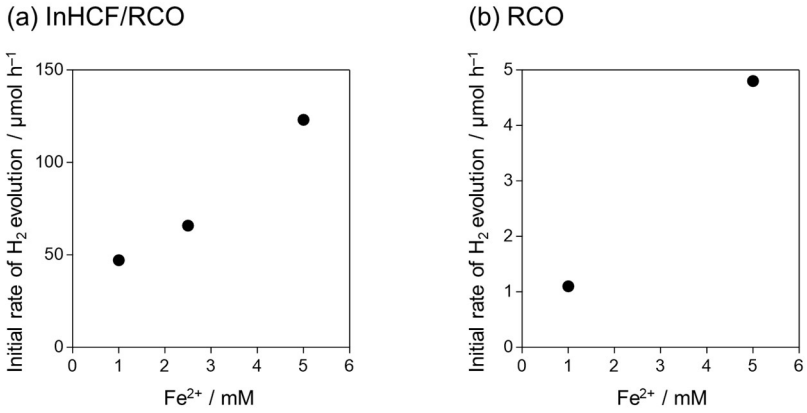

Figure 4-26. Dependence of concentration of Fe^{2+} electron donor on H_2 evolution of (a) InHCF/RCO/TaON and (b) RCO/TaON photocatalysts from 250 mL of 1, 2.5 or 5 mM $FeCl_2$ aqueous solution (pH 2.5) under visible light irradiation.

4.3.5. Effects of various metal species in MHCFs on H_2 evolution and applicability of co-loading to other semiconductor photocatalysts

ZnHCF and FeHCF, in which either Zn^{II} or Fe^{II} is coordinated by the N atom of the CN ligand, were also deposited on the RCO/TaON photocatalyst. The use of these materials in electrodes for secondary ion batteries has been well-studied.[55–58] The half-wave potential of Fe^{III}/Fe^{II} in ZnHCF was determined to be 0.99 V based on its CV profile, while FeHCF provided values of 0.40 V ($Fe^{III/II}$ coordinated to N) and 1.07 V ($Fe^{III/II}$ coordinated to C) (vs. SHE at pH2.5). As shown in Figure 4-27, these MHCFs also promoted H_2 evolution, although the use of InHCF resulted in the highest rate. Although the relationship between the redox potential and the H_2 evolution rate is unclear at present, optimization of the metal species in MHCFs to match the band level of the photocatalyst and the redox potential of the mediator would likely further enhance the oxidation of redox species by photogenerated holes.

To confirm the utility of the co-modification methodology, various visible-light-responsive photocatalysts were modified with InHCF after loading them with an RCO reduction cocatalyst. As shown in Figure 4-28 and Table 4-2, the H_2 evolution activities markedly improved in all cases, indicating the versatility of this method for amplifying H_2 evolution in the presence of Fe^{2+} electron donors. Note that the loading amounts of InHCF and RCO were not optimized; hence, further improvements in the activity were possible. Moreover, the synthesis of photocatalyst particles can be optimized to maximize their desired properties. Recently, the development of synthetic procedures for accessing various photocatalyst materials with superior properties has been intensively studied.[35,59] Considering these factors, further enhancements are expected for the proposed system.

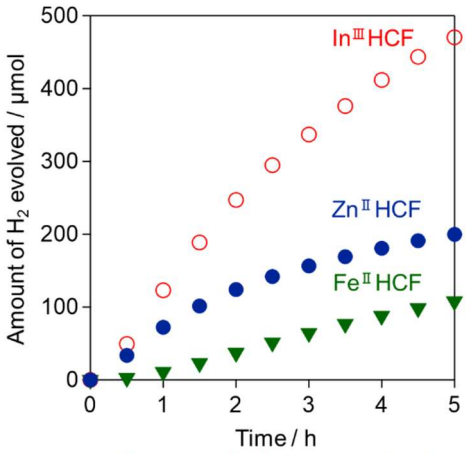

Figure 4-27. Time courses of H_2 evolution over RCO/TaON modified with either ZnHCF or FeHCF instead of InHCF from aqueous $FeCl_2$ solution (5 mM, 250 mL) at pH 2.5 under visible light irradiation.

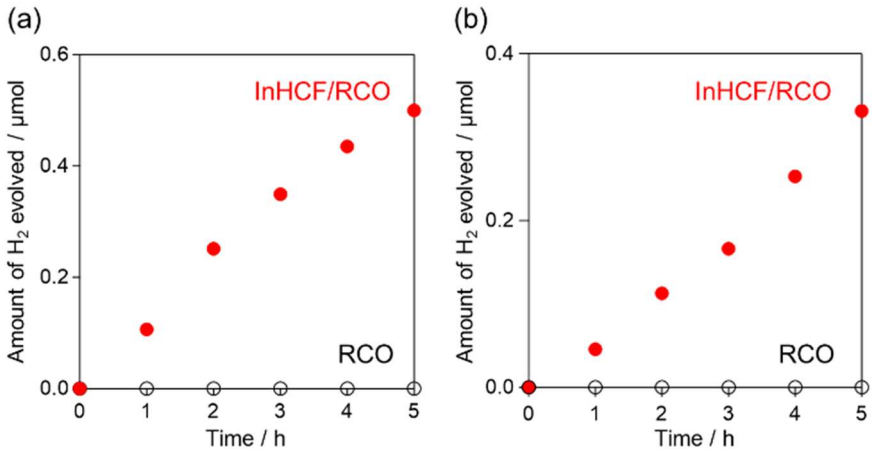

Figure 4-28. Application of the InHCF cocatalyst for various visible-light-responsive photocatalysts: (a) Ta_3N_5 and (b) $Sm_2Ti_2S_2O_5$. Reaction conditions: photocatalyst mass, 0.05 g; solution, aqueous $FeCl_2$ solution (5 mM, 250 mL) at pH 2.5

Table 4-2. Application of the InHCF cocatalyst for $BaTaO_2N$ photocatalyst

Photocatalyst[a]	InHCF modification (10 mol% as Fe)	Amount of H_2[b] / μmol
$BaTaO_2N$	Yes	0.1
	No	< 0.1
$BaTaO_2N$(Flux)	Yes	2.3

[a]All samples were loaded with RCO before modified with InHCF.

[b]After 5 h of irradiation of visible light to an aqueous dispersion of the photocatalyst powder (0.05 g) in the presence of the Fe^{2+} electron donor (5 mM).

[c]'n.d.' means 'not detected'.

4.3.6. Z-scheme Water Splitting using InHCF/RCO/TaON as an H_2 Evolution Photocatalyst.

Finally, InHCF/RCO/TaON was employed as an H_2 evolution photocatalyst in Z-scheme water splitting using an Fe^{3+}/Fe^{2+} redox mediator in combination with $BiVO_4$[38] or surface-treated WO_3[12] as the O_2 evolution photocatalyst. As shown in Figure 4-29a, the combination with $BiVO_4$, which has been extensively employed in Z-scheme water splitting with Fe^{3+}/Fe^{2+}, afforded simultaneous evolution of H_2 and O_2 under visible light. The amount of evolved H_2 was more than twice that of O_2 in the initial stages of illumination, because the reactions were initiated by the presence of Fe^{2+} only. After the evacuation of the gas phase, the rates of H_2 and O_2 evolution eventually approached a near-stoichiometric ratio (2:1). The total amount of H_2 produced after 35 h

of operation (887 μmol) was greater than the amount of Fe^{2+} present (500 μmol). The turnover number of the reacted electrons per mole of Fe^{2+} was calculated to be 3.5, indicating that the overall water splitting proceeds via the Fe^{3+}/Fe^{2+} redox relay. Although the combination of conventional STO:Rh and $BiVO_4$ has been demonstrated to generate H_2 and O_2 even without any redox mediators in solution, through the interparticle electron transfer,[60] the present combination did exhibit negligibly low activity in the absence of Fe^{3+}/Fe^{2+} (Figure 4-29a, open triangles). The combination with the surface-treated WO_3 also provided simultaneous generation of H_2 and O_2 (Figure 4-29b), while the initial rates were higher compared to the case of $BiVO_4$. Note that the gas evolution was negligible when the RCO/TaON sample without InHCF was employed (Figure 4-29b, open triangles), confirming that modification with InHCF as a cocatalyst for Fe^{2+} oxidation is essential for achieving Z-scheme water splitting using an Fe^{3+}/Fe^{2+} redox mediator. Water splitting using the above combination also proceeded under simulated sunlight irradiation (AM1.5G) (see Figure 4-30), with an STH conversion efficiency of 0.05%. This value is comparable to that of the combination of $SrTiO_3$:Rh and $BiVO_4$ (0.07–0.1%).[61,62]

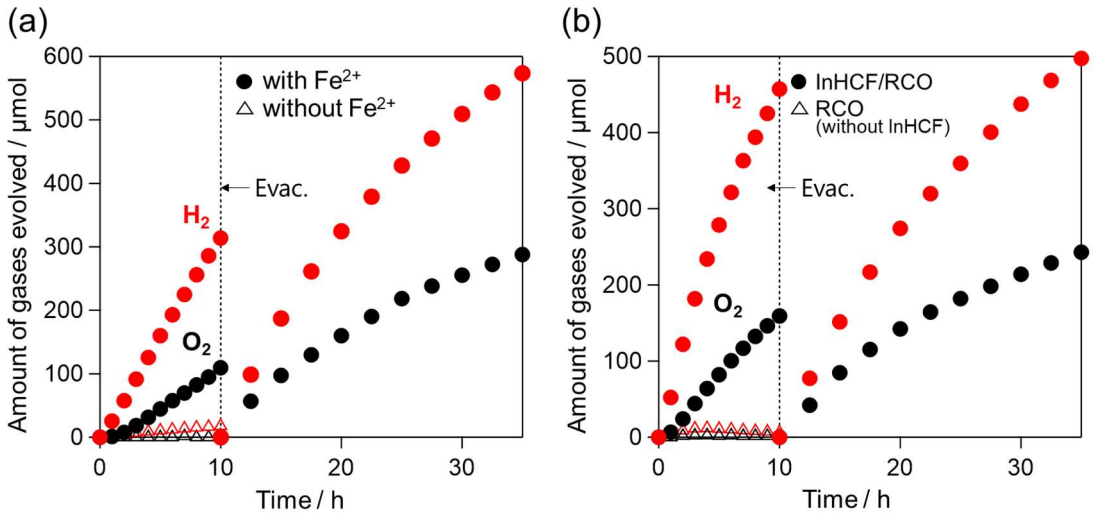

Figure 4-29. Water splitting activities of systems comprising (a) InHCF/RCO/TaON and $BiVO_4$ in aqueous solution (250 mL, pH 2.5) with $FeCl_2$ (2 mM, filled circle) and without $FeCl_2$ (open triangle), and (b) InHCF/RCO/TaON (filled circle) or RCO/TaON (open triangle) as an H_2 evolution photocatalyst, and surface-treated WO_3 as an O_2 evolution photocatalyst in aqueous $FeCl_2$ solution (2 mM, 250 mL, pH 2.5) under visible light irradiation.

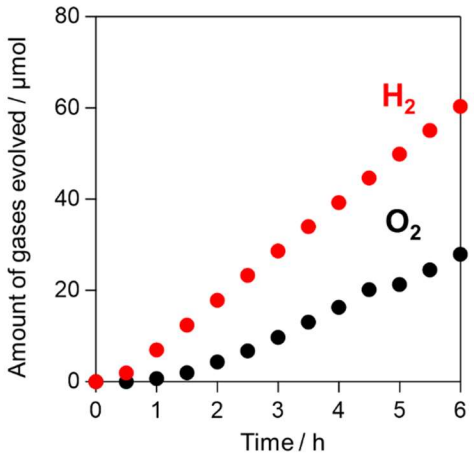

Figure 4-30. Time courses of water splitting over InHCF/RCO/TaON (0.05 g) and surface-treated WO_3 (0.05 g) in aqueous $FeCl_2$ solution (2 mM, 100 mL) at pH 2.5 under the simulated sunlight irradiation (AM 1.5G, 100 mW cm^{-2}).

4.4. Conclusion

In summary, we successfully activated TaON to deliver an efficient H_2 evolution photocatalyst for Z-scheme water splitting using Fe^{3+}/Fe^{2+} couples. Although TaON has so far been inactive for H_2 evolution in the presence of an Fe^{2+} electron donor due to the lack of Fe^{2+}oxidation sites, simple surface modification with indium hexacyanoferrate (InHCF) and Rh-Cr mixed oxide (RCO) enabled the efficient production of H_2 by the TaON photocatalyst in the presence of an Fe^{3+}/Fe^{2+} redox mediator. The vital roles of InHCF and RCO were experimentally determined to entail the promotion of Fe^{2+} oxidation via Fe^{III}/Fe^{II} redox cycles in the structure, and promotion of the water reduction without being hindered by the unfavorable reduction of Fe^{3+} to Fe^{2+}.

The present study achieved two important advancements. First is enhanced oxidation of the redox mediator, shown to be instrumental in achieving efficient Z-scheme water splitting, which has not been examined systematically to date.[30,31,37] This strategy indeed overcome the longstanding limitation in Z-scheme water splitting with an Fe^{3+}/Fe^{2+}, i.e., the rhodium-doped $SrTiO_3$ has been almost only the choice as the efficient H_2-evolution photocatalyst. The elucidation and harnessing of such oxidation processes will widen the selection of H_2 evolution photocatalysts with narrow bandgaps, such as Ta_3N_5, $Sm_2Ti_2S_2O_5$ and $BaTaO_2N$, thereby contributing to the development of highly efficient Z-scheme water splitting systems. The second is the utilization of MHCFs as cocatalysts. This highly diverse family of coordination polymers allows for the precise control of their physicochemical properties to customize them for targeted

reactions. As demonstrated in various research fields,[24,25,28,29,31,63–65] critical MHCF properties, such as catalytic activity and redox potential, can be modified by varying the metal cation or ligand, enabling the development of more effective cocatalysts capable of enhancing each reaction involved in Z-scheme water splitting.

References

1. Kudo, A.; Miseki, Y. *Chem. Soc. Rev.* **2009**, *38*, 253–278.
2. Abe, R. *Bull. Chem. Soc. Jpn.* **2011**, *84*, 1000–1030.
3. Pinaud, B. A.; Benck, J. D.; Seitz, L. C.; Forman, A. J.; Chen, Z.; Deutsch, T. G.; James, B. D.; Baum, K. N.; Baum, G. N.; Ardo, S.; Wang, H.; Millere, E.; Jaramillo, T. F. *Energy Environ. Sci.* **2013**, *6*, 1983–2002.
4. Shaner, M. R.; Atwater, H. A.; Lewis, N. S.; McFarland, E. W. *Energy Environ. Sci.* **2016**, *9*, 2354–2371.
5. Wang, Q.; Domen, K. Chem. Rev. **2020**, *120*, 919–985.
6. Maeda, K.; Teramura, K.; Lu, D.; Takata, T.; Saito, N.; Inoue, Y.; Domen, K. *Nature* **2006**, *440*, 440295.
7. Maeda, K.; Lu, D.; Domen, K. *Chem. - A Eur. J.* **2013**, *19*, 4986–4991.
8. Asai, R.; Nemoto, H.; Jia, Q.; Saito, K.; Iwase, A.; Kudo, A. A *Chem. Commun.* **2014**, *50*, 2543–2546.
9. Wang, Q.; Nakabayashi, M.; Hisatomi, T.; Sun, S.; Akiyama, S.; Wang, Z.; Pan, Z.; Xiao, X.; Watanabe, T.; Yamada, T.; et al. Nat. Mater. 2019, 18, 827–832.
10. Kudo, A. *MRS Bull.* **2011**, *36*, 32–38.
11. Wang, Y.; Suzuki, H.; Xie, J.; Tomita, O.; Martin, D. J.; Higashi, M.; Kong, D.; Abe, R.; Tang, J. *Chem. Rev.* **2018**, *118*, 5201–5241.
12. Miseki, Y.; Kusama, H.; Sugihara, H.; Sayama, K. *J. Phys. Chem. Lett.* **2010**, *1*, 1196–1200.
13. Nakada, A.; Suzuki, H.; Jhon, J.; Vequizo, M.; Ogawa, K.; Higashi, M.; Saeki, A.; Yamakata, A.; Kageyama, H.; Abe, R. *ACS Appl. Mater. Interfaces* **2019**, *11*, 45606–45611.
14. Kato, H.; Hori, M.; Konta, R.; Shimodaira, Y.; Kudo, A. *Chem. Lett.* **2004**, *33*, 1348–1349.
15. Konta, R.; Ishii, T.; Kato, H.; Kudo, A. *J. Phys. Chem. B* **2004**, *108*, 8992–8995.
16. Suzuki, H.; Tomita, O.; Higashi, M.; Abe, R. *Chem. Lett.* **2015**, *44*, 1134–1136.
17. Suzuki, H.; Tomita, O.; Higashi, M.; Abe, R. *J. Mater. Chem. A* **2017**, *5*, 10280–10288.
18. Nakada, A.; Nishioka, S.; Vequizo, J. J. M.; Muraoka, K.; Kanazawa, T.; Yamakata, A.; Nozawa, S.; Kumagai, H.; Adachi, S.; Ishitani, O.; et al. Solar-Driven Z-Scheme Water Splitting Using Tantalum/Nitrogen Co-Doped Rutile Titania Nanorod as an Oxygen Evolution Photocatalyst. *J. Mater. Chem. A* **2017**, *5*, 11710–11719.
19. Fujito, H.; Kunioku, H.; Kato, D.; Suzuki, H.; Higashi, M.; Kageyama, H.; Abe, R. *J. Am. Chem. Soc.* **2016**, *138*, 2082–2085.
20. De Tacconi, N. R.; Rajeshwar, K.; Lezna, R. O. *Chem. Mater.* **2003**, *15*, 3046–3062.
21. DeLongchamp., D. M.; Hammond, P. T. *Adv. Funct. Mater.* **2004**, *14*, 224–232.
22. Kholoud, E.; Watanabe, H.; Takahashi, A.; Emara, M. M.; Abd-El-Nabey, B. A.; Kurihara,

M.; Tajima, K.; Kawamoto, T. *J. Mater. Chem. C* **2017**, *5*, 8921–8926.
23. Kitajima, A.; Tanaka, H.; Minami, N.; Yoshino, K.; Kawamoto, T.; Kitajima, A.; Minami, N.; Kawamoto, T.; Tanaka, H. *Chem. Lett.* **2012**, *41*, 1473–1474.
24. Takahashi, A.; Tanaka, H.; Parajuli, D.; Nakamura, T.; Minami, K.; Sugiyama, Y.; Hakuta, Y.; Ohkoshi, S. I.; Kawamoto, T. *J. Am. Chem. Soc.* **2016**, *138*, 6376–6379.
25. Lu, Y.; Wang, L.; Cheng, J.; Goodenough, J. B. *Chem. Commun.* **2012**, *48*, 6544–6546.
26. Hurlbutt, K.; Wheeler, S.; Capone, I.; Pasta, M. *Joule* **2018**, *2*, 1950–1960.
27. Goberna-Ferrón, S.; Hernández, W. Y.; Rodríguez-García, B.; Galán-Mascarós, J. R. *ACS Catal.* **2014**, *4*, 1637–1641.
28. Yamada, Y.; Oyama, K.; Gates, R.; Fukuzumi, S. *Angew. Chemie - Int. Ed.* **2015**, *54*, 5613–5617.
29. Tabe, H.; Terashima, C.; Yamada, Y. *Catal. Sci. Technol.* **2018**, *8*, 4747–4756.
30. Shirakawa, T.; Higashi, M.; Tomita, O.; Abe, R. *Sustain. Energy Fuels* **2017**, *1*, 1065–1073.
31. Matsuoka, H.; Higashi, M.; Nakada, A.; Tomita, O.; Abe, R. *Chem. Lett.* **2018**, *47*, 941–944.
32. Maeda, K.; Higashi, M.; Lu, D.; Abe, R.; Domen, K.; Higash, M.; Lu, D.; Abe, R.; Domen, K. *J. Am. Chem. Soc.* **2010**, *132*, 5858–5868.
33. Maeda, K.; Terashima, H.; Kase, K.; Higashi, M.; Tabata, M.; Domen, K. *Bull. Chem. Soc. Jpn.* **2008**, *81*, 927–937.
34. Higashi, M.; Abe, R.; Teramura, K.; Takata, T.; Ohtani, B.; Domen, K. *Chem. Phys. Lett.* **2008**, *452*, 120–123.
35. Wang, Z.; Luo, Y.; Hisatomi, T.; Vequizo, J. J. M.; Suzuki, S.; Chen, S.; Nakabayashi, M.; Lin, L.; Pan, Z.; Kariya, N.; Yamakata, A.; Shibata, N.; Takata, T.; Teshima, K.; Domen, K. *Nat. Commun.* **2021**, *12*, 1005.
36. Hitoki, G.; Ishikawa, A.; Takata, T.; Kondo, J. N.; Hara, M.; Domen, K. *Chem. Lett.* **2002**, *31*, 736–737.
37. Ma, G.; Chen, S.; Kuang, Y.; Akiyama, S.; Hisatomi, T.; Nakabayashi, M.; Shibata, N.; Katayama, M.; Minegishi, T.; Domen, K. *J. Phys. Chem. Lett.* **2016**, *7*, 3892–3896.
38. Iwase, A.; Kato, H.; Kudo, A. *J. Sol. Energy Eng.* **2010**, *132*, 021106.
39. Miseki, Y.; Sayama, K. *Catal. Sci. Technol.* **2019**, *9*, 2019–2024.
40. Gotoh, A.; Uchida, H.; Ishizaki, M.; Satoh, T.; Kaga, S.; Okamoto, S.; Ohta, M.; Sakamoto, M.; Kawamoto, T.; Tanaka, H.; Tokumoto, M.; Hara, S.; Shiozaki, H.; Yamada, M.; Miyake, M.; Kurihara, M. *Nanotechnology* **2007**, *18*, 1–6.
41. Momma, K.; Izumi, F. *J. Appl. Crystallogr.* **2011**, *44*, 1272–1276.
42. Krishnamurti, G. S. R.; Huang, P. M. *Talanta* 1990, *37*, 745–748.
43. Tomita, O.; Nitta, S.; Matsuta, Y.; Hosokawa, S.; Higashi, M.; Abe, R. *Chem. Lett.* **2017**, *46*,

221–224.

44. Chen, L.; Shao, H.; Zhou, X.; Liu, G.; Jiang, J.; Liu, Z. *Nat. Commun.* 2016, *7*, 11982.
45. Kiener, J.; Limousy, L.; Jeguirim, M.; Meins, J. M. Le; Hajjar-Garreau, S.; Bigoin, G.; Ghimbeu, C. M. *Materials* **2019**, *12*, 1–17.
46. Kulesza, P. J.; Faszynska, M. *J. Electroanal. Chem.* **1988**, *252*, 461–466.
47. Jin, Z.; Dong, S. *Electrochim. Acta* **1990**, *35*, 1057–1060.
48. Chun, W. J.; Ishikawa, A.; Fujisawa, H.; Takata, T.; Kondo, J. N.; Hara, M.; Kawai, M.; Matsumoto, Y.; Domen, K. *J. Phys. Chem. B* **2003**, *107*, 1798–1803.
49. Trasatti, S. *J. Electroanal. Chem.* **1972**, *39*, 163–184.
50. Wang, Y.; Wang, Y.; Xu, R. *J. Phys. Chem. C* **2013**, *117*, 783–790.
51. Abe, R.; Sayama, K.; Arakawa, H. *J. Photochem. Photobiol. A Chem.* **2004**, *166*, 115–122.
52. Maeda, K.; Teramura, K.; Masuda, H.; Takata, T.; Saito, N.; Inoue, Y.; Domen, K. *J. Phys. Chem. B* **2006**, *110*, 13107–13112.
53. Maeda, K.; Lu, D.; Teramura, K.; Domen, K. *Energy Environ. Sci.* **2010**, *3*, 471–478.
54. Chiang, T. H.; Lyu, H.; Hisatomi, T.; Goto, Y.; Takata, T.; Katayama, M.; Minegishi, T.; Domen, K. *ACS Catal.* **2018**, *8*, 2782−2788.
55. Liao, J.; Hu, Q.; Yu, Y.; Wang, H.; Tang, Z.; Wen, Z.; Chen, C. *J. Mater. Chem. A* **2017**, *5*, 19017–19024.
56. Cai, D.; Yang, X.; Qu, B.; Wang, T. *Chem. Commun.* **2017**, *53*, 6780–6783.
57. Lee, H.; Kim, Y.-I.; Park, J.-K.; Choi, J. W. *Chem. Commun.* **2012**, *48*, 8416–8418.
58. Zhang, L.; Chen, L.; Zhou, X.; Liu, Z. Adv. Energy Mater. 2015, *5*, 1400930.
59. Xiao, J.; Vequizo, J. J. M.; Hisatomi, T.; Rabeah, J.; Nakabayashi, M.; Wang, Z.; Xiao, Q.; Li, H.; Pan, Z.; Krause, M.;Yin, N.; Smith, G.; Shibata, N.; Brückner, A.; Yamakata, A.; Takata, T.; Domen, K. *J. Am. Chem. Soc.* **2021**, *143*, 10059–10064.
60. Sasaki, Y.; Nemoto, H.; Saito, K.; Kudo, A. *J. Phys. Chem. C* **2009**, *113*, 17536–17542
61. Kato, H.; Sasaki, Y.; Shirakura, N.; Kudo, *J. Mater. Chem. A* **2013**, *1*, 12327–12333.
62. Duong, H. P.; Mashiyama, T.; Kobayashi, M.; Iwase, A.; Kudo, A.; Asakura, Y.; Yin, S.; Kakihana, M.; Kato, H. *Appl. Catal. B Environ.* **2019**, *252*, 222–229.
63. Scholz, F.; Dostal, A. *Angew. Chem., Int. Ed. Engl.* **1995**, *34*, 2685–2687.
64. Aksoy, M.; Nune, S. V. K.; Karadas, F. *Inorg. Chem.* **2016**, 55, 4301–4307.
65. Lee, H. W.; Wang, R. Y.; Pasta, M.; Lee, S. W.; Liu, N.; Cui, Y. *Nat. Commun.* **2014**, *5*, 5280.

Chapter 5

Indium Hexacyanoferrate as a Solid Redox Electron Mediator in Z-scheme Photocatalytic Water Splitting under Visible Light

5.1. Introduction

Some ionic redox couples (e.g., IO_3^-/I^-, Fe^{3+}/Fe^{2+}) have so far been employed as effective electron mediators in the majority of Z-scheme water splitting systems with various combinations of visible-light-responsive photocatalysts.[1–3] Actually, Chapters 1–4 in the present thesis have focused on the construction of Z-scheme systems using ionic redox couples such as $[Fe(CN)_6)]^{3-}/[Fe(CN)_6]^{4-}$ and Fe^{3+}/Fe^{2+}, and their improvements in efficiency. By contrast, solid electron conductors (e.g., carbon compounds,[4,5] Au,[6,7] indium tin oxide[8]) have recently garnered attention as other candidates of electron mediators in Z-schemes water splitting systems. This is basically because they can minimize the occurrence of backward reactions involving ionic redox couples (e.g., the reduction of Fe^{3+} instead of H^+ on H_2 evolution photocatalysts) that lower the efficiency of water splitting. Indeed, some systems using such solid electron mediators exhibited the remarkably higher solar-to-hydrogen conversion efficiencies (about 1%).[5,6] Moreover, such all-solid systems are probably favorable in terms of recovery of the photocatalyst and reclamation of clean water.[4] However, it is challenging to tune the fundamental properties of these solid electron mediators such as work function or conductivity.

Given the above, the present author focuses on metal hexacyanoferrates as a new class of solid electron mediators. As introduced in the previous chapters, Prussian blue analogues containing metal hexacyanoferrate ($A_hM_k[Fe(CN)_6]_l \cdot mH_2O$; *h, k, l, m*: composition ratios, A: alkali metal cation, M: (transition) metal cation, denoted as MHCF) are active materials in electrochemical technologies.[9–15] These applications rely on the high stability of the redox cycles of metal cation (e.g., carbon-coordinated Fe^{III}/Fe^{II}) in MHCF without any drastic structural changes.[10] Furthermore, the components in MHCF, i.e., metal cations and ligands, can be substantially substituted, by which their properties such as the redox potential[16] are highly tunable for targeted applications.

In Chapters 1, 2 and 4, it has been revealed that various MHCF species can function as promoters for oxidizing redox species in Z-scheme water splitting via their redox cycles of Fe^{III}/Fe^{II}. In short, the Fe^{II} species in the MHCFs are oxidized to Fe^{III} by the photogenerated holes in photocatalysts, and then the generated Fe^{III} species are reduced back to Fe^{II} by electrons of redox mediators. Given the electrochemical and catalytic properties of MHCFs, one can expect that such MHCF materials also function as electron mediators between two photocatalyst materials. The present study reports the first demonstration of Z-Scheme water splitting system using InHCF nanoparticles as solid electron mediators via their redox cycles of Fe^{III}/Fe^{II}.

5.2. EXPERIMENTAL

5.2.1. Sample preparation.

ZrO_2-modified TaON particles as the model H_2 evolution photocatalysts were synthesized by a previously-reported method[17] with a modification, as described in Chapter 4. As-prepared ZrO_2-modified TaON particles were confirmed to resemble the samples in Chapter 4. Hereafter, ZrO_2-modified TaON will be denoted as TaON for simplicity. Cs-treated WO_3 (Cs-WO_3) as an O_2 evolution photocatalyst for Z-scheme water splitting were prepared according to the previous reports.[18,19] Indium hexacyanoferrate (InHCF) nanoparticles were prepared by a coprecipitation method by referencing the previous report,[20] as described in Chapter 4. As-prepared InHCF particles were quite similar to those seen in Chapter 4.

5.2.2. Surface modification.

$Rh_xCr_{2-x}O_3$ species as a H_2 evolution cocatalyst was loaded on TaON particles by a photodeposition method using $Na_3RhCl_6{\cdot}nH_2O$ and K_2CrO_4 precursors, as described in Chapter 4. The amount of added Rh and Cr precursor was set to be 1wt% and 1.5wt%, respectively. Hereafter, RCO-loaded TaON will be denoted as RCO/TaON. RCO/TaON powder was modified with InHCF nanoparticles through an impregnation method. The loading amount of InHCF was 2 mol% as Fe in InHCF with respect to TaON based on the assumption that the composition of InHCF nanoparticles was $KIn[Fe(CN)_6]$. For a comparison, Cs-WO_3 was also modified with the same amount of InHCF via the same procedure. InHCF-modified samples are denoted as InHCF/RCO/TaON, for example.

5.2.3. Characterization.

The prepared samples were characterized by powder X-ray diffraction (XRD; Mini Flex II, X-ray source; Cu Kα, Rigaku) measurement, and attenuated total reflectance-Fourier transform infrared spectroscopy (ATR-FTIR, ATR; ATR Pro One, JASCO, FT-IR; FT-4200, JASCO) using a diamond prism. ATR-FTIR spectra were recorded against air as background. ζ potentials of InHCF/TaON, TaON and InHCF were measured in aqueous solution using a ζ potential analyzer (Zetasizer Nano ZS, Malvern Instruments). The pH of the solution was adjusted by1 M aqueous HCl and 1M aqueous KOH.

5.2.4. Electrochemical and photoelectrochemical measurements.

InHCF electrode was prepared on a FTO glass by a squeegee method as described in Chapter 4. The coated area and the deposited amount were fixed at approx. 1.5 × 1.5 cm^2 and 0.5 ± 0.3 mg, respectively. Electrochemical measurements were performed in an

aqueous solution of K_2SO_4 (0.1 M, 99.0%; FUJIFILM Wako Pure Chemical Corporation) as an electrolyte under Ar atmosphere using a three-electrode cell. The pH of the electrolyte was adjusted to be 2.5–6.0 by 1 M H_2SO_4, or KOH. The prepared electrode as the working electrode, Pt coil as the counter electrode, Ag/AgCl as the reference electrode were connected to a potentiostat (VersaSTAT 4, AMETEK).

5.2.5. Photocatalytic reaction.

Photocatalytic reactions were conducted in Pyrex side-illuminated reaction vessel connected to a glass closed gas-circulation system. A 300 W Xe lamp was used as a light source in combination with a CM-1 cold mirror and an L-42 cut-off filter for illumination with visible light ($\lambda > 400$ nm). The TaON photocatalyst powder (0.05 g) and the Cs-WO_3 powder (0.05 g) were dispersed in 250 mL of aqueous solution at pH 2.5–6.0 adjusted by HCl or KOH. The suspension was irradiated with visible light after thoroughly degassed and purged with Ar. The evolved gases were analyzed by a gas chromatograph (GC-8A, Shimadzu, TCD detector, MS 5A column, Ar carrier) directly connected to the closed gas-circulation system.

5.3. RESULTS AND DISCUSSION

5.3.1. Z-scheme water splitting with InHCF as a solid redox mediator

Figure 5-1 shows the time courses of H_2 and O_2 evolution over the combinations of a TaON-based photocatalyst and a Cs-treated WO_3 (Cs-WO_3) photocatalyst suspended in an aqueous solution of pH 2.5 adjusted by addition of small amount of HCl. The effect of the InHCF modification on the Z-scheme water splitting activity was evaluated by comparing the results with and without loading of InHCF onto RCO/TaON. The combination of RCO/TaON and Cs-WO_3 exhibited negligible H_2 and O_2 evolution, indicating that interparticle charge transfer did not occur between these photocatalysts. In contrast, the use of InHCF/RCO/TaON instead of RCO/TaON triggered simultaneous H_2 and O_2 evolution in higher and almost steady rates. The turnover number of reacted electrons per mole of InHCF in the combination of InHCF/RCO/TaON and Cs-WO_3 was calculated to be 48 over 20 h, which is higher than that of a typical solid-type Z-scheme water splitting system comprising Ru-loaded $SrTiO_3$ doped with Rh, $BiVO_4$, and reduced graphene oxide (3.2 over 24 h).[4] The characterization of the samples after the reaction (Figure 5-2) confirmed that each photocatalyst and InHCF remained stable. These results indicated that InHCF promoted the electron transfer between RCO/TaON and Cs-WO_3.

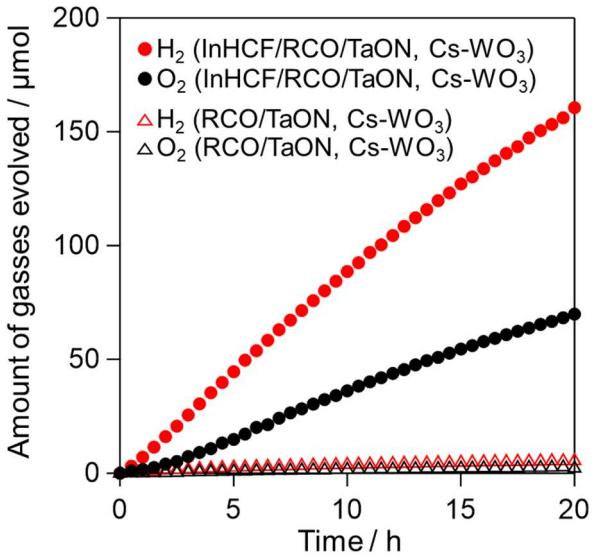

Figure 5-1. Water splitting activities with time of systems comprising InHCF/RCO/TaON (filled circle) or RCO/TaON (open triangle) as an H_2 evolution photocatalyst (0.05 g) and surface-treated WO_3 (0.05 g) as an O_2 evolution photocatalyst in aqueous solution at pH 2.5 under visible light irradiation.

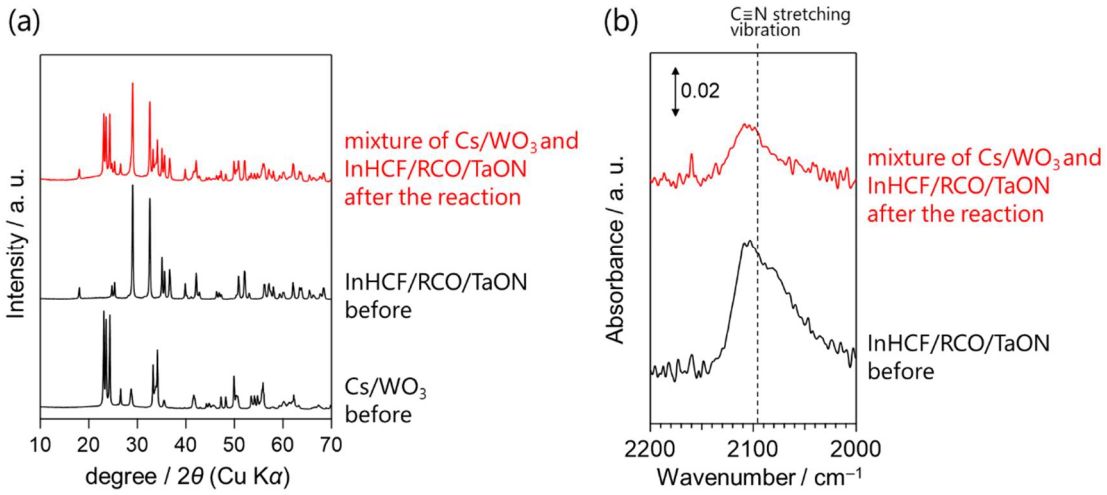

Figure 5-2. (a) XRD patterns and (b) ATR-FTIR spectra of the samples before and after the reaction.

Although a simple addition of InHCF particles into the reaction solution containing RCO/TaON and Cs-WO_3 also resulted in simultaneous evolution of H_2 and O_2, their evolution rates were much lower compared with the case with InHCF-loaded RCO/TaON (Figure 5-3). This finding indicates that the contact of RCO/TaON and InHCF is crucial

for the efficient electron migration, which will be further discussed later. In addition, these results probably rule out the assumption that the redox ion, such as $[Fe(CN)_6]^{4-}$, formed by the decomposition of InHCF, and then acted as a shuttle electron mediator in the reaction solution.

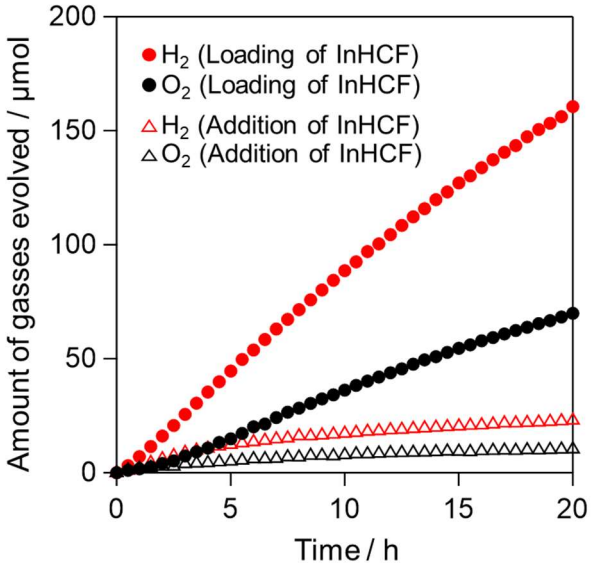

Figure 5-3. The effect of the addition of InHCF into the reaction solution (open triangle) on the water splitting activities over RCO/TaON (0.05 g) and surface-treated WO_3 (0.05 g) in 250 mL of aqueous solution at pH 2.5 under visible light irradiation.

5.3.3. Effect of pH on water splitting activity

It has been demonstrated that the pH value of the reaction solution significantly affects the efficiency of Z-scheme water splitting using solid-state electron mediators.[4,22] Such pH effect has been basically explained by surface charge of each photocatalyst depending on pH.[4,22] Because the increased physical contacts between H_2- and O_2-evolution photocatalyst particles should be advantageous to the electron transfer between them, they must be oppositely charged and form aggregates by electrostatic attraction. This is typified by the result of the combination of Rh-doped $SrTiO_3$ and $BiVO_4$ which exhibited the best performance under the pH conditions (e.g., at pH = 3.5) where their surfaces are oppositely charged (i.e., negative and positive).[4,22] Note that aggregation between solid materials in solutions is often discussed by the ζ potentials of the surface of them.

In the present system, the efficiency of water splitting indeed depended on the pH of the reaction solution. As shown in Figure 5-4, the combination exhibited the evidently higher activity at pH 2.5 or 4.3. It should be noted that the pH value of 4.3 was naturally

established without adjustment by addition of HCl or KOH, i.e., just by adding two particulate photocatalysts into a pure water. This spontaneous acidic pH value is undoubtedly attributed to the surface acidity of WO_3. Figure 5-5 shows the change in ζ potentials of InHCF/RCO/TaON, Cs-WO_3, unmodified TaON, and InHCF depending on pH of the solution. Unexpectedly, both the InHCF/RCO/TaON and Cs-WO_3 photocatalysts were negatively charged at pH values ranging from 2.5 to 4.3 where their combination provided higher efficiency in water splitting. Therefore, it is difficult to the explain the impact of pH on the efficiency by the electrostatic interaction between H_2- and O_2-evolution photocatalysts in the present case. However, it is worth noting that the unmodified TaON particles (i.e., without InHCF) exhibited positive ζ potentials at this pH range (2.5 to 4.3), implying more complicated interaction between these photocatalyst materials after the loading of InHCF. Note that the electrochemical properties such as peak separation and redox potential of Fe^{III}/Fe^{II} in InHCF did not depend on the pH of the solution, as shown in Figure 5-6. Although the origin of the pH dependence is still unclear and should be examined further, the reaction solution was set to be 4.3 (not adjusted) in the following reactions.

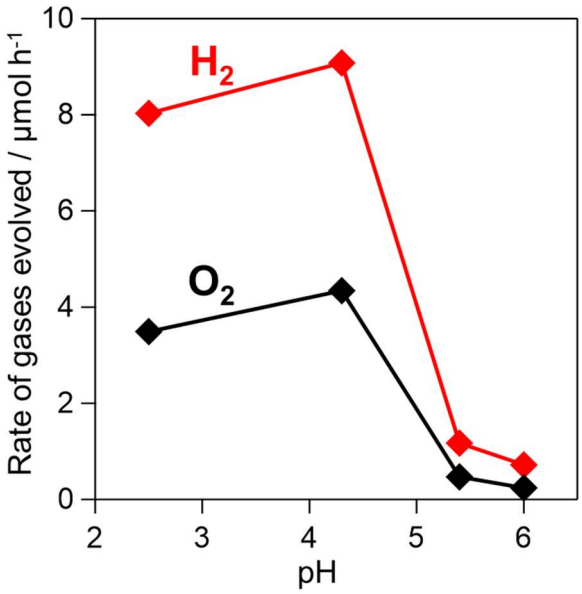

Figure 5-4. Dependence of the pH in the reaction solution on the efficiency of Z-scheme water splitting using InHCF/RCO/TaON and Cs-WO_3 under visible-light irradiation.

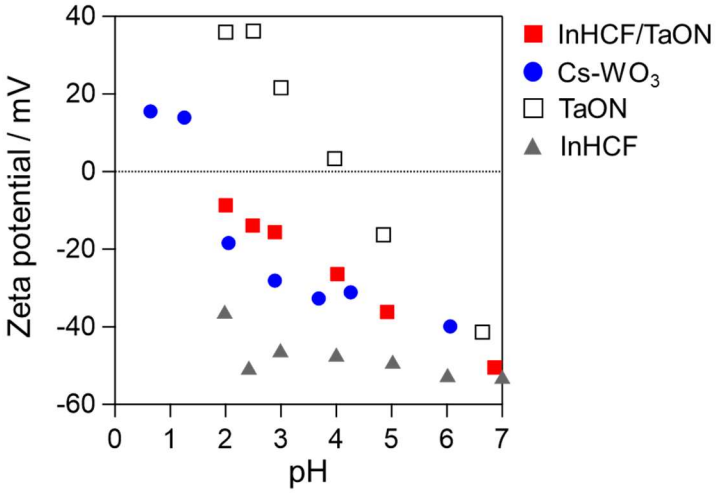

Figure 5-5. ζ potentials of InHCF/TaON, Cs-WO_3, TaON and InHCF at various pH values.

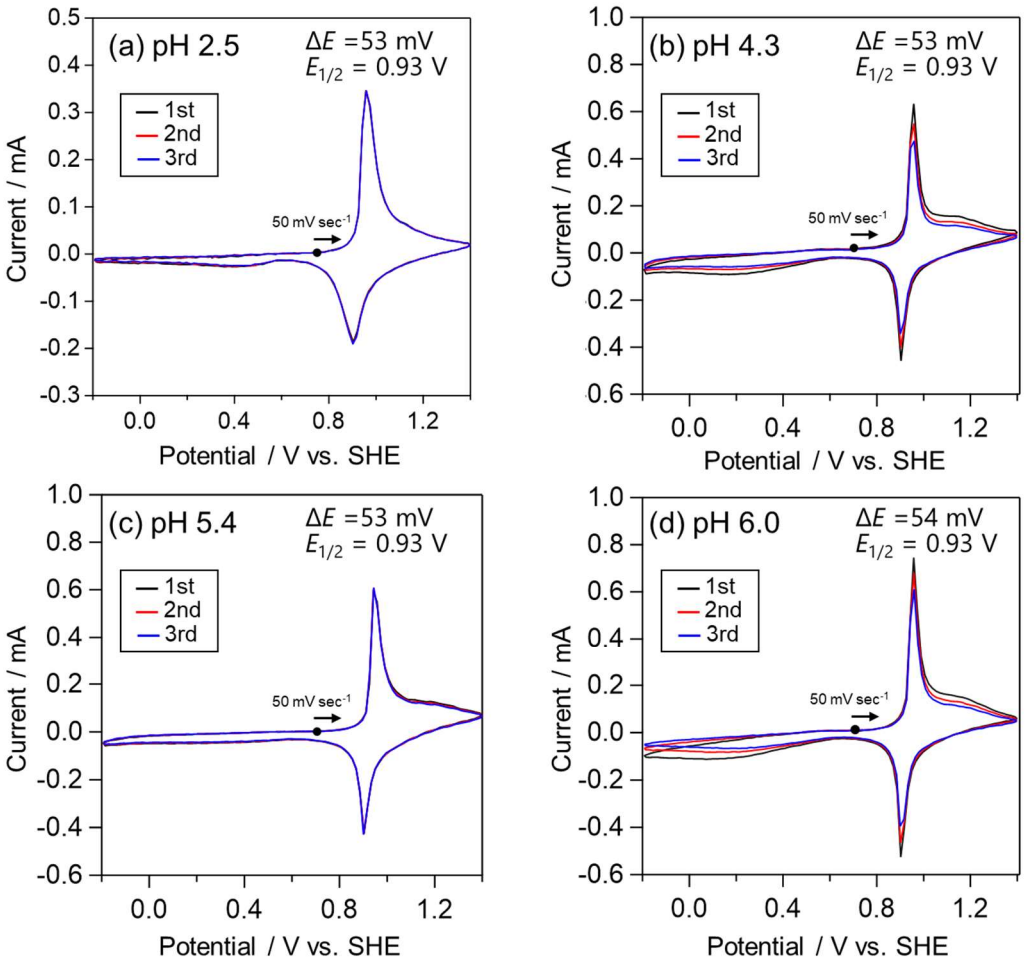

Figure 5-6. CV profiles of InHCF-deposited FTO electrode at a scan rate of 50 mV s^{-1} in aqueous K_2SO_4 solution (0.1 M, 40 mL) at various pH values.

5.3.4. Working mechanism of InHCF as a solid electron mediator

To examine the effective sites to be modified with InHCF for efficient electron transfer, the InHCF particles were deposited on Cs-WO_3 instead of RCO/TaON, and then subjected to Z-scheme reaction. As shown in Figure 5-7, the deposition of InHCF onto Cs-WO_3 resulted in much lower gas evolution rates compared to the case of the deposition onto RCO/TaON, while the rates were obviously higher than those in the absence of InHCF (Figure 5-1). The lower efficiency can be probably explained by the undesirable oxidation of Fe^{II} species in the InHCF by photogenerated holes in Cs-WO_3 instead of water. This finding indicates that the design and/or choice of appropriate sites for InHCF is the key for establishing Z-scheme water splitting systems and further improving the efficiency via the interparticle electron transfer by InHCF particles.

From the above results, the working mechanism of InHCF as an electron mediator in Z-scheme water splitting can be illustrated as Figure 5-8. Photogenerated holes in TaON oxidize Fe^{II} in InHCF to Fe^{III}, and then the produced Fe^{III} is reduced back to Fe^{II} by photoexcited electrons in (Cs-)WO_3. Eventually, the redox cycles of Fe^{III}/Fe^{II} in InHCF mediate the forward electron transfer between RCO/TaON and Cs-WO_3. Meanwhile, photoexcited electrons left in RCO/TaON can reduce proton (or water) to H_2, while photogenerated holes in Cs-WO_3 can oxidize water to O_2, realizing the Z-scheme water splitting without any ionic redox mediators in the solution.

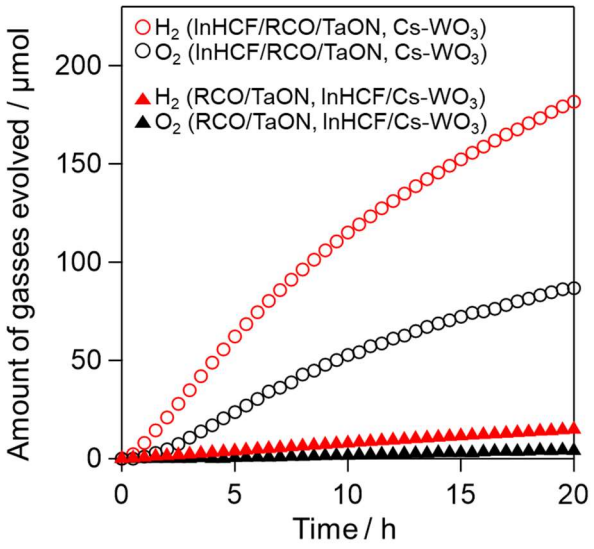

Figure 5-7. Water splitting activities with time of systems comprising RCO/TaON and InHCF/Cs-WO_3(filled triangle) or InHCF/RCO/TaON and Cs-WO_3 (open circle) in aqueous solution at pH 4.3 (not adjusted) under visible light irradiation.

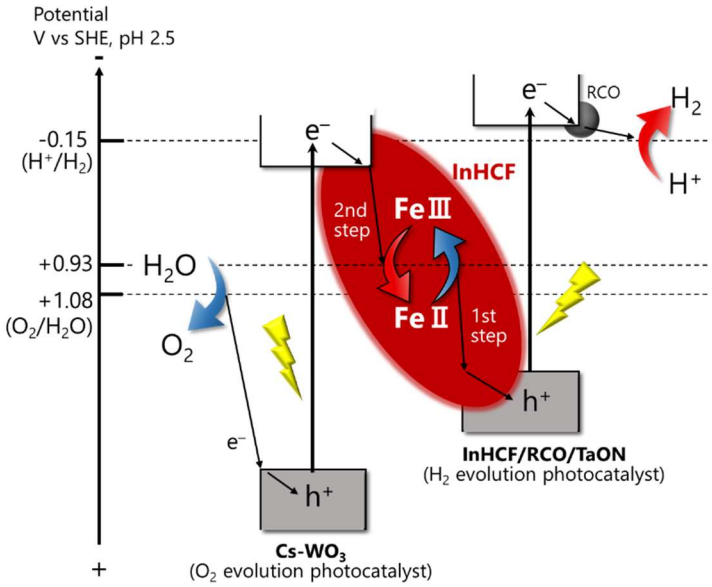

Figure 5-8. Schematic illustration of InHCF as an electron mediator between O_2- and H_2 -evolution photocatalysts in Z-scheme water splitting.

Conclusion

Indium hexacyanoferrate (InHCF) was demonstrated for the first time to function as a solid electron mediator in a Z-scheme water splitting system under visible light. The combination of InHCF/RCO/TaON and Cs-WO_3, as the H_2- and O_2-evolution photocatalyst, respectively, provided simultaneous and stable H_2 and O_2 evolution under visible light. The experimental results indicated that the water splitting relied on the electron transfer between H_2- and O_2-evolution photocatalysts via the redox cycles of Fe^{III}/Fe^{II} in InHCF. The present study highlights the potential of metal hexacyanoferrate (MHCF) family with high tunability as a new class of solid electron mediators for Z-scheme water splitting systems, implying the possibility of fabricating photocatalyst sheets comprising H_2 evolution photocatalyst, an O_2 evolution photocatalyst, and a MHCF to realize the higher water splitting efficiency in the near future.

References

1. Sayama, K.; Mukasa, K.; Abe, R.; Abe, Y.; Arakawa, H. *Chem. Commun.* **2001**, *23*, 2416–2417.
2. Kato, H.; Hori, M.; Konta, R.; Shimodaira, Y.; Kudo, A. *Chem. Lett.* **2004**, *33*, 1348–1349.
3. Wang, Y.; Suzuki, H.; Xie, J.; Tomita, O.; Martin, D. J.; Higashi, M.; Kong, D.; Abe, R.; Tang, J. *Chem. Rev.* **2018**, *118*, 5201–5241.
4. Iwase, A.; Ng, Y. H.; Ishiguro, Y.; Kudo, A.; Amal, R. *J. Am. Chem. Soc.* **2011**, *133*, 11054–11057.
5. Wang, Q.; Hisatomi, T.; Suzuki, Y.; Pan, Z.; Seo, J.; Katayama, M.; Minegishi, T.; Nishiyama, H.; Takata, T.; Seki, K.; Kudo, A.; Yamada, T.; Domen, K. *J. Am. Chem. Soc.* **2017**, *139*, 1675–1683.
6. Wang, Q.; Hisatomi, T.; Jia, Q.; Tokudome, H.; Zhong, M.; Wang, C.; Pan, Z.; Takata, T.; Nakabayashi, M.; Shibata, N.; Li, Y.; Sharp, I. D.; Kudo, A.; Yamada, T.; Domen, K. *Nat. Mater.* **2016**, *15*, 611–613.
7. Wang, Q.; Hisatomi, T.; Katayama, M.; Takata, T.; Minegishi, T.; Kudo, A.; Yamada, T.; Domen, K. *Faraday Discuss.* **2017**, *197*, 491–504.
8. Wang, Q.; Okunaka, S.; Tokudome, H.; Hisatomi, T.; Nakabayashi, M.; Shibata, N.; Yamada, T.; Domen, K. *Joule* **2018**, *2*, 2667–2680.
9. Lu, Y.; Wang, L.; Cheng, J.; Goodenough, J. B. *Chem. Commun.* **2012**, *48*, 6544–6546.
10. Hurlbutt, K.; Wheeler, S.; Capone, I.; Pasta, M. *Joule* **2018**, *2*, 1950–1960.
11. DeLongchamp., D. M.; Hammond, P. T. *Adv. Funct. Mater.* **2004**, *14*, 224–232.
12. Kholoud, E.; Watanabe, H.; Takahashi, A.; Emara, M. M.; Abd-El-Nabey, B. A.; Kurihara, M.; Tajima, K.; Kawamoto, T. *J. Mater. Chem. C* **2017**, *5*, 8921–8926.
13. Goberna-Ferrón, S.; Hernández, W. Y.; Rodríguez-García, B.; Galán-Mascarós, J. R. *ACS Catal.* **2014**, *4*, 1637–1641.
14. Yamada, Y.; Oyama, K.; Gates, R.; Fukuzumi, S. *Angew. Chemie - Int. Ed.* **2015**, *54*, 5613–5617.
15. Tabe, H.; Terashima, C.; Yamada, Y. *Catal. Sci. Technol.* **2018**, *8*, 4747–4756.
16. Scholz, F.; Dostal, A. *Angew. Chem., Int. Ed. Engl.* **1995**, *34*, 2685–2687.
17. Maeda, K.; Terashima, H.; Kase, K.; Higashi, M.; Tabata, M.; Domen, K. *Bull. Chem. Soc. Jpn.* **2008**, *81*, 927–937.
18. Miseki, Y.; Kusama, H.; Sugihara, H.; Sayama, K. *J. Phys. Chem. Lett.* **2010**, *1*, 1196–1200.
19. Miseki, Y.; Sayama, K. *Catal. Sci. Technol.* **2019**, *9*, 2019–2024.
20. Gotoh, A.; Uchida, H.; Ishizaki, M.; Satoh, T.; Kaga, S.; Okamoto, S.; Ohta, M.; Sakamoto, M.; Kawamoto, T.; Tanaka, H.; Tokumoto, M.; Hara, S.; Shiozaki, H.; Yamada, M.; Miyake, M.; Kurihara, M. *Nanotechnology* **2007**, *18*, 1–6.
21. Sasaki, Y.; Nemoto, H.; Saito, K.; Kudo, A. *J. Phys. Chem. C* **2009**, *113*, 17536–17542.

General Conclusion

This thesis focused on the application of metal hexacyanoferrates (MHCFs) to promoters of surface redox reactions, such as oxidation cocatalysts and solid redox electron mediators, to improve the efficiency of photocatalytic water splitting under visible light.

In Chapter 1, the author prepared and examined a series of MHCFs as promoters of the oxidation of $[Fe(CN)_6]^{4-}$ as an electron donor on the metal sulfide photocatalyst ($ZnIn_2S_4$). It was revealed that various MHCFs (M = Mn, In, Fe, Co, Ni or Zn) functioned as promoters of the $[Fe(CN)_6]^{4-}$ oxidation, thereby inducing the higher H_2 evolution rate. By contrast, AgHCF and CuHCF did not enhance the activity. The results on electrochemical measurements and the photocatalytic reactions clarified that the stable redox cycles of Fe^{III}/Fe^{II} in MHCFs (or Co^{III}/Co^{II} in CoHCF) with the redox potential located between the valence band maxima of photocatalysts and the redox potential of $[Fe(CN)_6]^{3-}/[Fe(CN)_6]^{4-}$ are crucial for realizing efficient H_2 evolution. In addition, the results suggested the effect of the peak separation in cyclic voltammograms of the redox couples in MHCFs and particle size (or specific surface area) on H_2 evolution activities.

In Chapter 2, the author developed the stepwise method of MHCF modification based on the effect of particle size in Chapter 1. The stepwise method allowed for the formation of thinner layers of zinc or cadmium hexacyanoferrate (ZnHCF or CdHCF) compared with the conventional impregnation method using ZnHCF or CdHCF particles. The thinner layers can captures the photogenerated holes in $ZnIn_2S_4$ and oxidize $[Fe(CN)_6]^{4-}$ electron donor more effectively, thereby inducing the higher H_2 evolution rate on $ZnIn_2S_4$.

In Chapter 3, the author revealed that cobalt hexacyanoferrate (CoHCF) functioned as promoters of O_2 evolution on the visible-light-responsive oxynitride (TaON) photocatalyst powder in the basic (pH 8) aqueous solution containing Ag^+ as the irreversible electron acceptor. It was also demonstrated that CoHCF cocatalysts promoted O_2 evolution under the acidic conditions (pH 3), where conventional cobalt-based materials (e.g., $CoO_x(OH)_y$) cannot due to their dissolution. In addition, CoHCF promoted the O_2 evolution even in the presence of the Fe^{3+} reversible electron acceptor which operates only under the acidic condition (at pH below 2.5).

In Chapter 4, the author demonstrated that co-modification with indium hexacyanoferrate (InHCF) and Rh-Cr mixed oxide (RCO) activated TaON, which has so far been regarded as inactive for H_2 evolution in the presence of Fe^{2+}, but not with RCO alone. The roles of InHCF and RCO were experimentally determined to be the promotion of Fe^{2+} oxidation via Fe^{III}/Fe^{II} redox cycles in InHCF, and promotion of the water reduction without being hindered by unfavorable reduction of Fe^{3+} to Fe^{2+}, respectively. Eventually, InHCF modification enabled the Z-scheme water splitting system comprising

TaON, Fe^{3+}/Fe^{2+}, and conventional O_2 evolution photocatalysts. Moreover, InHCF modification also enhanced the activities of H_2 evolution photocatalysts with narrow bandgaps, such as Ta_3N_5, $Sm_2Ti_2S_2O_5$ and $BaTaO_2N$. Because other MHCFs (ZnHCF or FeHCF) also promoted H_2 evolution, the development of more effective cocatalysts is expected via tuning of MHCF properties by varying the metal cation or ligand.

In Chapter 5, the author succeeded in establishing the Z-scheme water splitting system using InHCFs as solid electron mediators under visible light for the first time. Although the combination of the H_2 evolution photocatalyst (RCO/TaON) and the O_2 evolution photocatalyst (Cs-WO_3) without InHCF exhibited negligible gas evolution, that of InHCF-modified RCO/TaON and Cs-WO_3 did simultaneous and stable H_2 and O_2 evolution. Some control experiments revealed that the redox cycles of Fe^{III}/Fe^{II} in InHCFs on H_2 evolution photocatalysts mediated the forward electron transfer between H_2- and O_2-evolution photocatalysts, realizing the Z-scheme water splitting.

In this thesis, the author expanded the applicability of MHCFs towards efficient photocatalytic water splitting systems. As demonstrated by surface modification with MHCFs in Chapters 1, 2 and 4, improving the oxidation process of redox mediators, which has not been examined significantly, will provide an effective strategy for promoting H_2 evolution in Z-scheme water splitting systems. Notably, the promotion of redox mediator oxidation by MHCFs is instrumental in activating H_2 evolution photocatalysts which have been inactive owing to the lack of oxidation sites, thereby widening the photocatalyst choice for Z-scheme water splitting systems. In addition, metal cation or ligand substitution of MHCFs will be a promising way for further improving H_2 evolution.

The superior performance of CoHCF for promoting the photocatalytic water oxidation under acidic conditions will lead to the construction of efficient Z-scheme water splitting systems using Fe^{3+}/Fe^{2+} or polyoxometalate anion as well as CO_2 reduction systems which basically operate under weak acidic conditions (at pH = 2–5).

The application of MHCFs containing InHCF as solid electron mediators will provide significant possibility for establishing Z-scheme water splitting systems using various photocatalyst combinations by appropriately designing their properties such as redox potential and conductivity via metal cation or ligand substitution.

Finally, the author sincerely hopes that the results described in this thesis will offer useful information and open a way to apply MHCFs as reaction promoters and establish highly efficient photocatalytic water splitting systems.

List of Publications

1. Hikaru Matsuoka, Masanobu Higashi, Akinobu Nakada, Hajime Suzuki, Osamu Tomita, Ryu Abe
   "Metal Hexacyanoferrates as Oxidation Promoters for Realizing Efficient Photocatalytic Hydrogen Evolution on Metal Sulfide under Visible Light"
   To be submitted

2. Hikaru Matsuoka, Masanobu Higashi, Akinobu Nakada, Osamu Tomita, Ryu Abe
   "Enhanced H_2 Evolution on $ZnIn_2S_4$ Photocatalyst under Visible Light by Surface Modification with Metal Cyanoferrates"
   Chem. Lett. **2018**, *47*, 941–944

3. Hikaru Matsuoka, Osamu Tomita, Hiroyasu Tabe, Hajime Suzuki, Yusuke Yamada, Ryu Abe
   "Cobalt hexacyanoferrate as an effective cocatalyst boosting water oxidation on oxynitride TaON photocatalyst under visible light"
   J. Photochem. Photobiol. A: Chem. **2022**, *426*, 113753

4. Hikaru Matsuoka, Hajime Suzuki, Osamu Tomita, Shunsuke Nozawa, Ryota Sakamoto, Ryu Abe
   "Indium Hexacyanoferrate Overcomes a Limitation in Z-scheme Water Splitting with an Fe^{3+}/Fe^{2+} Redox Mediator: Activating Photocatalysts by Boosting Redox Mediator Oxidation"
   Submitted to Chemical Science

   Hikaru Matsuoka, Hajime Suzuki, Ryu Abe
   Japanese Patent 2021-117451, 2021
   Submitted

5. Hikaru Matsuoka, Tomoki Inoue, Hajime Suzuki, Osamu Tomita, Ryu Abe
   "Indium Hexacyanoferrate as a Solid Redox Electron Mediator in Z-scheme Photocatalytic Water Splitting under Visible Light"
   To be submitted

Paper not included in this thesis

1. Yosuke Kageshima, Yui Gomyo, Hikaru Matsuoka, Hiroto Inuzuka, Hajime Suzuki, Ryu Abe, Katsuya Teshima, Kazunari Domen, Hiromasa Nishikiori
   "Z-Scheme Overall Water Splitting Using $Zn_xCd_{1-x}Se$ Particles Coated with Metal Cyanoferrates as Hydrogen Evolution Photocatalysts"
   ACS Catal. **2021**, *11*, 8004−8014

Acknowledgements

The present thesis summarizes the author's studies carried out during 2016–2022 at Department of Energy and Hydrocarbon Chemistry, Graduate School of Engineering, Kyoto University.

First of all, the author wishes to express the author's deepest gratitude to Professor Ryu Abe for his invaluable guidance, fruitful discussions, worthy suggestions, continuing support, wonderful opportunities, and hearty encouragement throughout the author's work. The author would like to express his gratitude to Professor Takeshi Abe (Kyoto University) and Professor Tetsuo Sakka (Kyoto University) for their valuable, constructive, and careful comments on this thesis.

The author is deeply grateful to Professor Ryota Sakamoto (Tohoku University) for his helpful discussions and heartwarming encouragement. Sincere gratitude is also expressed to Associate Professor Masanobu Higashi (Osaka City University), Assistant Professor Osamu Tomita (Kyoto University), Assistant Professor Akinobu Nakada (Chuo University), and Assistant Professor Hajime Suzuki (Kyoto University) for their valuable discussions, directional guidance, and hearty encouragement.

The author would like to thank Professor Yusuke Yamada (Osaka City University) and Lecturer Hiroyasu Tabe (Kyoto University) for their excellent collaboration and valuable discussions about metal hexacyanoferrate/Prussian blue analogue especially in Chapter 3. Gratitude is also expressed to Associate Professor Shunsuke Nozawa (High Energy Accelerator Research Organization (KEK)), Dr. Rie Haruki (KEK) and Dr. Tomoki Kanazawa (KEK) for XAFS measurements in Chapter 4, and Associate Professor Yu Kimura (Kyoto University) and Assistant Professor Risako Miura for ζ potential measurements in Chapters 4 and 5. Sincere gratitude is expressed to Professor Frank Osterloh (University of California) for his valuable feedback on my work.

The author thanks to all members of Abe laboratory for their kind encouragement, support, and collaboration. Especially, the author is grateful to his junior fellows, Mr. Hiroki Yamada, Ms. Tomoha Shirouchi, and Mr. Tomoki Inoue for their assistance in carrying out the present works. The author deeply thanks secretary Ms. Eri Minoda for her kind support. The author acknowledges the financial support from JSPS Research Fellow (Grant Number 19J23359) and AIST-Kyoto University Chemical Energy Materials Open Innovation Laboratory (ChEM-OIL).

Finally, the author wishes to thank his family and friends for their deep understanding and continuous encouragement toward accomplishing this work.

Hikaru Matsuoka
2022